ELECTRO-OPTICALLY TUNABLE POLARIZATION INDEPENDENT ADD DROP FILTER WITH RELAXED BEAM SPLITTERS IN $LiNbO_3$

A Dissertation

by

YONG-WOOK SHIN

Submitted to the Office of Graduate Studies of
Texas A&M University
in partial fulfillment of the requirements for the degree of

DOCTOR OF PHILOSOPHY

August 2008

Major Subject: Electrical Engineering

ELECTRO-OPTICALLY TUNABLE POLARIZATION INDEPENDENT ADD DROP FILTER WITH RELAXED BEAM SPLITTERS IN $LiNbO_3$

A Dissertation

by

YONG-WOOK SHIN

Submitted to the Office of Graduate Studies of
Texas A&M University
in partial fulfillment of the requirements for the degree of

DOCTOR OF PHILOSOPHY

Approved by :

Chair of Committee,	Ohannes Eknoyan
Committee Members,	Steven Wright
	Christi K. Madsen
	Alvin Yeh
Head of Department,	Costas Georghiades

August 2008

Major Subject: Electrical Engineering

ABSTRACT

Electro-Optically Tunable Polarization Independent

Add Drop Filter with Relaxed Beam Splitters in $LiNbO_3$.

(August 2008)

Yong-Wook Shin, B.S., Yonsei University;

M.S., Yonsei University

Chair of Advisory Committee: Dr. Ohannes Eknoyan

A polarization-independent electro-optically tunable add/drop filter utilizing non-polarizing novel relaxed beam splitters has been developed in $LiNbO_3$ at the 1.55μm wavelength regime. The operation of this filter is based on passive directional coupler type beam splitters and strain-induced phase-matched TE↔TM polarization mode converters on an asymmetric Mach-Zehnder interferometer waveguide configuration. Fabrication parameters for channel waveguides, relaxed beam splitters and polarization mode converters were optimized individually then integrated to produce the final device. Single mode channel waveguides for both TE and TM polarizations were realized by the diffusion of 7μm wide Ti strips into $LiNbO_3$ substrate. Relaxed beam splitters were produced using Ti diffused waveguides in a directional coupler configuration with 3.5mm long coupling region, 0.6º bending angle, and separation gap of 11μm and 13μm between waveguides. Tunable TE↔TM polarization mode converters with 99.8%

conversion efficiency were obtained using a strain-induced refractive index grating consisting of 500 parallel strips formed in a strained SiO_2 surface film with a spatial period of 21μm. The strain results from the thermal expansion mismatch between the film and substrate by depositing the SiO_2 surface film at an elevated substrate temperature then cooling down to room temperature. Polarization independent electro-optically tunable add/drop filters were then produced based on the optimized fabrication parameters of the splitters and the mode converters. Fiber-to-fiber insertion loss on a 45mm long filter device was measured to be less than 6.5dB for both TE and TM polarizations. At the express port, the output spectrum of the filter revealed an approximately 13dB notch without an applied voltage, and the spectral characteristics of the drop port showed a -3dB bandwidth of 2.3nm. The nearest sidelobes were about 10dB below the center peak. Electro-optic tuning of the filter device was demonstrated by applying DC voltages ranging between -100V to +100V. A tuning range of 15.7nm with a linear voltage tuning rate of 0.075nm/V for both the TE and TM polarizations were obtained. The filter has a fast response time. The measured rise and fall times are 22.4ns and 45.6ns, respectively.

To My Family

ACKNOWLEDGMENTS

I would like to thank my advisor and committee chair, Dr. Ohannes Eknoyan, for his concern, encouragement and advice over the past six years. Also, I am very grateful to my committee members, Dr. Christi K. Madsen, Dr Steven Wright and Dr. Alvin Yeh, in addition to the late Dr. Henry Taylor for their time and advice at every step of my research. Without them, this dissertation would not have been accomplished.

I truly appreciate Mr. Robert Atkins and Mr. Jim Gardner for their technical training, support and collaboration throughout my entire research and fabrication steps. There are many friends and colleagues to whom I would like to express my gratitude such as Taehan, Apichai, RyoungHan, Pillip, Kuo, Renato, Jaewoo, Wonju, Xiaomin, Hyunchul, Jongen, Sungkyu, Hyungduk, Myungjoon, Jungmoo, Hyunsoo, Jaewon, Mehmet, Murat, Donny, Wee and family of Yonsei Alumni for their friendship and support in helping me through this toughest of times.

Finally, I'd like to give special thanks from the deepest of my heart to my parents and family especially my lovely Sunhee and Thomas, for their love, concern and encouragement, and for always believing in me throughout the ups and downs during my studies.

TABLE OF CONTENTS

TABLE OF CONTENTS (continued)

TABLE OF CONTENTS (continued)

Page

LIST OF FIGURES

LIST OF FIGURES (continued)

LIST OF FIGURES (continued)

FIGURE Page

LIST OF FIGURES (continued)

FIGURE Page

LIST OF FIGURES (continued)

FIGURE Page

LIST OF TABLES

CHAPTER I

INTRODUCTION

Fiber optic communication is currently the most attractive technology for providing long distance data transfers because of high carrier frequencies (~100THz), low signal attenuation (>0.2dB/km), low signal distortion and low power requirements [1] [2]. For the high speed and large capacity applications required to satisfy the ever increasing bandwidth demands, wavelength division multiplexing (WDM) technologies are rapidly maturing. In WDM, the transmitted light spectrum in a single mode fiber is divided into non-overlapping communication channels as shown in Fig. 1. Hence, the deployment of WDM technology provides a means for exploiting the optical bandwidth available in currently installed fiber networks [3]. Over the long term, high-speed manipulations in the optical domain will be required for packet- and cell-switched networks in IP and asynchronous transfer mode (ATM) applications in point to point transmission links. Since in WDM systems each channel is assigned a different wavelength, channel manipulations and selections require an optical wavelength selection, or optical filtering. Therefore, a key component of the network systems is an optical add-drop filter that can deliver fast packet-switching with narrow channel bandwidth and low cross-talk [4]. Many researches have focused on the development of such devices that can satisfy the various requirements for their performance such as fast

---

This dissertation follows the style and format of *IEEE Journal of Lightwave Technology*.

tuning speed, wide tuning range, narrow bandwidth, efficient side-lobe suppression, low optical insertion loss, low power consumption, minimum cross talk, simple control mechanism, simple fabrication process, small size and low cost [5-8].

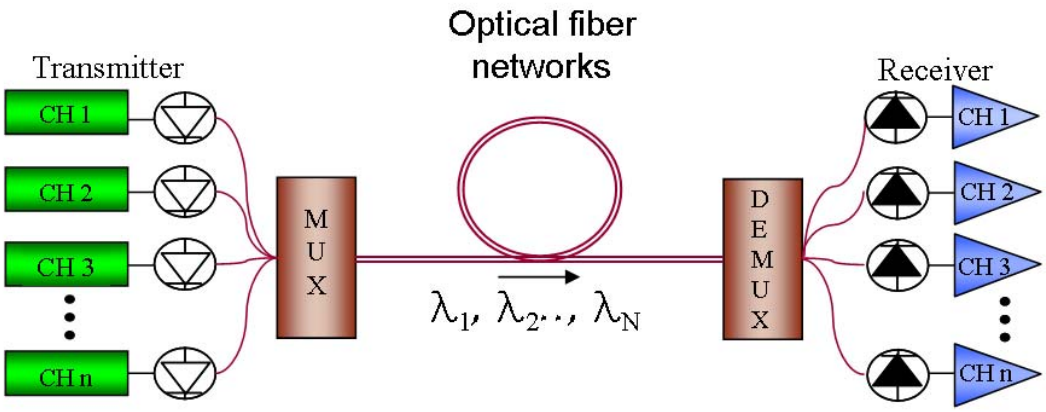

Fig. 1. A schematic of a wavelength division multiplexing link.

Generally, conventional optical tunable filters can be grouped into two main categories [9]:

- Slow-speed tunable filters, with a few milliseconds tuning time, which are used for circuit-switched networks.
- High-speed tunable filters, with microsecond and nanosecond tuning times, which are needed for packet- and cell-switched networks.

Slow-speed tunable filters are usually based on thermal or mechanical effects, and have a matured technology. The devices in the high speed tunable category, however, are mostly in various research stages. Table 1 summarizes the important characteristics of the various reported technologies [10].

Table 1. A comparison of characteristics for various tunable filters.

Filter Category	-3 dB Bandwidth	Tuning Range	Tuning Time	Tuning mechanism
FFP	< 0.5 nm	~ 10 nm	ms	PZT
FBG	< 0.2 nm	< 10 nm	ms	Thermal
AWG	< 0.2 nm	~ 40 nm	10 ms	Thermo-optic
Micromachine FP	< 0.5 nm	~ 60 nm	100 μs	mechanical
AOTF	~ 1.5 nm	250 nm	μs	Acouto-optic
EOTF	~ 1.5 nm	~ 16 nm	ns	Electro-optic

Recent research activities at Texas A&M University have demonstrated an electro-optic tunable filter with Ti-indiffused waveguides in a lithium niobate ($LiNbO_3$) substrate with a bandwidth of 2.3nm and nanosecond tuning speed [11] using a phase matched strain-induced grating for polarization coupling in the 1.55μm wavelength regime. In an extended effort, another electro-optic tunable filter having a narrower bandwidth of 1.56nm and using a longer polarization coupling region was also developed [12]. However, the operation of these optical add-drop multiplexers required the use of polarization beam splitters (PBSs) with large (>20dB) polarization splitting ratio for both TE and TM polarizations. Such optical elements require stringent fabrication controls, they are difficult to produce repeatedly and the filter performance depends strongly upon their polarization splitting behavior. In other words, even if a good splitting can be

obtained for one polarization, it may be very difficult to achieve a similar behavior for the corresponding orthogonal polarization. To overcome this difficulty, the use of relaxed beam splitters was proposed for this research [13]. The relaxed beam splitters offer less stringent requirements for the development of optical add-drop multiplexers.

The objective of this research is to develop a polarization independent electro-optic add/drop tunable filter with relaxed beam splitters in Ti:$LiNbO_3$, at the 1.55μm wavelength regime, and demonstrate rapid tuning capability.

Chapter II consists of a brief theoretical review. Device structure and analysis are given in Chapter III. Chapter IV provides details of the device fabrication. Experimental results are presented in Chapter V. Finally, the conclusive results are summarized in Chapter VI.

CHAPTER II

THEORETICAL REVIEW

Propagation properties of optical waves in dielectric waveguides and anisotropic crystals are reviewed in this chapter, based on Maxwell's equations. The electro-optic and photoelastic effects are outlined. Using coupled-mode theory, the basic concepts of the directional coupler and polarization mode conversion are presented.

A. Basic Theory of Wave Propagation

The electric and magnetic fields in a homogeneous, lossless, isotropic and source-free dielectric medium should satisfy Maxwell's equations, expressed by [14]

$$\nabla \times \mathbf{E} = -\frac{\partial \mathbf{B}}{\partial t} \tag{1}$$

$$\nabla \times \mathbf{H} = \frac{\partial \mathbf{D}}{\partial t} \tag{2}$$

$$\nabla \cdot \mathbf{D} = 0 \tag{3}$$

$$\nabla \cdot \mathbf{B} = 0 \tag{4}$$

where **E** (V/m) and **H** (A/m) represent electric and magnetic field intensity vectors, **D** (C/m^2) is the electric displacement vector, and **B** (Wb/m^2) is the magnetic displacement vector. The relation between **E** and **D** depends on the electric properties of the medium through the dielectric permittivity ε (F/m) of the medium. Similarly, the relation between **H** and **B** depends on the magnetic properties of the medium, which in dielectrics is

simply the permeability of free space μ_0 (H/m). From these relations, **D** and **B** can be defined as follows:

$$\mathbf{D} = \varepsilon_0 \mathbf{E} + \mathbf{P} = \varepsilon \mathbf{E} \tag{5}$$

$$\mathbf{B}=\mu_0 \mathbf{H} \tag{6}$$

in which **P** (C/m^2) is the dielectric polarization density and given by $\mathbf{P}=\varepsilon_0(\varepsilon_r-1)\mathbf{E}$, ε_0 (F/m) is the dielectric permittivity of free space, ε_r is the relative permittivity (or dielectric constant).

The wave equation can be obtained by taking the curl of equation (1), substituting in equation (2), employing equations (3) - (6), and using the vector identity $\mathbf{A}\times\mathbf{B}\times\mathbf{C} = \mathbf{B}(\mathbf{A}\cdot\mathbf{C}) - \mathbf{C}(\mathbf{A}\cdot\mathbf{B})$. The resultant vector wave equation governs the propagation of light in linear, source-free, lossless, nonmagnetic media, and is given by

$$\nabla^2 \mathbf{E} - \varepsilon\mu_0 \frac{\partial^2 \mathbf{E}}{\partial t^2} = 0 . \tag{7}$$

If the electromagnetic wave is monochromatic with an angular frequency, $\omega = \frac{2\pi c}{\lambda}$, the electric field vector **E** can be expressed as

$$\mathbf{E}(\mathbf{r},t) = \mathbf{E}(\mathbf{r})e^{j\omega t}. \tag{8}$$

Substituting equation (8) into (7) and using the relation, $\frac{\partial}{\partial t} = j\omega$, equation (7) becomes

$$\nabla^2 \mathbf{E}(\mathbf{r}) + n^2 k_0^2 \mathbf{E}(\mathbf{r}) = 0 \tag{9}$$

where $k_0 = \frac{\omega}{c}$ is the propagation constant in free space, $c = \frac{1}{\sqrt{\mu_0 \varepsilon_0}}$ is the light speed in free space, and $n = \sqrt{\varepsilon_r}$ is the refractive index of the medium.

B. Optical Waveguides

The propagation behavior of optical wave in dielectric waveguides can be explained with the help of a planar (slab) model which assumes no variation of either refractive index or the electric field, in one dimension. A simple planar waveguide in which the dimensions are finite in *x*- and *y*- direction approaches the behavior of the planar guide when one dimension(here, y) is considerably larger than the other (x in this case).

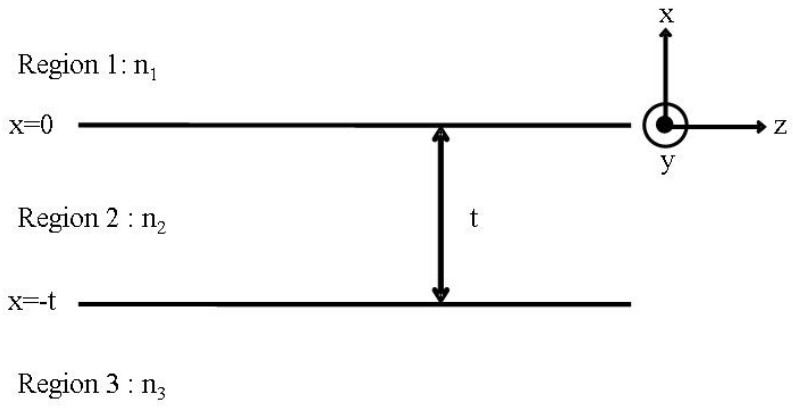

Fig. 2. Planar dielectric waveguide.

In a waveguide, light can be guided within a high refractive index region surrounded by lower refractive index regions through total internal reflection (TIR). A

simple planar waveguide as depicted in Fig. 2 is introduced to explain guided wave propagation.

A mode in such a waveguide at a given frequency is defined by a solution of the vector wave equation. Generally, three-dimensional channel waveguides are more practical, but a solution from a simple planar waveguide structure can give a basic concept of the guided mode. In rectangular coordination, $\nabla^2 = \frac{\partial^2}{\partial \mathrm{x}^2} + \frac{\partial^2}{\partial \mathrm{y}^2} + \frac{\partial^2}{\partial \mathrm{z}^2}$, with $\frac{\partial}{\partial y} = \frac{\partial^2}{\partial y^2} = 0$ since ∞ in the y dimension. For forward propagation along the z-axis, equation (9) becomes [15],

$$\begin{aligned} &\text{Region } 1: \ \frac{d^2}{dx^2}\mathrm{E}(x) + (k_0^2 n_1^2 - \beta^2)\mathrm{E}(x) = 0 \\ &\text{Region } 2: \ \frac{d^2}{dx^2}\mathrm{E}(x) + (k_0^2 n_2^2 - \beta^2)\mathrm{E}(x) = 0 \\ &\text{Region } 3: \ \frac{d^2}{dx^2}\mathrm{E}(x) + (k_0^2 n_3^2 - \beta^2)\mathrm{E}(x) = 0 \end{aligned} \tag{10}$$

where E(x) is a Cartesian component of **E**(x) in each region.

At the boundary between the two dielectric media, the tangential components of electric field **E** and magnetic field **H** and the normal components of electric flux density **D** and magnetic flux density **B** should all be continuous. Assuming that the refractive indices of materials are chosen such that $\mathrm{n}_2 > \mathrm{n}_3 > \mathrm{n}_1$, the solution to equation (10) in each region can be classified as either oscillatory or exponential in nature depending on the propagation constant β. In the case of $\beta < k_0 n_1$, waveguide modes characterized by equation (10) are sinusoidal in all three regions. These give radiation or oscillatory

solutions and the lightwave cannot be guided in the high refractive index n_2 region. For $k_0 n_1 < \beta < k_0 n_3$, the solutions of E(x) correspond to decaying behavior in region 1 and sinusoidal behavior in regions 2 and 3. This is referred as the substrate radiation mode. In the case of $k_0 n_3 < \beta < k_0 n_2$, the solutions of E(x) show exponential decay in regions 1 and 3, and oscillatory action in region 2. Only solutions corresponding to case 3 can support a propagating wave. The optical wave in this case is confined within the middle layer, which is the high refractive index region, and defines guided modes depending on the value of β. In the case of $\beta > k_0 n_2$, the solutions of E(x) show exponential increase away from the interfaces, which is physically unrealistic.

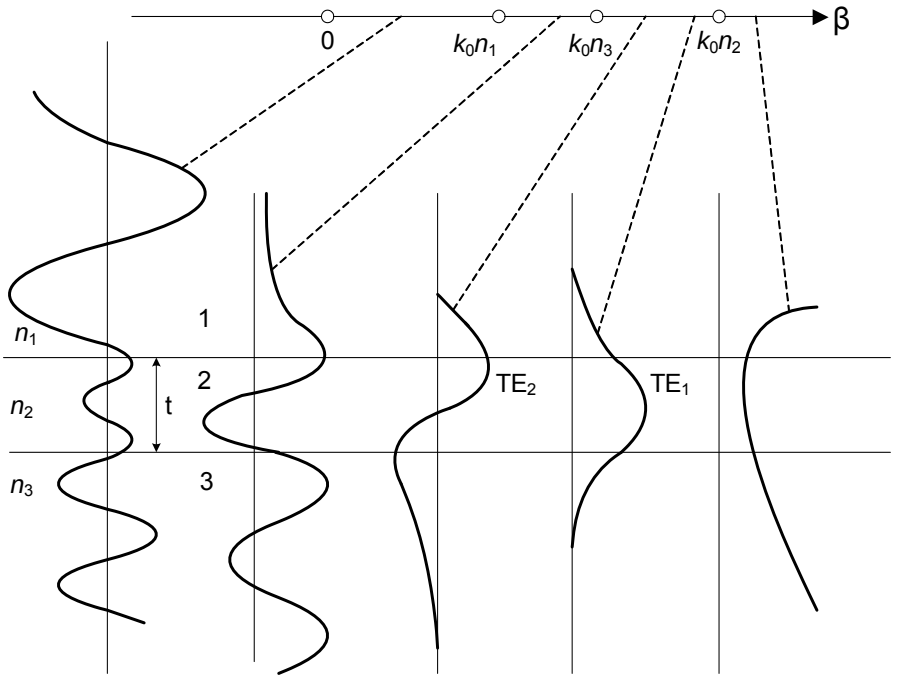

Fig. 3. The electric field distributions of the planar waveguide corresponding to various propagation constants β in a three layer waveguide with $n_2 > n_3 > n_1$.

The electric field distributions for all of the cases mentioned above are illustrated in Fig. 3.

Generally, the planar waveguide shown in Fig. 2 can support a finite number of guided modes. Those modes can be divided into two groups with mutually orthogonal polarization states. One consists of the fields E_y, H_x, H_z and no E_z component which is called the transverse electric (TE) mode because the electric field is transverse to the propagation direction. The other is called the transverse magnetic (TM) mode with fields H_y, E_x, E_z and no H_z component. Considering the TE mode, light tranvels in the z-direction and is polarized in the y-direction with the field components:

$$\mathbf{E}(\mathbf{r},t) = E_y(x)e^{i(\omega t-\beta z)}.\hat{a}_y \tag{11}$$

$$H_{\mathrm{x}} = -\frac{\beta}{\omega\mu_0}E_{\mathrm{y}}$$

$$H_{\mathrm{z}} = -\frac{1}{\mathrm{j}\omega\mu_0}\frac{\partial E_{\mathrm{y}}}{\partial \mathrm{x}}. \tag{12}$$

From equation (11), the field solutions can be written in the form

$$E_y(x) = \begin{cases} Ce^{-qx} & (\text{Region 1}) \\ C\left[\cos(hx) - \frac{q}{h}\sin(hx)\right] & (\text{Region 2}) \\ C\left[\cos(ht) + \frac{q}{h}\sin(ht)\right]e^{p(x+t)} & (\text{Region 3}) \end{cases} \tag{13}$$

where C is an arbitrary constant, t is the thickness of the planar waveguide, and $q = \sqrt{\beta^2 - k_0^2 n_1^2}$, $h = \sqrt{k_0^2 n_2^2 - \beta^2}$, $p = \sqrt{\beta^2 - k_0^2 n_3^2}$. Allowed modes can be determined

from boundary conditions that requires continuity of E_y and H_z across the interfaces $x = 0$ and $x = -t$, which yields the relationship

$$\tan(ht) = \frac{p+q}{(h - \frac{q}{h}p)} \quad . \tag{14}$$

This is called the characteristic equation for the TE mode and also an Eigen value equation, and identifies discrete values for h with each h corresponding to one value of β , or a mode.

For TM guided wave propagation, a similar approach to that used for the TE modes is applied. The field components are

$$\mathbf{H}(\mathbf{r},t) = H_y(x)e^{j(\omega t - \beta z)}.\hat{a}_y \tag{15}$$

$$\begin{aligned} E_x &= \frac{\beta}{\omega\varepsilon_0 n^2} H_y \\ E_z &= \frac{1}{j\omega\varepsilon_0 n^2}\frac{\partial H_y}{\partial x} \end{aligned} \quad . \tag{16}$$

Solving for the field components $H_y(x)$ and applying the boundary condition in a the same manner, gives

$$\tan(ht) = \frac{\left(\frac{n_2}{n_1}\right)^2 q + \left(\frac{n_2}{n_3}\right)^2 p}{h - \left(\frac{n_2^2}{n_1 n_3}\right)\frac{pq}{h}} \quad . \tag{17}$$

Eigen values β identify the number of allowed modes in a waveguide. In guided wave optoelectronics, a single mode is desired for most applications. This is generally the lowest order mode and is called the fundamental mode.

C. Optical Indicatrix in Uniaxial Crystals

If the medium is isotropic, the polarization in the material is parallel to the electric field and linearly related by a constant electric susceptibility that is independent of the direction along which the field is applied. However, in anisotropic media, the electric susceptibility is no longer a constant and polarization by the electric field depends on the direction of the field. Therefore, wave propagation in anisotropic media displays a directional dependence on electric susceptibility which relates the electric polarization and field vectors as

$$\mathbf{P} = \varepsilon_0 \tilde{\chi}_e \mathbf{E} \tag{18}$$

where $\tilde{\chi}_e$ is a 3 × 3 electric susceptibility tensor. To simplify the analysis, a reference coordinate can be chosen along the principal axes of the crystal so that all off-diagonal components of the electric susceptibility tensor reduce to zero. From equations (5) and (18) with the use of diagonal $\tilde{\chi}_e$, the permittivity of the medium $\tilde{\varepsilon} = \varepsilon_0(\mathbf{I} + \tilde{\chi}_e)$ can be written as

$$\tilde{\varepsilon} = \begin{bmatrix} \varepsilon_{11} & 0 & 0 \\ 0 & \varepsilon_{22} & 0 \\ 0 & 0 & \varepsilon_{33} \end{bmatrix} = \varepsilon_0 \begin{bmatrix} n_x^2 & 0 & 0 \\ 0 & n_y^2 & 0 \\ 0 & 0 & n_z^2 \end{bmatrix} \tag{19}$$

where ε_{11}, ε_{22}, ε_{33} are called principal permittivities. It follows from equation (5) that the relation between **E** and **D** can be rewritten as:

$$\mathbf{D} = \begin{bmatrix} D_x \\ D_y \\ D_z \end{bmatrix} = \begin{bmatrix} \varepsilon_{11} & 0 & 0 \\ 0 & \varepsilon_{22} & 0 \\ 0 & 0 & \varepsilon_{33} \end{bmatrix} \begin{bmatrix} E_x \\ E_y \\ E_z \end{bmatrix} = \tilde{\varepsilon}\mathbf{E} \ . \tag{20}$$

The optical properties of crystals are determined by their crystal structures. The simplest form of anisotropy is the uniaxial case, such as in $LiNbO_3$ or $LiTaO_3$ with $n_x = n_y \neq n_z$. The stored electric energy density of propagating wave in a crystal is given by

$$U_e = \frac{1}{2}\mathbf{E} \cdot \mathbf{D} \ . \tag{21}$$

Combining equations (20) and (21) yields

$$U_e = \frac{1}{2}\left[\frac{D_x^2}{\varepsilon_{11}} + \frac{D_y^2}{\varepsilon_{22}} + \frac{D_z^2}{\varepsilon_{33}} \right] . \tag{22}$$

Defining the following relationships $x = D_x / \sqrt{2\varepsilon_0 U_e}$, $y = D_y / \sqrt{2\varepsilon_0 U_e}$, $z = D_z / \sqrt{2\varepsilon_0 U_e}$ and substituting in equation (22) produces an equation that identifies the indices of refraction associated with a specific propagation direction of a wave in an anisotropic material, which is given as [16]

$$\frac{x^2}{n_x^2} + \frac{y^2}{n_y^2} + \frac{z^2}{n_z^2} = 1 \, . \tag{23}$$

Equation (23) represents an index ellipsoid or indicatrix with the principal axes *x*, *y*, and *z*. In uniaxial crystals $n_x = n_y \equiv n_0$ and $n_z \equiv n_e$. This reduces the index ellipsoid equation to

$$\frac{x^2}{n_0^2} + \frac{y^2}{n_0^2} + \frac{z^2}{n_e^2} = 1 \tag{24}$$

where the axis of symmetry is chosen as the z axis. The z axis is also called the optic axis, n_o is the ordinary index of refraction, whereas n_e is the extraordinary one.

Fig. 4 illustrates the procedure for determining the indices of refraction for a given direction of wave propagation in a uniaxial crystal.

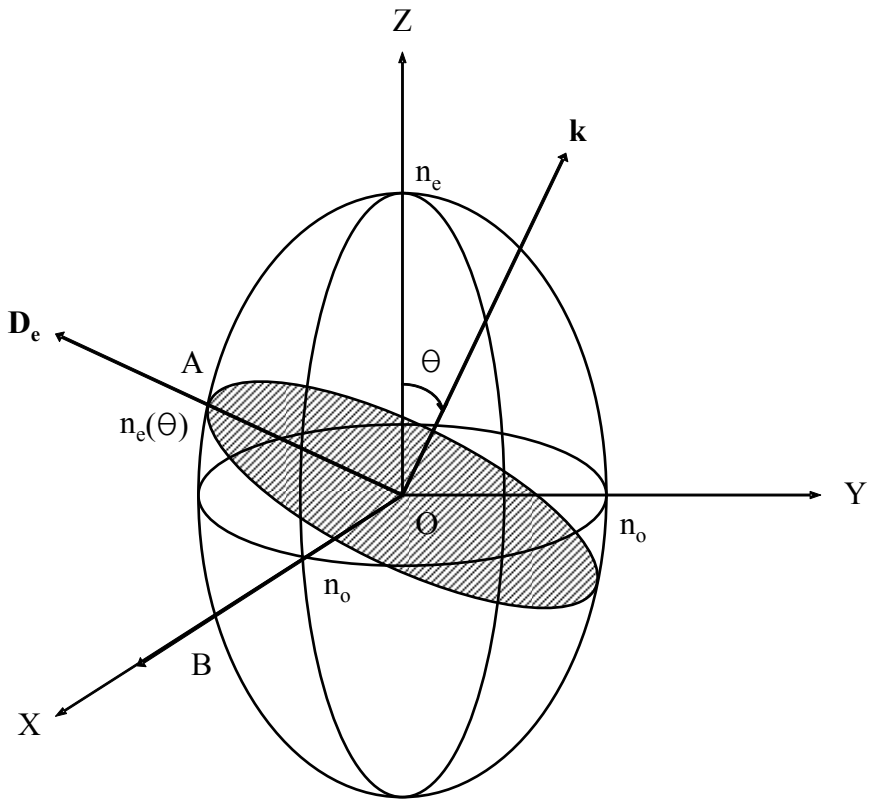

Fig. 4. Optical indicatrix (index ellipsoid) of uniaxial crystals.

To determine the refractive indices associated with an arbitrary direction of propagation **k**, an intersection plane with the index ellipsoid that passes through the origin of the indicatrix and is perpendicular to **k** is constructed. This intersection

produces an ellipse, as shown shaded in Fig. 4. The two allowed orthogonal polarizations coincide with the major and minor axes of the ellipse. One allowed polarization, $\mathbf{D}_0$, along the OB direction, always encounters a constant refractive index n_0, which is independent of the angle θ. This is referred to as an *ordinary* wave. The other allowed polarization, $\mathbf{D}_e$, parallel to the OA direction, encounters an index $n_e(\theta)$, that depends on the angle θ. This is said to be an *extraordinary* wave. The index of extraordinary waves is equal to the length of OA in Fig. 4, which is given by

$$\begin{aligned} n_e^2(\theta) &= y^2 + z^2 \\ y &= n_e(\theta)\cos\theta \\ z &= n_e(\theta)\sin\theta \end{aligned} . \tag{25}$$

Substituting equation (25) into equation (24) yields

$$n_e(\theta) = \frac{n_0 n_e}{\sqrt{n_e^2\cos^2\theta + n_0^2\sin^2\theta}} . \tag{26}$$

From equation (26), it can be seen that the refractive index of the extraordinary wave varies from $n_e(\theta) = n_0$ at $\theta = 0$ to $n_e(\theta) = n_e$ at $\theta = 90^\circ$. In particular, when $\theta = 0$, the uniaxial crystal will behave as if it is optically isotropic (both ordinary and extraordinary waves encounter the index n_0); therefore, the z-axis of a uniaxial crystals is called the optical axis [17].

D. Directional Coupler

Fig. 5 shows a schematic drawing for a directional coupler. A directional coupler consists of two closely spaced channel waveguides. The performance of a directional coupler can be described from the coupled mode theory [18].

$$\frac{dA_s^-}{dy}\cdot e^{j(\omega t+\beta_s y)} - \frac{dA_s^+}{dy}\cdot e^{j(\omega t-\beta_s y)} - C.C = \frac{-j}{2\omega}\cdot\frac{\partial^2}{\partial t^2}\int_{-\infty}^{+\infty}\left[P_{pert}\right]_z \cdot E_z^s \cdot dx\,. \qquad (27)$$

If the theory is applied to waveguide A without a backward wave and with TE polarization, then the above equation can be simplified into

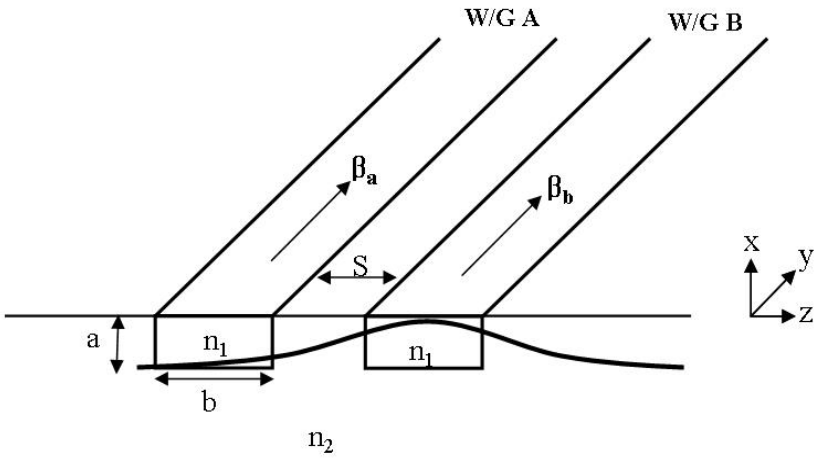

Fig. 5. A schematic drawing of a directional coupler.

$$-\frac{dA_s^+}{dy}\cdot e^{j(\omega t-\beta_s y)} - C.C = \frac{-j}{2\omega}\cdot\frac{\partial^2}{\partial t^2}\int_{surface}\left[P_{pert}(r,t)\right]_z \cdot E_{Az}^s \cdot dx\cdot dz \qquad (28)$$

where, $P_{pert}(x,y,z,t) = \varepsilon_0\left[n_1^2(x,z) - n_2^2\right]\cdot E_{Bz}(x,y,z,t)$

$$\frac{dA_s^+}{dy}\cdot e^{j(\omega t-\beta_s y)} + C.C = \frac{j}{2\omega}\cdot(j\omega)^2\int_{surface}\left[\varepsilon_0(n_1^2(x,z)-n_2^2)E_{Bz}^s(x,z)\cdot e^{j(\omega t-\beta_b y)}\cdot\frac{B(y)}{2} + C.C\right]$$

$$\cdot E_{Az}(x,z)dx \cdot dz \tag{29}$$

$$\frac{dA_s^+}{dy} \cdot = -jB(y)\left[\frac{\omega\varepsilon_0}{4} \cdot \int_{surface} (n_1^2(x,z) - n_2^2) \cdot E_{Az}(x,z) \cdot E_{Bz}(x,z) \cdot dx \cdot dz\right] \cdot e^{j(\beta_a - \beta_b)y}. \tag{30}$$

The left hand side of equation (30) represents the change in amplitude of a forward propagating wave that couples into waveguide A, B(y) is the change in amplitude of the guided wave propagating in waveguide B, and the bracketed terms describe the coupling coefficient which is defined as κ_{ab}. As the two wave propagate along y in their respective regions, the power couples back and forth between waveguide A and B. By reciprocity, this can be expressed as

$$\frac{dA}{dy} = -j\kappa_{ab} B(y) \cdot e^{j(\beta_a - \beta_b)y} \tag{31}$$

$$\frac{dB}{dy} = -j\kappa_{ba} A(y) \cdot e^{j(\beta_b - \beta_a)y}. \tag{32}$$

If waveguide A and B are identical, $\beta_a = \beta_b$ and also $\kappa_{ab} = \kappa_{ba} = \kappa$

$$\kappa = \frac{2h_z^2 \gamma_{2z} e^{-\gamma_{2z} \cdot S}}{\beta \cdot b(h_z^2 + \gamma_{2z}^2)} \tag{33}$$

where S is the distance between waveguides. The coupling ratio can be controlled by adjusting the distance between waveguides and the waveguides field mode distribution. Then equations (31) and (32) reduce to

$$\frac{dA}{dy} = -j\kappa B(y) \tag{34}$$

$$\frac{dB}{dy} = -j\kappa A(y). \tag{35}$$

Differentiating equation (35) and combining it with equation (34), an ordinary second order differential equation can be obtained as follows

$$\frac{d^2B(y)}{dy^2} + \kappa^2 \cdot B(\kappa) = 0 . \tag{36}$$

For light entering only into waveguide A, the amplitude of the fields at y=0 can be defined as $A(y=0)=A_o$ and $B(y=0)=0$. Using a general solution for the ordinary differential equation and applying boundary conditions, the amplitudes as a function of the propagating distance in each waveguide are expressed as

$$A(y) = A_o \cos(\kappa y) \tag{37}$$

$$B(y) = -jA_o \sin(\kappa y) . \tag{38}$$

From these equations it is clear that the phase for the amplitude of a driven waveguide always lags behind the phase of the driving waveguide by 90°.

E. Linear Electro-optic (Pockels) Effect

The electro-optic effect provides a change in the refractive index in an optical crystalline material that is proportional to the applied electric field. The linear relation between the refractive index and the electric field is known as the linear electro-optic or Pockels effect. The quadratic (nonlinear) relation between the refractive index and the electric field is called as the Kerr effect. Since the Pockels effect is commonly used in integrated optics and also induces larger refractive index changes, the linear electro-optic (Pockels) effect is the basis for active waveguide device control. Electrooptically induced

index changes can be characterized by specifying changes in the index ellipsoid equation (23). When an electric field is applied, the index ellipsoid equation is written as

$$\left(\frac{1}{n^2}\right)_1 x^2 + \left(\frac{1}{n^2}\right)_2 y^2 + \left(\frac{1}{n^2}\right)_3 z^2 + 2\left(\frac{1}{n^2}\right)_4 yz + 2\left(\frac{1}{n^2}\right)_5 xz + 2\left(\frac{1}{n^2}\right)_6 xy = 1. \qquad (39)$$

If x, y, and z are set to be parallel to the crystal's principal axes, then in the absence of electric field, equation (39) reduces to,

$$\left(\frac{1}{n^2}\right)_i\Bigg|_{E=0} = \begin{cases} \frac{1}{n_j^2}, j = 1,2,3 \\ 0, i = 4,5,6 \end{cases} \qquad (40)$$

where j = 1, 2, 3 denotes x, y, z, respectively. When an electric field is applied, the inverse of the indices in equation (40) are expressed as

$$\left(\frac{1}{n^2}\right)_i\Bigg|_{E\neq 0} = \begin{cases} \frac{1}{n_j^2} + \Delta\left(\frac{1}{n^2}\right)_i, i = 1,2,3 \\ 0 + \Delta\left(\frac{1}{n^2}\right)_i, i = 4,5,6 \end{cases}. \qquad (41)$$

The induced refractive index change $\Delta\left(\frac{1}{n^2}\right)_i$ due to an applied electric field is defined by

$$\Delta\left(\frac{1}{n^2}\right)_i = \sum_{j=1}^{3} r_{ij} E_j \qquad (42)$$

where i=1, 2, …, 6. E_j is the component of the applied electric field, and r_{ij} is a 6×3 electro-optic coefficient tensor. For a uniaxial crystal structure such as $LiNbO_3$, $n_x = n_y = n_o$, $n_z = n_e$, and the electro-optic tensor is

$$\begin{pmatrix} 0 & -r_{22} & r_{13} \\ 0 & r_{22} & r_{13} \\ 0 & 0 & r_{33} \\ 0 & r_{51} & 0 \\ r_{51} & 0 & 0 \\ -r_{22} & 0 & 0 \end{pmatrix} \tag{43}$$

where $r_{33} = 30.8\times10^{-12}$ m/V, $r_{13} = 8.6\times10^{-12}$ m/V, $r_{22} = 3.4\times10^{-12}$ m/V, and $r_{51} = 26\times10^{-12}$ m/V.

If the electric field **E** is applied along the z-direction of a $LiNbO_3$ crystal, with equations (39), (41), and (42) the index ellipsoid equation becomes

$$\left(\frac{1}{n_o^2}+r_{13}E_z\right)x^2+\left(\frac{1}{n_o^2}+r_{13}E_z\right)y^2+\left(\frac{1}{n_e^2}+r_{33}E_z\right)z^2=1. \tag{44}$$

According to equations (41) and (42), the new refractive indices along the principal axes can be found as

$$\begin{aligned} \frac{1}{n_x^2} &= \frac{1}{n_o^2}+r_{13}E_z \\ \frac{1}{n_y^2} &= \frac{1}{n_o^2}+r_{13}E_z \\ \frac{1}{n_z^2} &= \frac{1}{n_e^2}+r_{33}E_z \end{aligned} \tag{45}$$

Since the electrooptic coefficients are very small, then $n_o^2 r_{13} E_z << 1$ and $n_e^2 r_{33} E_z << 1$. Therefore $(1+x)^a \approx 1+ax$ can be applied, and the new refractive indices obtained as

$$
\begin{aligned}
n_x &= n_o - \frac{1}{2} n_o^3 r_{13} E_z \\
n_y &= n_o - \frac{1}{2} n_o^3 r_{13} E_z \cdot \\
n_z &= n_e - \frac{1}{2} n_e^3 r_{33} E_z
\end{aligned}
\tag{46}
$$

More complicated cases occur if the electric fields is not in the z- direction and mixed terms appear in the index ellipsoid equation (39).

F. Photoelastic Effect and Strain Distribution

For a homogeneous, continuous solid body, external forces cause a change in distances between the different points in the body of the material. Generally, it is said that the solid body undergoes a deformation. In an elasto-optic crystalline material, the deformation induces their refractive index change. Many crystals show the refractive index change in a certain direction is different from that in other directions.

Consider a small volume element surrounding a point **P** of coordinates x_i (i =1,2,3), as shown in Fig. 6. If an infinitesimal displacement **u**(x_i) is applied, the point **P** moves to **P′.** Similarly, the position of a neighboring point **Q** which is an incremental distance **dx** from point **P** will also displace to **Q′**.

The coordinates of **Q`**, to first order are

$$
x_i + dx_i + u_i + \frac{du_i}{dx_j} dx_j . \tag{47}
$$

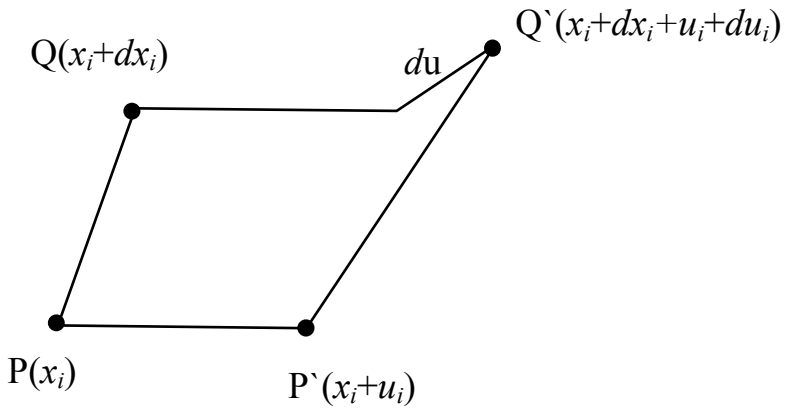

Fig. 6. Illustration of the deformation of two neighboring points **P** and **Q.**

Thus the difference between vectors **PQ** and **P`Q`** is a vector **du** of components

$$du_i = \left(\frac{du_i}{dx_j} \right) dx_j . \tag{48}$$

The resulting nine elements $\partial u_i / \partial x_j$ represent a (3×3) tensor that relates the displacement **du** to the unperturbed increment **dx**, and is called the strain tensor [19]. The strain tensor is symmetric with only six independent variables so it can be replaced with a 1×6 matrix without losing any generality.

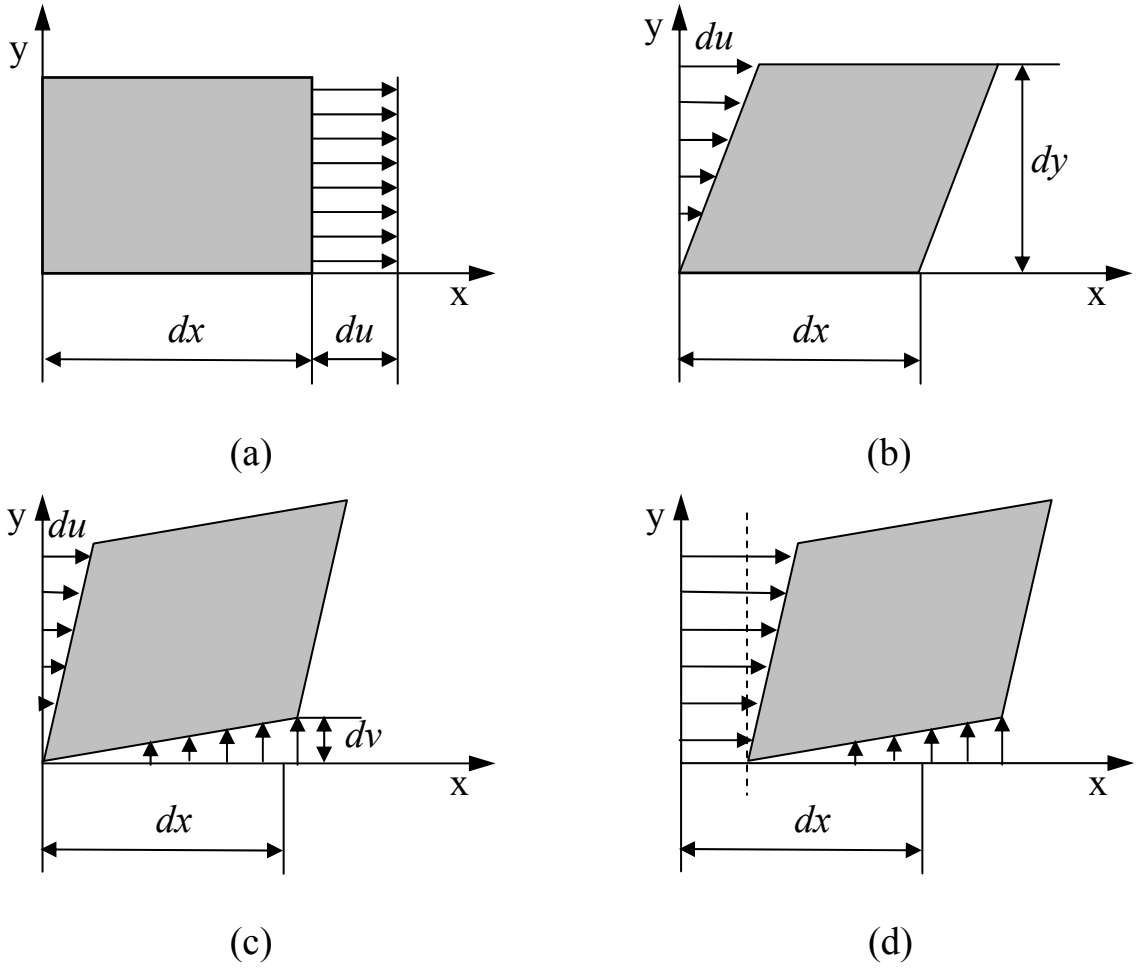

Fig. 7. Strain components. (a) Principal strain. (b) Shearing strain in y. (c) Shearing strain in x and y. (d) Combination of principal strain and shearing strain.

There are two types of strain. One type is principal strain in which the deformation occurs uniformly across the plane as shown in Fig. 7 [20]. The other type of strain generates deformation which is not uniform across the plane, and is called the shear strain. Based on these definitions, the six components of strain can be summarized as

$$S_1 = \frac{\partial u_1}{\partial x_1}, \quad S_2 = \frac{\partial u_2}{\partial x_2}, \quad S_3 = \frac{\partial u_3}{\partial x_3}, \tag{49}$$

$$S_4 = \frac{1}{2}\left(\frac{\partial u_i}{\partial x_3} + \frac{\partial u_j}{\partial x_2}\right), \quad S_5 = \frac{1}{2}\left(\frac{\partial u_i}{\partial x_3} + \frac{\partial u_j}{\partial x_1}\right), \quad S_6 = \frac{1}{2}\left(\frac{\partial u_i}{\partial x_2} + \frac{\partial u_j}{\partial x_1}\right) \tag{50}$$

where S_1, S_2, S_3 are called principle strains and S_4, S_5, S_6 are called shear strains. The linear photoelastic effect can be defined in the same manner as the linear electro-optic effect described previously. In this case

$$\Delta\left(\frac{1}{n^2}\right)_{ij} = P_{ijkl} S_{kl} \tag{51}$$

where i, j, k, l = 1, 2, 3 and $\left(\frac{1}{n^2}\right)_{ij}$ is the constant of the index ellipsoid equation (39). P_{ijkl} is the elastooptic constant [21], and S_{kl} is the strain component defined as

$$S_{kl}(\mathbf{r}) = \frac{1}{2}\left[\frac{\partial u_k(\mathbf{r})}{\partial x_l} + \frac{\partial u_l(\mathbf{r})}{\partial x_k}\right] \tag{52}$$

where $u_k(\mathbf{r})$ is the displacement of a point **r** in the crystal projected along the direction k. The strain tensor S_{kl} and the photoelastic tensor P_{ijkl} can be expressed as a six-component vector and a second-order tensor having 6×6 components, respectively by correlating α = 1, 2, 3, 4, 5, 6 to ij = 11, 22, 33, 23, 31, 12 and β = 1, 2, 3, 4, 5, 6 to kl = 11, 22, 33, 23, 31, 12. Therefore, equation (51) yields

$$\Delta n_\alpha = -\frac{1}{2} n_\alpha^3 P_{\alpha\beta} S_\beta \tag{53}$$

where $n_\alpha = \sqrt{n_{ii} n_{jj}}$, $P_{\alpha\beta} = P_{ijkl}$, and $S_\beta = S_{kl}$. Based on the definition of equation (49) and (50), the six-component vector S_β is given by

$$\begin{pmatrix} S_1 \\ S_2 \\ S_3 \\ S_4 \\ S_5 \\ S_6 \end{pmatrix} = \begin{pmatrix} \dfrac{\partial u_1}{\partial x_1} \\ \dfrac{\partial u_2}{\partial x_2} \\ \dfrac{\partial u_3}{\partial x_3} \\ \dfrac{1}{2}\left(\dfrac{\partial u_2}{\partial x_3} + \dfrac{\partial u_3}{\partial x_2} \right) \\ \dfrac{1}{2}\left(\dfrac{\partial u_1}{\partial x_3} + \dfrac{\partial u_3}{\partial x_1} \right) \\ \dfrac{1}{2}\left(\dfrac{\partial u_1}{\partial x_2} + \dfrac{\partial u_2}{\partial x_1} \right) \end{pmatrix} \tag{54}$$

where 1, 2, and 3 indicate x, y, and z, respectively. S_1, S_2, and S_3 are the longitudinal strain components and S_4, S_5, and S_6 are the shear strain components.

As an example, for $LiNbO_3$ and $LiTaO_3$, which are crystals with 3m symmetry, the photoelastic (also called strain-optic) matrix is [21]

$$[p_{ij}] = \begin{bmatrix} p_{11} & p_{12} & p_{13} & p_{14} & 0 & 0 \\ p_{12} & p_{11} & p_{13} & -p_{14} & 0 & 0 \\ p_{31} & p_{31} & p_{33} & 0 & 0 & 0 \\ p_{41} & -p_{41} & 0 & p_{44} & 0 & 0 \\ 0 & 0 & 0 & 0 & p_{44} & p_{41} \\ 0 & 0 & 0 & 0 & p_{14} & \dfrac{1}{2}(p_{11} - p_{12}) \end{bmatrix}. \tag{55}$$

If a strain component S_6 exists, then from equation (51) the index change in

reduced notation is written as $\Delta\left(\frac{1}{n^2}\right)_i = \sum_i^6 p_{ij} S_j$ with i=1,2,….6, and for i=5 becomes

$$\Delta n_5 = -\frac{1}{2}\bar{n}^3 p_{41} S_6 \tag{56}$$

where, $\bar{n} = (n_o n_e)^{1/2}$.

G. TE ↔ TM Mode Conversion

When an optical mode propagates in a waveguide containing a spatially periodic refractive index perturbation, coupling between orthogonal TE and TM components takes place. The basic concept of the polarization conversion can be explained by a small perturbation in the dielectric polarization density **P**, and examining this perturbation effect on the time dependent wave equation. From previous theoretical reviews, the wave equation in a dielectric medium can be rewritten as

$$\nabla^2 \mathbf{E}(\mathbf{r},t) = \varepsilon(\mathbf{r})\mu_0 \frac{\partial^2 \mathbf{E}(\mathbf{r},t)}{\partial t^2}. \tag{57}$$

Substituting equation (5) into (57), gives

$$\nabla^2 \mathbf{E}(\mathbf{r},t) = \varepsilon_0 \mu_0 \frac{\partial^2 \mathbf{E}(\mathbf{r},t)}{\partial t^2} + \mu_0 \frac{\partial^2 \mathbf{P}(\mathbf{r},t)}{\partial t^2}. \tag{58}$$

The dielectric polarization **P** can be considered to be the sum of two terms, unperturbed and perturbed polarizations

$$\mathbf{P}(\mathbf{r},t) = \mathbf{P}_o(\mathbf{r},t) + \mathbf{P}_{pert}(\mathbf{r},t) \tag{59}$$

with

$$\mathbf{P}_o(\mathbf{r},t) = \left[\varepsilon(\mathbf{r}) - \varepsilon_0\right]\mathbf{E}(\mathbf{r},t). \tag{60}$$

Substituting equations (59) and (60) into (58), yields

$$\nabla^2 E_i(\mathbf{r},t) - \mu_0 \varepsilon(\mathbf{r}) \frac{\partial^2 E_i(\mathbf{r},t)}{\partial t^2} = \mu_0 \frac{\partial^2}{\partial t^2} \left[\mathbf{P}_{pert}(\mathbf{r},t) \right]_i \tag{61}$$

where i indicates x, y, or z and $E_i(\mathbf{r},t)$ is a component of $\mathbf{E}(\mathbf{r},t)$.

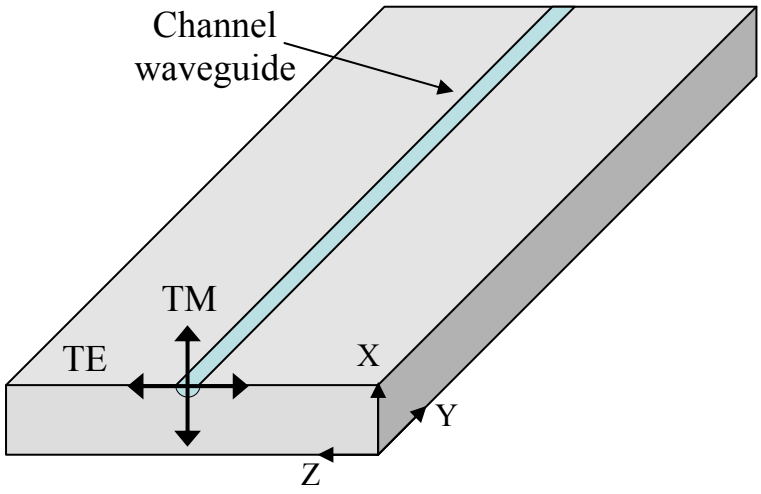

Fig. 8. Polarization directions of the TE and TM modes propagating along a y-direction in an optical channel waveguide on an x-cut substrate.

For the example of an x-cut y-propagating channel waveguide as shown in Fig. 8, a TE-polarized mode has its transverse electric field along z-direction ($E_x = 0$) while the TM-polarized mode has its transverse electric field along the x-direction ($E_z = 0$). According to equation (61), an x-component of the perturbation polarization, P_x, is needed to achieve coupling from a TE-mode into a TM-mode, while for coupling a TM-mode into a TE-mode, a z-directed perturbation polarization component, P_z, is required. Based on equation (5),

$$D_i = \varepsilon_{ij} E_j = \varepsilon_0 E_i + P_i \tag{62}$$

where j=1,2,3, or simply

$$P_i = (\varepsilon_{ij} - \varepsilon_0 \delta_{ij}) E_j \tag{63}$$

where δ_{ij}=1 for i=j, and zero for i≠j. Thus, the perturbation of medium polarization P_{pert} can be expressed as

$$\left[P_{pert} \right]_i = \Delta P_i = \Delta \varepsilon_{ij} E_j = \varepsilon_0 (\Delta \varepsilon'_{ij}) E_j \,. \tag{64}$$

Substituting equations (43) and (46) into equation (64), yields

$$\left[P_{pert} \right]_i = \Delta P_i = -\varepsilon_0 \varepsilon'_{ii} \varepsilon'_{jj} \Delta \left(\frac{1}{n^2} \right)_{ij} E_j \,. \tag{65}$$

For TE $\rightarrow$ TM mode conversion, equation (65) indicates that a perturbation polarization ΔP_x (along the x-direction) is required, or

$$\Delta P_1 = -\varepsilon_0 \varepsilon'_{11} \varepsilon'_{33} \Delta \left(\frac{1}{n^2} \right)_{13} E_3 \tag{66}$$

where $\varepsilon'_{11} = n_o^2$ and $\varepsilon'_{33} = n_e^2$ for a uniaxial crystal. Then, equation (66) can be rewritten as

$$\Delta P_1 = -\varepsilon_0 n_o^2 n_e^2 \Delta \left(\frac{1}{n^2} \right)_5 E_3 \,. \tag{67}$$

For the case of the TM $\rightarrow$ TE mode conversion, the required perturbation polarization is ΔP_z (along the z-direction)

$$\Delta P_3 = -\varepsilon_0 n_o^2 n_e^2 \Delta \left(\frac{1}{n^2} \right)_5 E_1 \,. \tag{68}$$

In equations (67) and (68), the important fact is that TE $\leftrightarrow$ TM mode conversions can be produced from an induced refractive index change Δn_5 , via the photoelastic effect.

Using coupled-mode theory [18], TE$\leftrightarrow$TM mode conversion can be analyzed. The following equations describe the coupling relation between these two orthogonal modes.

$$\begin{cases} \dfrac{dA_m(y)}{dy} = -j\kappa B_m(y) e^{-j(\beta_m^{TM} - \beta_m^{TE})y} \\ \dfrac{dB_m(y)}{dy} = -j\kappa A_m(y) e^{+j(\beta_m^{TM} - \beta_m^{TE})y} \end{cases} \tag{69}$$

where A_m and B_m are the amplitudes of TE and TM m^{th} mode; β_m^{TE} and β_m^{TM} are the propagating constants of TE and TM m^{th} mode; κ is the coupling coefficient, and y is the propagating direction of the mode. If the TM polarized mode enters into a waveguide with an amplitude of B_0, the solutions to equation (69) are:

$$\begin{cases} A_m(y) = aB_0 e^{-j\delta y} \\ B_m(y) = bB_0 e^{+j\delta y} \end{cases} \tag{70}$$

where

$$\begin{aligned} a &= -j\frac{\kappa}{(\kappa^2+\delta^2)^{1/2}} \sin\left[(\kappa^2+\delta^2)^{1/2} y\right] \\ b &= \cos\left[(\kappa^2+\delta^2)^{1/2} y\right] - j\frac{\delta}{(\kappa^2+\delta^2)^{1/2}} \sin\left[(\kappa^2+\delta^2)^{1/2} y\right]. \\ \delta &= \frac{1}{2}(\beta_m^{TM} - \beta_m^{TE}) \end{aligned} \tag{71}$$

A plot of the TE and TM mode power exchange normalized to an input intensity of $|B_0|^2$ is shown in Fig. 9. With the phase-matched condition $\delta = 0$, all of the power of a polarized mode can be periodically coupled into its orthogonal polarization, whereas

with $\delta \neq 0$ only a partial periodic power transfer occurs because of a phase mismatch δ between the orthogonal TE and TM polarization modes.

For the crystal orientation shown in Fig. 8, $\beta_{TM} = \frac{2\pi}{\lambda_o} n_o$, $\beta_{TE} = \frac{2\pi}{\lambda_o} n_e$, with $n_o \neq n_e$.

To achieve $\delta \neq 0$, a deliberate periodic variation with a period Λ is introduced. The phase-mismatch factor δ can then be described as [22]

$$\delta = \frac{\beta_{TM} - \beta_{TE}}{2} \pm \frac{\pi}{\Lambda}. \tag{72}$$

To satisfy the phase-matched condition $\delta = 0$, the required period Λ becomes

$$\Lambda = \frac{2\pi}{|\beta_{TM} - \beta_{TE}|} = \frac{2\pi}{(2\pi/\lambda_o)|n_{TM} - n_{TE}|} = \frac{\lambda_o}{|n_{TM} - n_{TE}|}. \tag{73}$$

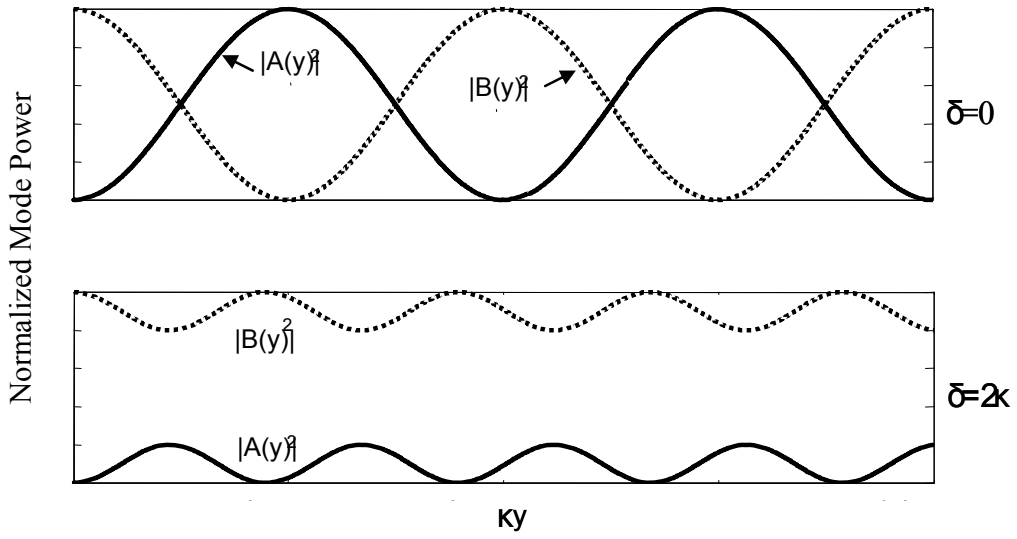

Fig. 9. Periodic power transfer between the TE and TM modes with δ=0 and δ=2κ.

For a fixed period Λ in such a polarization mode converter device, the coupling between TE and TM modes becomes highly wavelength selective. The phase-match wavelength λ_o can be adjusted by changing the birefringence $|n_{TM}-n_{TE}|$.

CHAPTER III

DEVICE STRUCTURE AND ANALYSIS

In this chapter, the structure of the proposed tunable add/drop filter is presented, and its overall principle of operation is explained. The design and properties of each of the individual elements required to form the integrated optical tunable filter are discussed.

A. Proposed Optical Add Drop Filter

The proposed electro-optic tunable filter device structure is shown in Fig. 10. It is basically a Mach-Zehnder interferometer that consists of two relaxed beam splitters, which are connected at the center by the interferometer arms. All waveguides are single mode. The interferometer arms include strain-inducing strips to provide a phase-matched TE↔TM polarization conversion, and electrodes for wavelength tuning. The proposed design differs from conventional designs in the following three aspects:

1. Polarization beam splitters are not required.
2. There is an optical path difference of as much as half a wavelength, or odd integral multiples, between the upper and lower arms.
3. The relative positions for the TE↔TM polarization coupling regions in the upper and lower waveguides are displaced in the propagation direction by half of the spatial period of the perturbation responsible for the coupling.

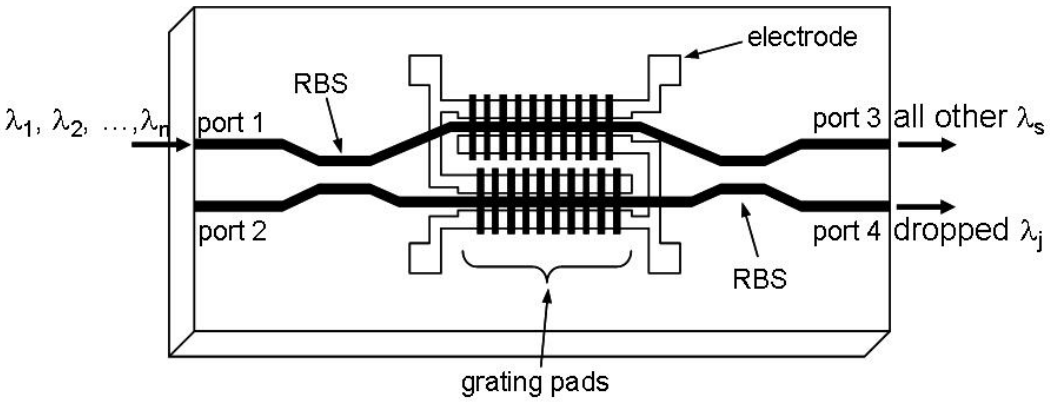

Fig. 10. Proposed electro-optic tunable filter design.

Primarily, the multiplexer is capable of separating a stream of incident wavelength channels such that a single selected wavelength channel can be tapped out, and also tapped back in. In the shown configuration, the selected wavelength channel is directed to the lower output port, while all other channels emerge from the upper output port. Channel selection can be accomplished by applying voltage to the electrodes. For a channel to be dropped its wavelength must satisfy the phase matched condition. A dropped channel can be tapped back into the main stream of exiting channels by adding it from the lower port on the input side.

To describe the operation of the multiplexer, the performance of the beam splitter, and the progression of the incident beam for non-selected wavelength channels and selected drop wavelength channel are outlined below using a matrix representation.

B. Beam Splitters

The performance of a four-port beam splitter, which is depicted in Fig. 11,

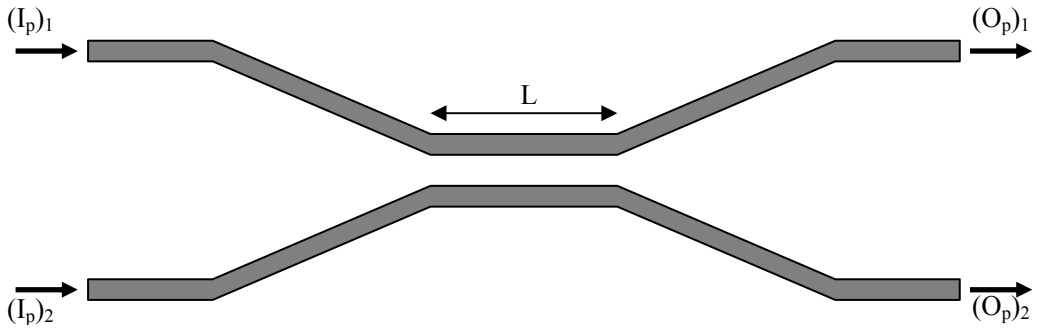

Fig. 11. Four-port beam splitter.

can be individually described in matrix notation as

$$O_p = C_p I_p \tag{74}$$

where

$$I_p = \begin{bmatrix} (I_p)_1 \\ (I_p)_2 \end{bmatrix} \tag{75}$$

$$O_p = \begin{bmatrix} (O_p)_1 \\ (O_p)_2 \end{bmatrix} \tag{76}$$

$$C_p = \begin{bmatrix} \cos(\kappa_p L) & i \cdot \sin(\kappa_p L) \\ i \cdot \sin(\kappa_p L) & \cos(\kappa_p L) \end{bmatrix}. \tag{77}$$

In these expressions, I and O represent the electric field amplitude for the input and the output modes, respectively. Subscript *P* refers to the polarization (TE or TM).

Subscript i=1, 2 designates the upper and lower ports, respectively. The elements in matrix *Cp* define the transfer functions of the beam splitter for *P*-polarization. The factor κ_p represents the inter-waveguide coupling coefficient and L is the effective length of the coupling region.

C. Non-Phase Matched Wavelengths

When an incident beam with polarization *P* and wavelength $\lambda_1, \lambda_2, \ldots\ldots \lambda_n$ enters the upper arm of the multiplexer (Fig. 10), it splits by a certain ratio into two beams as it passes through the first beam splitter. For wavelengths that do not satisfy the phase-matched condition $\lambda=\Lambda\ |\Delta n|$, where Λ is the spatial period of the index grating that is produced from the strain inducing strips on the surface and $|\Delta n|$ is the birefringence in the waveguide, the separated beams proceed through the upper and lower waveguide arms of the interferometer toward the second splitter without undergoing any polarization conversion. Because of the half-wavelength optical path difference between the upper and lower waveguide arms, the two beams enter the interaction region of the second beam splitter with a π-phase difference and proceed through. Assuming identical splitters of the same splitting ratio, the beams for the non phase-matched wavelengths recombine and emerge from the upper output port of the multiplexer. This behavior can be verified using matrix notation, by expressing the multiplexer output as

$$O_p = C_p M_\pi C_p I_p \tag{78}$$

with M_π signifying the matrix that describes the π-radian relative phase shift due to the half wavelength path difference, and is given by

$$M_\pi = \begin{bmatrix} 1 & 0 \\ 0 & -1 \end{bmatrix}. \tag{79}$$

Substituting (75)-(77) and (79) into (78) yields

$$\begin{bmatrix} (O_p)_1 \\ (O_p)_2 \end{bmatrix} = \begin{bmatrix} \cos^2(\kappa_p L)\cdot(I_p)_1 + \sin^2(\kappa_p L)\cdot(I_p)_1 \\ i\cdot\cos\ (\kappa_p L)\cdot\sin\ (\kappa_p L)\cdot(I_p)_1 - i\cdot\cos\ (\kappa_p L)\cdot\sin\ (\kappa_p L)\cdot(I_p)_1 \end{bmatrix}. \tag{80}$$

Using the trigonometric identity $\cos^2 A+\sin^2 A=1$, the above reduces to $(O_p)_1=(I_p)_1$ and $(O_p)_2=0$. Because of symmetry, if the incident beam is coupled into the lower input port i.e. $(I_p)_1=0$ and $(I_p)_2\neq 0$, it will emerge from the lower output, or $(O_p)_2=(I_p)_2$ and $(O_p)_1=0$.

D. Phase Matched Wavelength

In the case of a wavelength that satisfies the phase-matched condition $\lambda=\Lambda\,|\Delta n|$, a polarization conversion occurs in the upper and lower waveguide arms between the incident polarization P and output polarization, $\hat{P}$. Hence, the light passes through the first splitter with polarization P and through the second splitter with polarization $\hat{P}$. Furthermore, in addition to the π-radian phase difference resulting from the optical path length difference, another π-radian phase difference is acquired from the relative spatial displacement of the coupling regions in the waveguide arms by Λ/2. As the beams advance into the coupling region of the second splitter, the phase-matched wavelength can be made to emerge out from the lower output port of the multiplexer i.e. the phase-

matched wavelength is tapped out or allowed to drop, provided the relaxed beam splitter requirement is satisfied. This requirement can be determined by expressing the multiplexer (Fig. 10) output in matrix notation as

$$O_{\hat{p}} = C_{\hat{p}} M_{\pi} M_{\pi} C_{p} I_{p} . \tag{81}$$

Because $M_{\pi} M_{\pi}$ equals the unitary matrix, the above reduces to

$$O_{\hat{p}} = C_{\hat{p}} C_{p} I_{p} . \tag{82}$$

Using the trigonometric identities

$$\begin{aligned} \cos(A+B) &= \cos A \cdot \cos B - \sin A \cdot \sin B \\ \sin(A+B) &= \sin A \cdot \cos B + \cos A \cdot \sin B \end{aligned} \tag{83}$$

and substituting equation (82)

$$C_{\hat{p}} C_{p} = \begin{bmatrix} \cos(\Theta) & i\sin(\Theta) \\ i\sin(\Theta) & \cos(\Theta) \end{bmatrix} \tag{84}$$

where the argument becomes

$$\Theta = \kappa_{TE} L + \kappa_{TM} L . \tag{85}$$

To insure that the phase matched wavelength will emerge from the lower output port, $\Theta = \kappa_{TE} L + \kappa_{TM} L$ should be $\pi/2$. Then (84) becomes

$$C_{\hat{p}}C_p = \begin{bmatrix} 0 & i \\ i & 0 \end{bmatrix}. \tag{86}$$

The power transfer coefficient in a directional type beam splitter (as in Fig.10) from a waveguide "A" to a neighboring waveguide "B" for a polarization of *P* is

$$f_p = \left|c_p\right|_{ij}^2 = \left|i\sin(\kappa_p L)\right|^2. \tag{87}$$

When both polarizations (TE and TM) are present, then (87) becomes

$$f_{TE} + f_{TM} = \sin^2(\kappa_{TE}L) + \sin^2(\kappa_{TM}L). \tag{88}$$

If the condition $\Theta = \kappa_{TE}L + \kappa_{TM}L = \pi/2$ can be satisfied, (88) reduces to

$$f_{TE} + f_{TM} = \sin^2(\kappa_{TE}L) + \sin^2(\frac{\pi}{2} - \kappa_{TE}L) = \sin^2(\kappa_{TE}L) + \cos^2(\kappa_{TE}L) = 1 \tag{89}$$

or simply

$$f_{TE} + f_{TM} = 1. \tag{90}$$

Equation (90) is the required condition that must be satisfied for the relaxed beam splitter, which would then make it possible to drop the phase matched wavelength from the lower output port of the multiplexer.

If directional type, four-port beam splitter (Fig. 11) could be produced to satisfy equation (90), the stringent requirement of a polarization beam splitter can be relaxed. This would considerably facilitate the realization of tunable add-drop multiplexers.

Applying a voltage to the electrodes changes the birefringence $|\Delta n|$ value through the linear electro-optic effect. For a fixed period Λ, this makes a different wavelength λ satisfy the phase-matched condition, and hence provides a means for selecting the drop wavelength.

E. Spatially Periodic Strain-Induced Grating

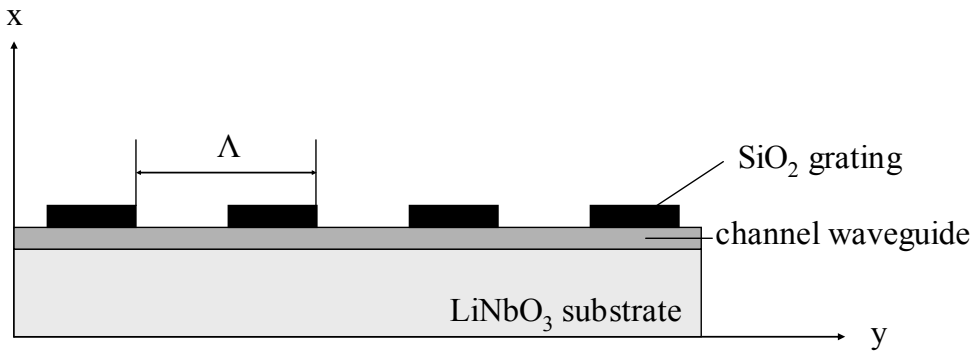

Fig. 12. Longitudinal view of the periodic index grating.

The mode conversion has been discussed in the previous chapter. To realize the conversion on a channel waveguide via a photoelastic effect, a spatially periodic strain-induced index grating is required. The periodic index grating in this study is made by a strain inducing SiO_2 film on the top of a $LiNbO_3$ substrate as shown in Fig. 12. The SiO_2 film is deposited on the surface of the $LiNbO_3$ substrate at an elevated temperature, and due to the difference between their thermal expansion coefficients, the $LiNbO_3$ substrate tends to expand much more than the SiO_2 film at the higher temperature. The thermal expansion coefficients of $LiNbO_3$ and SiO_2 are 1.59×10^{-5} and 5.4×10^{-7} [23], respectively. After cooling down to room temperature, a compressive strain is induced

because the SiO_2 film is compressed by the $LiNbO_3$ substrate, which has a larger thermal expansion coefficient.

The relevant strain-stress equation is generally given by

$$\begin{bmatrix} S_1 \\ S_2 \\ S_3 \\ S_4 \\ S_5 \\ S_6 \end{bmatrix} = \begin{bmatrix} s_{11} & s_{12} & s_{13} & s_{14} & s_{15} & s_{16} \\ s_{12} & s_{22} & s_{23} & s_{24} & s_{25} & s_{26} \\ s_{13} & s_{23} & s_{33} & s_{34} & s_{35} & s_{36} \\ s_{14} & s_{24} & s_{34} & s_{44} & s_{45} & s_{46} \\ s_{15} & s_{25} & s_{35} & s_{45} & s_{55} & s_{56} \\ s_{16} & s_{26} & s_{36} & s_{46} & s_{56} & s_{66} \end{bmatrix} \begin{bmatrix} T_1 \\ T_2 \\ T_3 \\ T_4 \\ T_5 \\ T_6 \end{bmatrix} + \begin{bmatrix} \alpha_x \Delta T \\ \alpha_y \Delta T \\ \alpha_z \Delta T \\ 0 \\ 0 \\ 0 \end{bmatrix} \tag{91}$$

where S_1-S_6 are the strains, T_1-T_6 are the stresses, and s_{11}-s_{66} are the compliances.

For the modeling of optical devices using such relations, it is a prerequisite to analyze and evaluate the stress and strain distributions. The Finite Element Method (FEM) provides one approach for performing the analysis. There are several commercial software packages that use FEM. Fig. 13 shows the simulated distribution of shear strain(S_6) in SiO_2 gratings on a $LiNbO_3$ substrate. For this simulation, commercial software (COMSOL Multiphysics 3.0) was used and 385^{o}C and 1.5 μm were applied the elevated temperature and the SiO_2 thickness, respectively. The shear strain was distributed periodically along the SiO_2 gratings. Maximum peaks of the shear strain are appear at the edges of the gratings inside the substrate. The strain is strongest near the surface and becomes weaker with distance away from the surface.

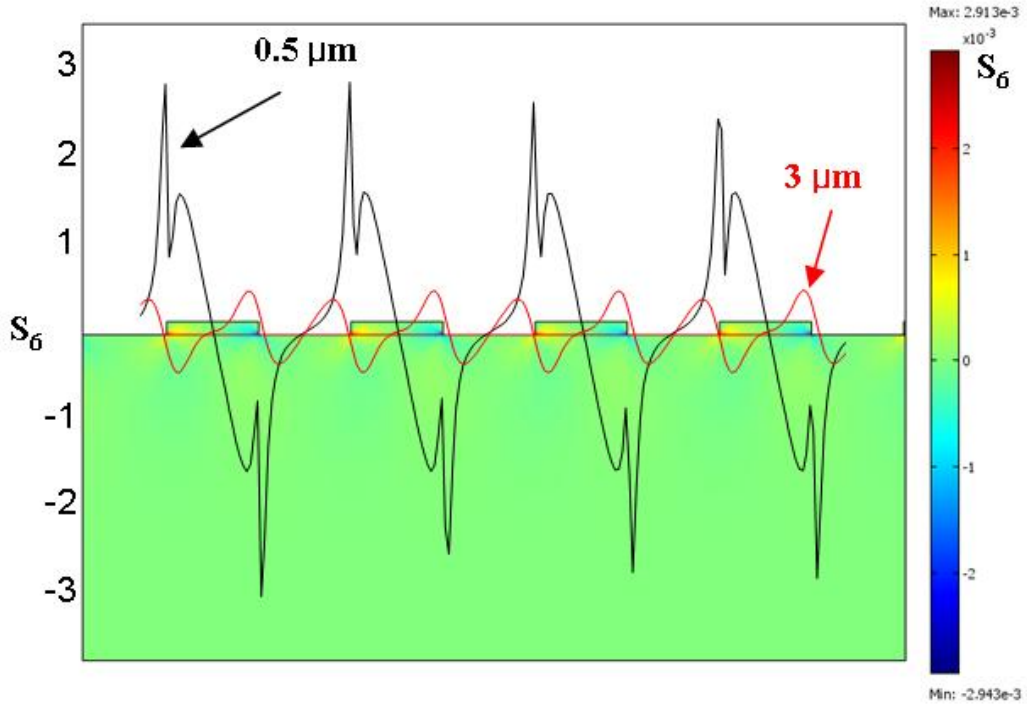

Fig. 13. Simulated distribution of shear strain (S_6) for the SiO_2 grating on the $LiNbO_3$ at depths of 0.5 and 3μm beneath the surface of the substrate.

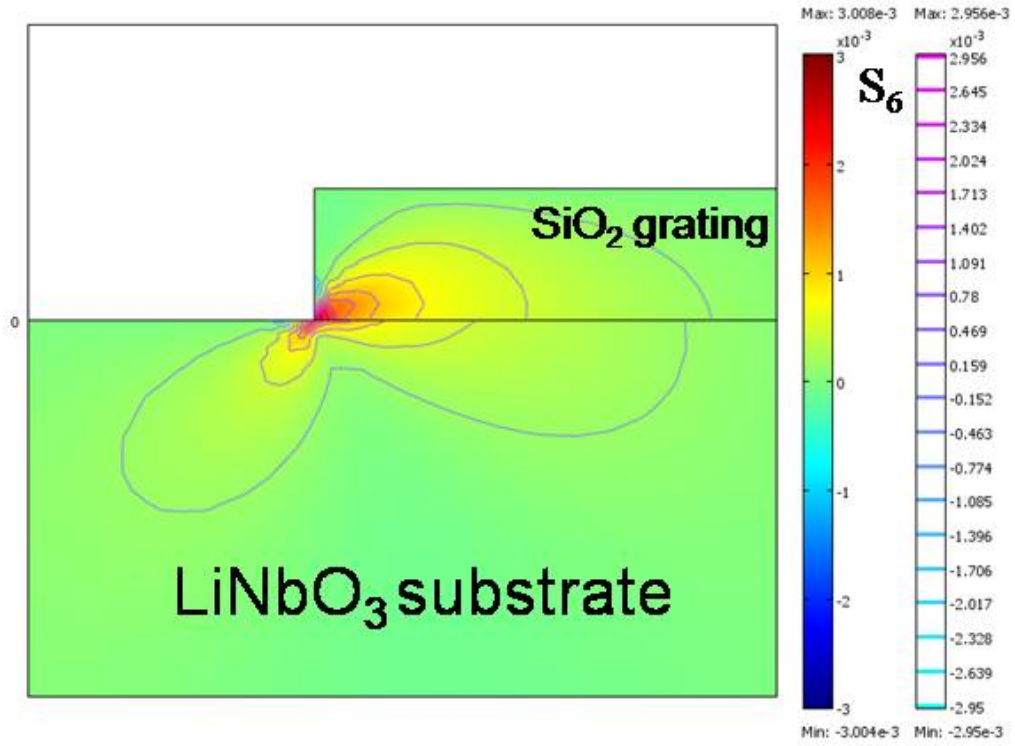

Fig.14. Magnified distribution of shear strain constant contours at the interface between the SiO_2 grating on the $LiNbO_3$.

Fig. 14 shows a closer view of the shear strain constant contours simulated with the same parameters as Fig. 13. The periodic distribution of strain-shear S_6 component promotes polarization coupling between TE and TM through Δn_5, via the elasto-optic effect. Only the displacement along the y-direction from (x, y, z) to (x, y+u_y, z) is relevant for the guided wave. The displacement u_x is continuous over the waveguide and does not contribute to S_6, hence [24]

$$S_6 = \frac{1}{2}\frac{\partial u_y}{\partial x}. \tag{92}$$

The photoelastic tensor $P_{\alpha\beta}$ of a $LiNbO_3$ substrate is [21]:

$$P_{\alpha\beta} = \begin{pmatrix} P_{11} & P_{12} & P_{13} & P_{14} & 0 & 0 \\ P_{12} & P_{11} & P_{13} & -P_{14} & 0 & 0 \\ P_{13} & P_{13} & P_{33} & 0 & 0 & 0 \\ P_{41} & -P_{41} & 0 & P_{44} & 0 & 0 \\ 0 & 0 & 0 & 0 & P_{44} & P_{41} \\ 0 & 0 & 0 & 0 & P_{14} & \tfrac{1}{2}(P_{11}-P_{12}) \end{pmatrix}. \tag{93}$$

Based on the earlier expressions shown in equations (54) and (56), the induced refractive index change Δn_5 caused by the photoelastic effect leads to the polarization conversion. By substituting equation (91) into (41) with only the shear strain component S_6, Δn_5 is obtained as

$$\Delta n_5 = -\frac{1}{2}\bar{n}^3 P_{41} S_6 \tag{94}$$

with $\bar{n} = \sqrt{n_o n_e}$, where n_o and n_e are ordinary and extraordinary refractive indices, respectively. The maximum strain component S_6 which appears at the corner of the

interface between SiO_2 and $LiNbO_3$ as shown in Fig. 14, is calculated using the referenced commercial software [25] for a 1.5μm thick SiO_2 film deposited at 385°C, and a periodic pattern with Λ = 21μm and has a magnitude $|S_6|$ of 3.0×10^{-3}. Using P_{41} = -0.15 [26], and $\bar{n}\sim 2.17$. ($n_o\sim 2.21$ and $n_e\sim 2.14$ at 24.5°C for 1550nm wavelength [27]) the calculated index change Δn_5 is $\sim 2.3\times10^{-3}$.

F. TE↔TM Polarization Mode Converter

A polarization mode converter can be produced in a single-mode Ti-indiffused channel waveguide with a spatially periodic strain-induced index grating on a $LiNbO_3$ substrate, as drawn in Fig. 15.

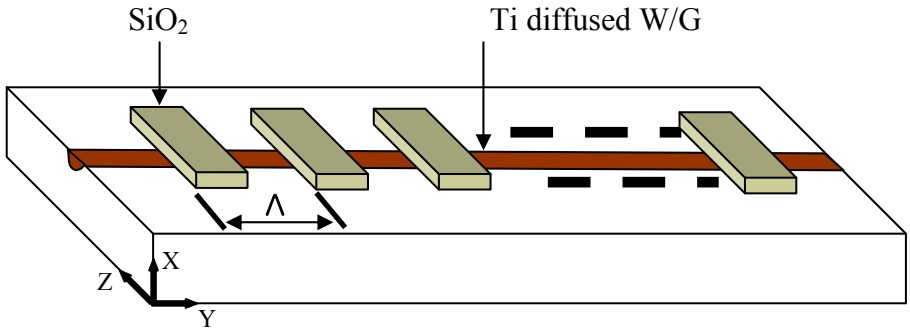

Fig. 15. The basic structure of a polarization mode converter.

Assuming a TM-polarized light is coupled into the channel waveguide and based on the coupled-mode theory [18], discussed in the previous chapter, the normalized transmitted TE-polarized intensity of the converter is given by

$$I_{out}(L)=\frac{\left|A_{TE}(L)\right|^2}{\left|a_o\right|^2}=\frac{\kappa^2}{(\kappa^2+\delta^2)}\sin^2\left[\sqrt{(\kappa^2+\delta^2)}\,L\right] \tag{95}$$

where a_0 is the amplitude of input light and L = NΛ with N being the total number of periods of the uniform grating, κ is the coupling coefficient and κL = π/2 for complete TM→TE mode conversion. In the conversion process, the wavelength deviation Δλ from the phase-matched wavelength λ_o introduces a phase-mismatch factor δ which can be expressed as [28]

$$\delta(\Delta\lambda)\cong\Delta\lambda\left[\frac{d}{d\lambda}\left(\frac{\beta_{TM}(\lambda)-\beta_{TE}(\lambda)}{2}\right)\right]\Bigg|_{\lambda=\lambda_o}=-\frac{\Delta\lambda}{\lambda_o}\frac{\pi}{\Lambda}\frac{\Delta n_g(\lambda_o)}{\Delta n_p(\lambda_o)} \tag{96}$$

with

$$\begin{aligned}\Delta n_p(\lambda_o)&=n_{TM}(\lambda_o)-n_{TE}(\lambda_o)\\ \Delta n_g(\lambda_o)&=\Delta n_p(\lambda_o)-\lambda_o\left(\frac{d\Delta n_p(\lambda_o)}{d\lambda}\right)\Bigg|_{\lambda=\lambda_o}\end{aligned} \tag{97}$$

where $\Delta n_p(\lambda_o)$ and $\Delta n_g(\lambda_o)$ denote the phase and group effective index differences, respectively, between the TE and TM modes at the design wavelength λ_o. Neglecting $\Delta n_g(\lambda_o)$ for first order approximation, the factor δ reduces to

$$\delta(\Delta\lambda)=-\frac{\Delta\lambda}{\lambda_o}\frac{\pi}{\Lambda}. \tag{98}$$

Substituting equation (98) into (95) with κL = π/2 for the complete conversion, the converted output intensity I_{out} dependence upon the wavelength deviation Δλ is obtained as

$$I_{out}(\Delta\lambda)=\frac{\pi^2}{\pi^2+\left[2\delta(\Delta\lambda)L\right]^2}\sin^2\left(\frac{1}{2}\sqrt{\pi^2+\left[2\delta(\Delta\lambda)L\right]^2}\right). \tag{99}$$

The output transmission is highly wavelength-dependent, as shown in Fig. 16. The -3dB bandwidth (FWHM) of a polarization mode converter can be obtained by substituting equation (98) into (99) with 50% of the maximum intensity as [29]

$$(\Delta\lambda)_{FWHM} \sim 0.8\frac{\Lambda}{L}\lambda_o = 0.8\frac{\lambda_o}{N}. \tag{100}$$

From this theoretical approach, a calculated FWHM using λ_0=1535nm and N=500 is 2.456nm. Another important parameter for the characterization of a TE↔TM polarization mode converter is the conversion efficiency defined as

$$\eta_{TE} = \frac{(P_{out})_{TM}}{(P_{out})_{TE} + (P_{out})_{TM}} \tag{101}$$

for a TE-polarized input, and

$$\eta_{TM} = \frac{(P_{out})_{TE}}{(P_{out})_{TE} + (P_{out})_{TM}} \tag{102}$$

for a TM-polarized input, where $(P_{out})_{TE}$ and $(P_{out})_{TM}$ are TE- and TM-polarized output powers, respectively. The conversion efficiency is ideally equal to one, if complete polarization conversion occurs at the phase-matched wavelength.

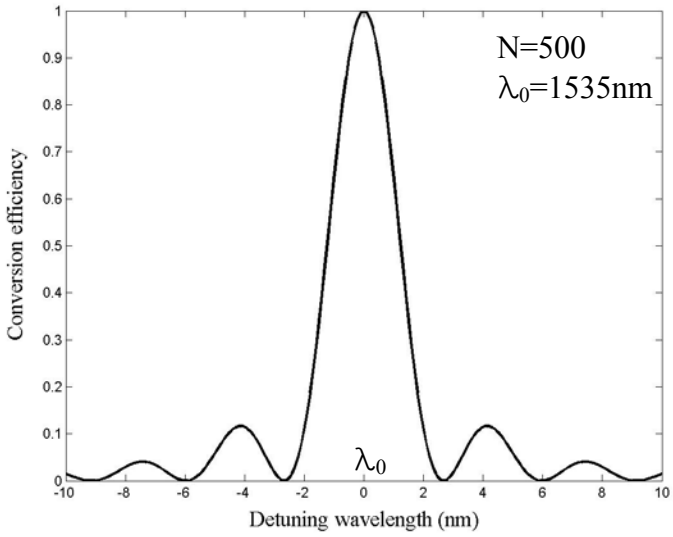

Fig.16. Normalized converted power transmission with wavelength deviation from center wavelength 1535nm for N = 500 periodic uniform gratings.

G. Electro-optic Tuning

To make an electro-optic tunable polarization mode converter a pair of electrodes need to be placed on either side of a channel waveguide. According to the linear electro-optic effect, refractive indices can be changed by introducing a z-component of an electrical field via an applied DC voltage across the electrodes. Since neither the applied electric field nor the optical mode field is uniform, an overlap factor Γ is introduced, which describes the overlap integral between the applied electric field and the optical field [30]. The refractive index of each polarization becomes

$$n_{TM} = n_x = n_o - \frac{1}{2}\Gamma_{TM} n_o^3 r_{13} \frac{V_T}{g}$$
$$n_{TE} = n_z = n_e - \frac{1}{2}\Gamma_{TE} n_e^3 r_{33} \frac{V_T}{g} \qquad (103)$$

where $\frac{V_T}{g}$ is the electric field (E_z) and g is the gap between electrodes; Γ_{TM} and Γ_{TE} are overlap factors for TM- and TE-polarized modes, respectively. The refractive index difference Δn between the two polarizations can be written as

$$\Delta n = \left| n_{TM} - n_{TE} \right| = \left| \left(n_o - n_e \right) - \frac{1}{2} \left(\Gamma_{TM} n_o^3 r_{13} - \Gamma_{TE} n_e^3 r_{33} \right) \frac{V_T}{g} \right|. \tag{104}$$

Substituting equation (104) into (73), and taking the derivative of λ_o with the applied DC tuning voltage V_T, the electro-optic tuning rate is expressed by

$$\frac{d\lambda_o}{dV_T} = \frac{1}{2} \left(\Gamma_{TM} n_o^3 r_{13} - \Gamma_{TE} n_e^3 r_{33} \right) \frac{\Lambda}{g} \tag{105}$$

where Λ is the spatial period of the grating.

H. Optical Transmission Characteristics of the Filter

To understand the performance of the filter, a detailed characterization of the modes in waveguides along the propagating direction is required, and can be accomplished by utilizing the features from each component in the filter, such as the beam splitter and the polarization converter. For simplicity, assume that the incident light is broadband, and TE polarization is launched at the upper input port.

For clarity, the detailed filter configuration is depicted in Fig. 17, the shaded areas represent the SiO_2 grating pads and Λ is the spatial period.

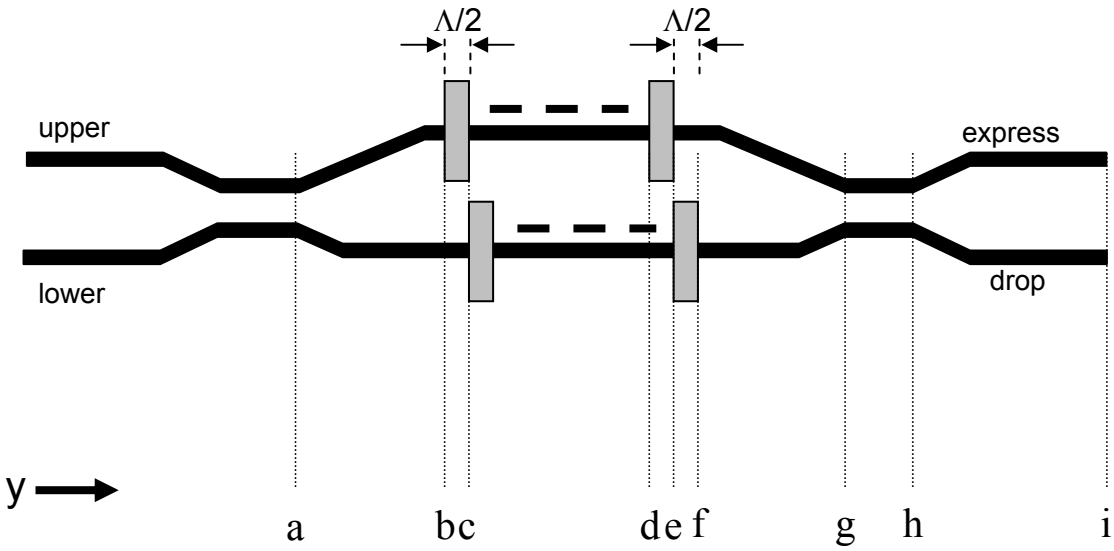

Fig. 17. The detailed filter configuration for the mode characterization.

At the first beam splitter, the incident beam coming from the upper input port splits between the two arms, depending on a splitting ratio which can be determined by the transfer function (as discussed previously).

1. At point "a"

Assuming the first beam splitter has a transfer function as in equation (77), the electric fields for a TE input beam in the upper and lower arms at point "a" can be written as

$$\begin{aligned} E_{0,u(y=a)} &= \cos(\kappa_{TE} L_{bs}) \cdot E_o \\ E_{0,l(y=a)} &= i \sin(\kappa_{TE} L_{bs}) \cdot E_o \end{aligned} \tag{106}$$

where subscript “l” and “u” indicate the lower and upper arms, respectively, E_0 is the amplitude of the incident beam, and L_{bs} is the length of the coupling region of the beam splitter.

2. At point “b”

The optical path difference between the two arms from point “a” to point “g” with a longer upper arm is $\frac{\lambda}{2}$. Therefore, the path difference from “a” to “b” between the upper and lower arms is $\frac{\lambda}{4}$, due to the symmetric structure of the interferometer.

After propagating to point “b” at the two arms, each electric field can be written by

$$\begin{aligned}\overline{E}_{u(y=b)} &= \cos(\kappa_{TE}L_{bs})\cdot E_0 e^{-i\beta_{TE}L^u_{ab}} = \cos(\kappa_{TE}L_{bs})\cdot E_0 e^{-i\beta_{TE}(L^l_{ab}+\frac{\lambda}{4})} = \cos(\kappa_{TE}L_{bs})\cdot E_0 e^{-i(\beta_{TE}L^l_{ab}+\frac{\pi}{2})} \\ \overline{E}_{l(y=b)} &= i\sin(\kappa_{TE}L_{bs})\cdot E_0 e^{-i\beta_{TE}L^l_{ab}}\end{aligned}. \quad (107)$$

3. At point “e” in the upper arm

For the phase matched wavelength λ_0 in the upper arm, which completely converts to a TM polarization and accumulates $\frac{\pi}{2}$ phase over the conversion region length L_0, the field can bee written as

$$E_{u(y=e)} = E_{u(y=b)}\cdot e^{-i(\beta_{TE}L_0+\frac{\pi}{2})} = \cos(\kappa_{TE}L_{bs})\cdot E_0 e^{-i(\beta_{TE}L^l_{ab}+\frac{\pi}{2})} e^{-i(\beta_{TE}L_0+\frac{\pi}{2})}. \quad (108)$$

4. At point "f" in the upper arm

After exiting from the polarization conversion region, the converted polarization at the phase matched wavelength λ_0 accumulates an additional phase $\beta_{TM} L_{ef}^{u} = \beta_{TM} \frac{\Lambda}{2}$. The electric field at point "f" is expressed as

$$\overline{E}_{u(y=f)} = \overline{E}_{u(y=e)} \cdot e^{-i\beta_{TM} \frac{\Lambda}{2}} = \cos(\kappa_{TE} L_{bs}) \cdot E_0 e^{-i(\beta_{TE} L_{ab}^{l} + \frac{\pi}{2} + \beta_{TE} L_0 + \frac{\pi}{2} + \beta_{TM} \frac{\Lambda}{2})}. \quad (109)$$

5. At point "c" in the lower arm

At the lower arm, the input light accumulates an additional $\beta_{TE} \frac{\Lambda}{2}$ phase change. Hence, the electric field for the lower arm at point "c" is

$$\overline{E}_{l(y=c)} = \overline{E}_{l(y=b)} e^{-i\beta_{TE} \frac{\Lambda}{2}} = i \sin(\kappa_{TE} L_{bs}) \cdot E_0 e^{-i(\beta_{TE} L_{ab}^{l} + \beta_{TE} \frac{\Lambda}{2})}. \quad (110)$$

6. At point "f" in the lower arm

For the phase matched wavelength λ_0, the input light in the lower arm is fully converted to a TM mode, and also accumulates an additional phase of $\frac{\pi}{2}$, similar to the case of the upper arm, i.e.

$$\overline{E}_{l(y=f)} = \overline{E}_{l(y=c)} e^{-i(\beta_{TE} L_0 + \frac{\pi}{2})} = i \sin(\kappa_{TE} L_{bs}) \cdot E_0 e^{-i(\beta_{TE} L_{ab}^{l} + \beta_{TE} \frac{\Lambda}{2} + \beta_{TE} L_0 + \frac{\pi}{2})}. \quad (111)$$

7. At point "g" in the lower arm

During the propagation from "f" to "g", the light in each arm acquires an additional $\beta_{TM} L_{fg}$ phase. Also there is an additional $\frac{\lambda}{4}$ phase difference between the upper and lower arms. Thus, the electric field of the upper and lower arms can be written as

$$\begin{aligned} \overline{E}_{u(y=g)} &= \overline{E}_{u(y=f)} \cdot e^{-i(\beta_{TM} L^{l}_{fg} + \frac{\pi}{2})} = \cos(\kappa_{TE} L_{bs}) \cdot E_0 e^{-i(\beta_{TE} L^{l}_{ab} + \frac{\pi}{2} + \beta_{TE} L_0 + \frac{\pi}{2} + \beta_{TM} \frac{\Lambda}{2} + \beta_{TM} L^{l}_{fg} + \frac{\pi}{2})} \\ \overline{E}_{l(y=g)} &= \overline{E}_{l(y=f)} e^{-i\beta_{TM} L^{l}_{fg}} = i \sin(\kappa_{TE} L_{bs}) \cdot E_0 e^{-i(\beta_{TE} L^{l}_{ab} + \beta_{TE} \frac{\Lambda}{2} + \beta_{TE} L_0 + \frac{\pi}{2} + \beta_{TM} L^{l}_{fg})} . \end{aligned} \tag{112}$$

Since the transfer function needs to be applied for a TM polarization, the total number of electric fields at the express (upper) and drop (lower) output ports at point i are

$$\begin{aligned} \overline{E}_{out,ex} &= \cos(\kappa_{TM} L_{bs}) \cdot E_{u(y=g)} e^{-i\beta_{TM} L_{gi}} + i \sin(\kappa_{TM} L_{bs}) \cdot E_{l(y=g)} e^{-i\beta_{TM} L_{gi}} \\ \overline{E}_{out,dr} &= i \sin(\kappa_{TM} L_{bs}) \cdot E_{u(y=g)} e^{-i\beta_{TM} L_{gi}} + \cos(\kappa_{TM} L_{bs}) \cdot E_{l(y=g)} e^{-i\beta_{TM} L_{gi}} . \end{aligned} \tag{113}$$

Substituting equation (112) into (113), the total electric field at the express port can be defined as

$$\begin{aligned} \overline{E}_{out,ex} &= \cos(\kappa_{TM} L_{bs}) \cos(\kappa_{TE} L_{bs}) E_0 e^{-i(\beta_{TE} L^{l}_{ab} + \frac{\pi}{2} + \beta_{TE} L_0 + \frac{\pi}{2} + \beta_{TM} \frac{\Lambda}{2} + \beta_{TM} L_{fg} + \frac{\pi}{2} + \beta_{TM} L_{gi})} \\ &\quad - \sin(\kappa_{TM} L_{bs}) \sin(\kappa_{TE} L_{bs}) E_0 e^{-i(\beta_{TE} L^{l}_{ab} + \beta_{TE} \frac{\Lambda}{2} + \beta_{TE} L_0 + \frac{\pi}{2} + \beta_{TM} L_{fg} + \beta_{TM} L_{gi})} . \end{aligned} \tag{114}$$

Substituing $\kappa_{TE} L + \kappa_{TM} L = \frac{\pi}{2}$ into (114), thus yields

$$\begin{aligned} \overline{E}_{out,ex} &= \cos(\frac{\pi}{2} - \kappa_{TE} L_{bs}) \cos(\kappa_{TE} L_{bs}) E_0 e^{-i(\beta_{TE} L^{l}_{ab} + \frac{\pi}{2} + \beta_{TE} L_0 + \frac{\pi}{2} + \beta_{TM} \frac{\Lambda}{2} + \beta_{TM} L_{fg} + \frac{\pi}{2} + \beta_{TM} L_{gi})} \\ &\quad - \sin(\frac{\pi}{2} - \kappa_{TE} L_{bs}) \sin(\kappa_{TE} L_{bs}) E_0 e^{-i(\beta_{TE} L^{l}_{ab} + \beta_{TE} \frac{\Lambda}{2} + \beta_{TE} L_0 + \frac{\pi}{2} + \beta_{TM} L_{fg} + \beta_{TM} L_{gi})} \end{aligned}$$

$$= \sin(\kappa_{TE} L_{bs}) \cos(\kappa_{TE} L_{bs}) E_0 e^{-i(\beta_{TE} L'_{ab} + \frac{\pi}{2} + \beta_{TE} L_0 + \frac{\pi}{2} + \beta_{TM} \frac{\Lambda}{2} + \beta_{TM} L_{fg} + \frac{\pi}{2} + \beta_{TM} L_{gi})}$$

$$- \cos(\kappa_{TE} L_{bs}) \sin(\kappa_{TE} L_{bs}) E_0 e^{-i(\beta_{TE} L'_{ab} + \beta_{TE} \frac{\Lambda}{2} + \beta_{TE} L_0 + \frac{\pi}{2} + \beta_{TM} L_{fg} + \beta_{TM} L_{gi})} . \quad (115)$$

Finally, this equation can be simplified as

$$\overline{E}_{out} = \sin(\kappa_{TE} L_{bs}) \cos(\kappa_{TE} L_{bs}) E_0 e^{-i(\beta_{TE} L'_{ab} + \beta_{TE} L_0 + \beta_{TM} L_{fg} + \beta_{TM} L_{gi} + \frac{\pi}{2})} \cdot \left[e^{-i(\beta_{TM} \frac{\Lambda}{2} + \pi)} - e^{-i(\beta_{TE} \frac{\Lambda}{2})} \right]. \quad (116)$$

The output light intensity can be presented as

$$I_{out} = \left| \overline{E}_{out} \right|^2 = (\overline{E}_{out}) \cdot (\overline{E}_{out})^* . \quad (117)$$

The total electric field at the express port can be represented as

$$I_{out} = \sin^2(\kappa_{TE} L_{bs}) \cos^2(\kappa_{TE} L_{bs}) E_0^2 \cdot \left[2 - e^{-i(\beta_{TM} \frac{\Lambda}{2} + \pi - \beta_{TE} \frac{\Lambda}{2})} - e^{-i(\beta_{TE} \frac{\Lambda}{2} - \pi - \beta_{TM} \frac{\Lambda}{2})} \right]$$

$$= \sin^2(\kappa_{TE} L_{bs}) \cos^2(\kappa_{TE} L_{bs}) E_0^2 \cdot \left[2 - 2 \left(\frac{e^{-i(\beta_{TM} - \beta_{TE}) \frac{\Lambda}{2} + \pi)} + e^{+i(\beta_{TM} - \beta_{TE}) \frac{\Lambda}{2} + \pi}}{2} \right) \right]$$

$$I_{out} = \sin^2(\kappa_{TE} L_{bs}) \cos^2(\kappa_{TE} L_{bs}) E_0^2 \cdot \left[2 - 2\cos[(\beta_{TM} - \beta_{TE}) \frac{\Lambda}{2} + \pi] \right]. \quad (118)$$

From the definition of the phase matched condition,

$$(\beta_{TM} - \beta_{TE}) \frac{\Lambda}{2} = \frac{2\pi}{\lambda_0} (n_o - n_e) \cdot \frac{\Lambda}{2} = \frac{2\pi}{\lambda_0} (n_o - n_e) \cdot \frac{1}{2} \cdot \frac{\lambda_0}{\Delta n} = \pi \quad (119)$$

where λ_0 is the phase matched wavelength and the special period is $\Lambda = \frac{\lambda_0}{\Delta n}$.

Therefore, $I_{out} = \sin^2(\kappa_{TE} L_{bs}) \cos^2(\kappa_{TE} L_{bs}) E_0^2 \cdot [2 - 2\cos(2\pi)] = 0$.

The total electric field for the drop port can be similarly obtained as

$$\overline{E}_{out,dr} = i\sin(\kappa_{TM}L_{bs})con(\kappa_{TE}L_{bs})E_0 e^{-i(\beta_{TE}L'_{ab}+\frac{\pi}{2}+\beta_{TE}L_0+\frac{\pi}{2}+\beta_{TM}\frac{\Lambda}{2}+\beta_{TM}L_{fg}+\frac{\pi}{2}+\beta_{TM}L_{gi})}$$

$$+ i\sin(\kappa_{TE}L_{bs})con(\kappa_{TM}L_{bs})E_0 e^{-i(\beta_{TE}L'_{ab}+\beta_{TE}\frac{\Lambda}{2}+\beta_{TE}L_0+\frac{\pi}{2}+\beta_{TM}L_{fg}+\beta_{TM}L_{gi})} . \quad (120)$$

Using the requirement for complete power transfer, $\kappa_{TE}L_{bs} + \kappa_{TE}L_{bs} = \frac{\pi}{2}$,

$$\overline{E}_{out,dr} = i\sin\left(\frac{\pi}{2} - \kappa_{TE}L_{bs}\right)con(\kappa_{TE}L_{bs})E_0 e^{-i(\beta_{TE}L'_{ab}+\frac{\pi}{2}+\beta_{TE}L_0+\frac{\pi}{2}+\beta_{TM}\frac{\Lambda}{2}+\beta_{TM}L_{fg}+\frac{\pi}{2}+\beta_{TM}L_{gi})}$$

$$+ i\cos\left(\frac{\pi}{2} - \kappa_{TE}L_{bs}\right)\sin(\kappa_{TE}L_{bs})E_0 e^{-i(\beta_{TE}L'_{ab}+\beta_{TE}\frac{\Lambda}{2}+\beta_{TE}L_0+\frac{\pi}{2}+\beta_{TM}L_{fg}+\beta_{TM}L_{gi})}$$

$$= i\cos^2(\kappa_{TE}L_{bs})E_0 e^{-i(\beta_{TE}L'_{ab}+\frac{\pi}{2}+\beta_{TE}L_0+\frac{\pi}{2}+\beta_{TM}\frac{\Lambda}{2}+\beta_{TM}L_{fg}+\frac{\pi}{2}+\beta_{TM}L_{gi})}$$

$$+ i\sin^2(\kappa_{TE}L_{bs})E_0 e^{-i(\beta_{TE}L'_{ab}+\beta_{TE}\frac{\Lambda}{2}+\beta_{TE}L_0+\frac{\pi}{2}+\beta_{TM}L_{fg}+\beta_{TM}L_{gi})} . \quad (121)$$

Designating A=$\cos^2(\kappa_{TE}L_{bs})$ and B=$\sin^2(\kappa_{TE}L_{bs})$, then A+B=1 and

$$\overline{E}_{out,dr} = iAE_0 e^{-i(\beta_{TE}L'_{ab}+\frac{\pi}{2}+\beta_{TE}L_0+\frac{\pi}{2}+\beta_{TM}\frac{\Lambda}{2}+\beta_{TM}L_{fg}+\frac{\pi}{2}+\beta_{TM}L_{gi})} + i(1-A)E_0 e^{-i(\beta_{TE}L'_{ab}+\beta_{TE}\frac{\Lambda}{2}+\beta_{TE}L_0+\frac{\pi}{2}+\beta_{TM}L_{fg}+\beta_{TM}L_{gi})}$$

$$= iE_0 e^{-i(\beta_{TE}L'_{ab}+\beta_{TE}L_0+\beta_{TM}L_{fg}+\beta_{TM}L_{gi}+\frac{\pi}{2})} \cdot \left[Ae^{-i(\beta_{TM}\frac{\Lambda}{2}+\pi)} + (1-A)e^{-i(\beta_{TE}\frac{\Lambda}{2})} \right]. \quad (122)$$

Therefore, the output intensity of the drop port is

$$I_{dr} = \left|\overline{E}_{out}\right|^2 = (\overline{E}_{out}) \cdot (\overline{E}_{out})^*$$

$$= E_0^2 \cdot \left[Ae^{-i(\beta_{TM}\frac{\Lambda}{2}+\pi)} + (1-A)e^{-i(\beta_{TE}\frac{\Lambda}{2})} \right] \cdot \left[Ae^{+i(\beta_{TM}\frac{\Lambda}{2}+\pi)} + (1-A)e^{+i(\beta_{TE}\frac{\Lambda}{2})} \right]$$

$$= E_0^2 \left[A^2 + (1-A)(1-A) + A(1-A) \cdot \left(e^{-i(\beta_{TM}\frac{\Lambda}{2}-\beta_{TE}\frac{\Lambda}{2}+\pi)} + e^{-i(\beta_{TE}\frac{\Lambda}{2}-\beta_{TM}\frac{\Lambda}{2}-\pi)} \right) \right]$$

$$= E_0^2\left[A^2 + (1-A)(1-A) + A(1-A)\cdot 2\left(\frac{e^{-i\left[(\beta_{TM}-\beta_{TE})\frac{\Lambda}{2}+\pi \right]} + e^{+i\left[(\beta_{TM}-\beta_{TE})\frac{\Lambda}{2}+\pi \right]}}{2} \right) \right]. \qquad (123)$$

$$= E_0^2\left[2A^2 + 1 - 2A + (2A - 2A^2)\cos\left((\beta_{TM} - \beta_{TE})\frac{\Lambda}{2} + \pi \right) \right] = E_0^2$$

In the phase matched condition, the cosine becomes one. Conclusively, the output light intensity at the drop port is E_0^2. This means that all of the input beams at the phase matched wavelength can be tapped out from the drop port.

For the case of a non phase matched condition, in other words $\lambda \neq \lambda_0$, efficient polarization mode conversion does not occur. Thus, there is only a π-radian phase difference between the upper and lower arms, due to the optical path difference. Therefore, for wavelength $\lambda \neq \lambda_0$ the express port shows E_0^2 of light intensity, but the drop port appears to show zero output intensity.

CHAPTER IV

DEVICE FABRICATION

The fabrication processes for channel waveguides, beam splitters, polarization mode converters and the filter are described in this chapter. The optimized conditions that are identified for producing each of these elements are not included in this chapter, but are listed in the next chapter. Detailed procedures of the relevant processes are given in the appendices.

A. Ti In-diffused Channel Waveguides and Beam Splitters in $LiNbO_3$

Among the different ways for making optical waveguides on a $LiNbO_3$ substrate, the Ti in-diffused [31] method is adopted in this work because of its well developed technology and ability to support both TE and TM polarization. The straight channel waveguides and beam splitters were initially fabricated by dicing a 1mm thick, 3 inch diameter, x-cut $LiNbO_3$ crystal wafer supplied by Crystal Technology Inc. (Palo Alto, CA) into appropriate sizes to make devices with the lightwave propagation along the y-direction. The wafer was diced into 12.7mm (in the z-direction) by 19mm (in the y-direction) for channel waveguides and beam splitters (Appendix 1). After dicing, samples were cleaned using various organic solvents and DI water (Appendix 2). Titanium films of different thicknesses (1025Å ~ 1200Å for both elements) were deposited onto the cleaned substrate surface by a DC sputtering process (Appendix 3).

After Ti-film deposition, the patterns of channel waveguides and splitters were delineated above the Ti film with an AZ-5214 photoresist produced by Clariant via a positive photolithography process (Appendix 4). Once the developed photoresist patterns satisfied requirements such as width of the waveguide and separation gap between waveguides, the samples were further cleaned in a barrel asher with O_2 plasma (Appendix 6) for 3 minutes to remove remained photoresist residues on exposed regions after being developed and hard baked under a vacuum at 135°C for 5 minutes to harden the photoresist for the later etching processes. The Ti film with hardened photoresist patterns was mainly etched away through reactive ion etching (RIE) (Appendix 7). It is extremely difficult to stop etching precisely at the interface of Ti and $LiNbO_3$ because the etching process in the used instrument was not uniform over the entire surface, and also the mixture of gases (Argon: 3sccm, Helium: 7.5sccm, and CHF_3: 30sccm,) used in the RIE could slightly etch through the $LiNbO_3$ substrate. Over-etching damages the surface and introduces optical loss. Hence, titanium film was etched until the remaining thickness was around 100Å. The residual Ti film was etched away using diluted hydrofluoric acid (HF) mixed with DI water at a 1:30 volume ratio. The wet-etching process is both isotropic and fast. A light can not be well confined in a Ti-diffused channel waveguide if under-etched, while over-etching reduces the width of waveguides and increases separation gaps. After etching, the photoresist was then removed by immersing into a photoresist stripper (Clariant AZ 300T) heated to 90°C for 15 minutes. The samples were then cleaned with liquid solvents (Appendix 2).

The Ti patterns for channel waveguides were designed with two different widths of 7μm and 8μm, and the delineated patterns for beam splitters consisted of a directional coupler with a splitting angle α and a central interaction region of gap d (ranging from 5μm to 13μm by a 2μm interval) and length L, as shown in Fig. 18. Appendix 8 gives more details about the beam splitters. The width of the Ti strip was carefully measured with 1000X of magnification under a microscope, and the Ti film thickness was determined from the average of 10 repeated measurements using a Dektak^3 Surface Profile Measuring System (Appendix 9).

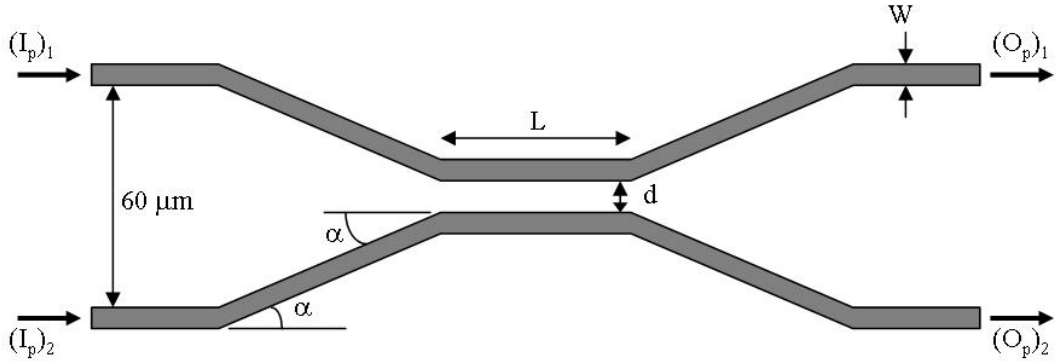

Fig. 18. The structure of a beam splitter with a splitting angle α and a gap between waveguides d.

Once satisfactory values for the width and thickness of the Ti-strip were confirmed, the samples were loaded at the center of the quartz tube of a furnace for diffusion at fixed set temperatures under wet air ambient condition. Diffusion temperatures ranged between 1025°C to 1035°C for 9 to 13 hours, depending on the

deposited Ti film thickness (Appendix 10). The wet air ambient was used to suppress the Li_2O out-diffusion [32]. The initial Ti thickness τ, diffusion temperature T, and diffusion time t were the three dominant parameters for fabricating high quality waveguides with a single mode, low propagation loss, and well-confined mode profiles for both the TE and TM polarizations, and also for the desired beam splitters. According to previous research, the diffusion temperature was more critical than the diffusion time, as the following equation [33] indicates

$$d = 2\sqrt{Dt} \tag{124}$$

with the diffusion coefficient D given by

$$D = D_o e^{-\frac{T_o}{T}} \tag{125}$$

where D_o is the bulk diffusivity and T_o is the activation temperature. Both are dependent upon the composition of a $LiNbO_3$ crystal. Generally, T_o and D_o are 2.5×10^4K and 2.5×10^{-4}cm^2 for $LiNbO_3$ (48.6 mole% of Li_2O), respectively [34]. Since the diffusion temperature is a critical factor during the lengthy metal diffusion process (9-13 hours in this research), it is very important to accurately calibrate the temperature so that it does not show any variation over the entire set of tested samples.

Finally, both ends of the samples were polished (Appendix 11) along the edges perpendicular to the waveguides for input/output coupling of light and optical characterization.

B. Zn Vapor Diffused Channel Waveguide and Beam Splitter in $LaTiO_3$

The low birefringence of $LiTaO_3$ relative to $LiNbO_3$ makes it an attractive material choice for DWDM optical filter applications. As such, relaxed beam splitters (RBSs) were initially fabricated and characterized in $LiTaO_3$. This effort, however, was later abandoned because the unavailability of large diameter $LiTaO_3$ wafers that would be required for the filter fabrication. This section describes the fabrication procedure that was used for making RBSs in $LiTaO_3$ by the method of Zn diffusion from vapor phase.

The fabrication process began with the dicing of a commercially purchased 1 inch (y) × 1 inch (z) × 1mm thick X-cut $LiTaO_3$ single crystal substrate (Crystal Technology Inc, Palo alto, CA) to the appropriate size of 17mm×12mm. Afterward, samples were cleaned (Appendix 1), a SiO_2 layer, which was used as a protective window during vapor diffusion, was deposited by the RF sputtering to a thickness of 5000Å. Straight channel waveguides and beam splitter patterns were delineated on a spun surface photoresist film using an image reversal process (Appendix 12). After hardening the photoresist pattern in a barrel asher (under vacuum at 135ºC for 3 min), dry etching of the exposed SiO_2 by reactive ion etching was used to open windows for the Zn vapor diffusion and then remained photoresist was

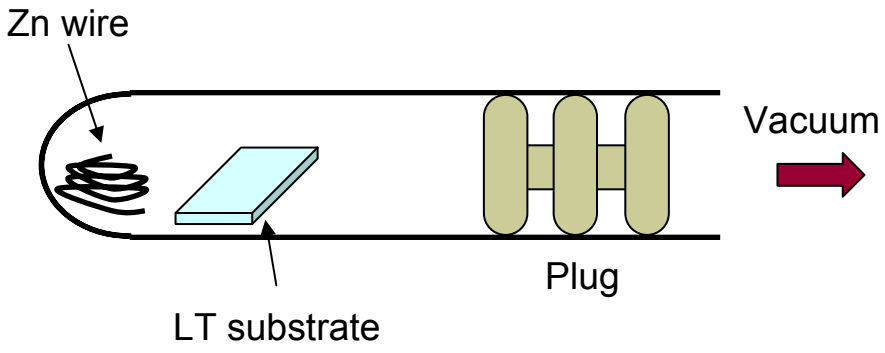

Fig. 19. Ampule arrangement for zinc vapor diffusion.

removed by the PR stripper. The diffusions were performed from the vapor phase in vacuum-sealed ampules of 38.83cm^3 in volume, each containing wire Zn metal and a $LiTaO_3$ substrate with delineated pattern in SiO_2, as shown in Fig. 19. Diffusions were carried out in 6hrs under different conditions on three separate samples, as described in Table 2. After diffusion, the SiO_2 films were etched off, the end edges of each sample were polished, and the crystals were repoled. Since the diffusions were carried out at temperatures above the Curie temperature of $LiTaO_3$ (~635^{o}C), the repoling procedure restores the electro-optic properties of the crystals.

Table 2. Diffusion conditions used for the formation of waveguide channels.

Sample	Amount of Zn (mg)	Diffusion Temperature (^{o}C)
S3	40	925
S7	40	935
S8	23.2	925

C. Tunable TE ↔ TM Polarization Mode Converters

A tunable polarization mode converter was formed with a spatially periodic strain-induced index grating on top of a single-mode, Ti-indiffused channel waveguide with polished end-edges and one pair of electrodes for electro-optic tuning. The structure of a tunable TE↔TM polarization mode converter is schematically drawn in Fig. 20.

The straight channel waveguide was fabricated by Ti-indiffusion in $LiNbO_3$ as described in the previous section and tested to check all of the properties for good optical waveguides such as single-mode propagation, low insertion loss, and a good confinement for both polarization modes. After that, one pair of electrodes was placed on both sides of the channel waveguide. Electrodes, patterns were delineated using an image reversal photolithography process (Appendix 12). To remove another source of optical loss, the patterns had to be carefully aligned not overlap with the waveguide.

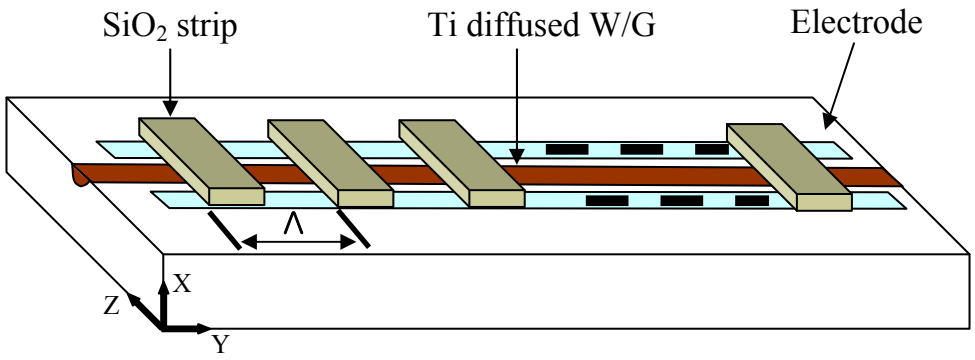

Fig. 20. The diagram of a tunable TE↔TM polarization mode converter.

The gap between electrodes was fixed at 17μm. The samples were then cleaned in a barrel asher using an O_2 descum for 3 minutes, to remove residual photoresist. After the descum process, multi-metal layers were deposited in order of Cr/Au/Ti with a thickness of 400Å/800Å/600Å, respectively, using e-beam evaporation (Appendix 13). The Cr layer was used to improve the adhesion between the metal layer and the $LiNbO_3$ substrate, and the Ti layer was used to prevent Au diffusion into the strain-inducing SiO_2 film that was deposited later at high temperature (>380°C). Electrode metal patterns were defined using a lift-off process by immersing the sample in acetone.

After the formation of electrodes, a spatially periodic strain-induced index grating was constructed as follows. The $LiNbO_3$ substrate with Ti-indiffused waveguides and electrodes was heated up at a rate of 4°C/min until it stabilized at 390°C, and a 1.54μm thick SiO_2 film was deposited by an e-beam evaporation at this elevated temperature with O_2 flowing (at a 1~2 sccm flow rate) inside the chamber. A heat lamp was automatically turned on and off by a heat controller to maintain a constant temperature during the deposition. After completing the SiO_2 deposition, the sample was kept inside the chamber with the O_2 continuously flowing until it slowly cooled down to room temperature. The O_2 flowing during the SiO_2 deposition was for preventing O_2 out-diffusion from the $LiNbO_3$ substrate. Using positive photolithography process, a uniform periodic grating of photoresist on the SiO_2 film was delineated with a longer dehydration time, a higher soft-bake temperature and a slower spinning speed (Appendix 5) than the parameter values that were used for the channel waveguide's delineation process due to a thicker SiO_2 film. The sample was then vacuum hard-baked at 135°C for 17 minutes, and

dry etched under the RIE system for 20 minutes with 350 watts of plasma power. The non-etched SiO_2-film residue after dry etching was completely removed by wet-etching in a buffered oxide etch (BOE) for 30~40 seconds. The photoresist on top of the SiO_2 grating patterns was removed by immersing the sample in a heated 90°C photoresist stripper for 15 minutes. After further cleaning, the sample was carefully inspected to ensure the realization of the required spatial period Λ of 21μm and no missing parts among the total number of 500 grating strips..

D. Electro-optically Tunable Add/Drop Filters

The electro-optically tunable add/drop filter was produced on an x-cut y-propagating $LiNbO_3$ substrate of 15mm width (z-axis) by 45mm long (y-axis). The actual diagram of the device structure is illustrated in Fig. 21. Four of these devices with different gaps in the beam splitter and lengths of the optical paths between splitters were included in one sample (Appendix 15). The detail dimensions of the filter design are described in Appendix 14.

The fabrication procedure for the electro-optically tunable add/drop filter was exactly the same as that of the previously explained tunable polarization mode converter. The complete filter consisted of three layers produced sequentially in the following order: Ti-indiffused waveguides, electro-optic tuning electrodes, and SiO_2 gratings. Initially, the Ti-indiffused waveguides incorporating two beam splitters and an asymmetric Mach-Zehnder interferometer were produced on a $LiNbO_3$ substrate using a 1200Å deposited Ti film thickness and diffusing at 1035°C for 9~10 hours.

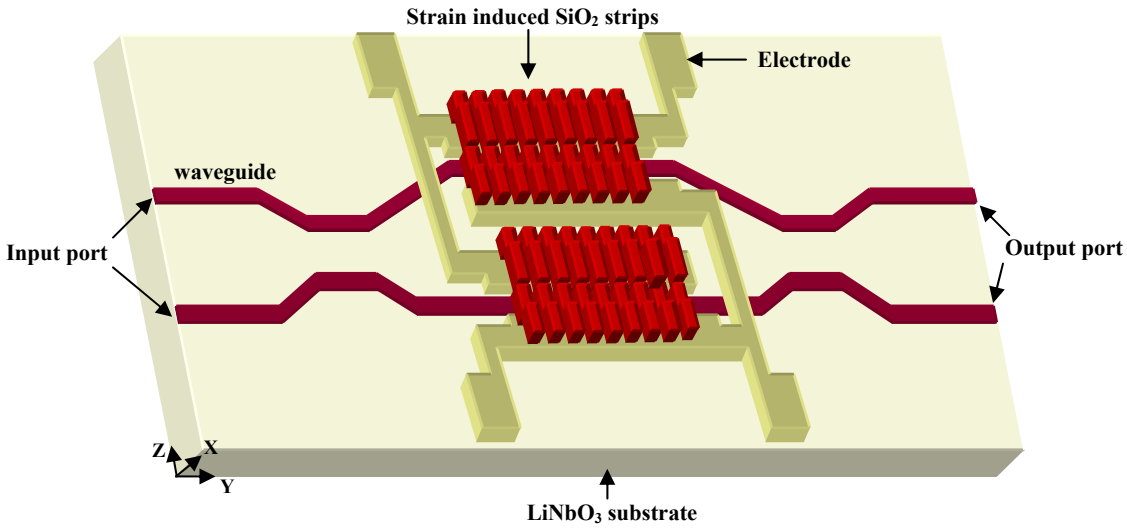

Fig. 21. The schematic of the complete tunable add/drop integrated filter structure.

Once the first layer was produced, the end edges were polished and optical characterization of the power from the two output ports was measured to verify the overall extinction ratio of the filter using fiber coupling, before proceeding to the next fabrication step. Second, Cr/Au/Ti metal electrodes with a gap of 17μm of the corresponding thicknesses 400Å/800Å/600Å were deposited on the $LiNbO_3$ substrate and formed using lift-off process. Third, the periodic strain-induced index gratings made from a 1.54μm thick SiO_2 film, which was deposited using an E-beam evaporation system at 390°C, was constructed on top of the electrode pairs. Finally, the complete tunable add/drop optical filter was characterized by optical testing with fiber coupling and a broadband laser source.

CHAPTER V

OPTICAL TESTING AND RESULTS ANALYSIS

The optical testing results for channel waveguides, beam splitters, and tunable TE↔TM polarization mode converters are given in this chapter. Also, the characteristics of the optically tunable add/drop filter with respect to insertion loss, polarization dependence, FWHM, electro-optic tuning, side-lobe, tuning range, tuning rate and tuning speed are presented. Suggestion for a future work is proposed.

A. Ti In-diffused Channel Waveguides and Beam Splitters in $LiNbO_3$

High quality optical channel waveguides are required for the efficient operation of integrated optical filter. The criteria for high quality channel waveguide include single mode propagation at the design wavelength, low insertion loss and good confinement of mode field distributions. These requirements should be satisfied for both TE and TM polarizations, and strongly depend on fabrication parameters. In the case of a Ti in-diffused waveguide, the quality of the Ti film, its initial thickness, the strip width, diffusion temperature, diffusion time and environment during diffusion can all affect the quality of the final optical waveguides.

To characterize the dependence of Ti in-diffused waveguides on these criteria, Ti diffused straight channel waveguides with different fabrication conditions were tested. The insertion loss of a waveguide can be calculated from measurement of intensity

before and after placing a waveguide within the optical path between two fibers, and using the defining relation in dB

$$\text{Insertion Loss (dB)} = -10 \cdot \log \frac{P_{out}}{P_{in}} \tag{126}$$

where P_{in} and P_{out} are the measured output powers before and after placing the waveguide, respectively. Fig. 22 shows the test setup for the optical insertion loss measurement. A pigtailed 1558.2nm distributed feedback (DFB) laser diode (Alcatel, Module: 1915-LMI) controlled by a current source (ILX Lightwave, Model LDC-3712) at 36.76mA and a setting temperature of 20^{o}C was used as an optical source to supply 1.0mW of optical power. The output of the laser diode was spliced to a single mode fiber (Corning SMF-28^{TM}) and the fiber was wound into a fiber polarization controller (Thorlabs Inc., Model FDC010) to switch the polarization mode of the input light. A high resolution x-y-z translation stage (Line Tool Co., Allentown, PA) was used to hold and manipulate the position of the sample. The output light from the polarization controller was launched into the channel waveguide through one polished end-edge. After the input light propagates through the sample, the output light from the opposite polished end-edge was coupled into another single mode fiber. The light emerging from the lens was focused onto a Ge photodetector (Newport, Model 818-IR). Then, output optical power was measured by an optical power meter (Newport, Model 1825-c).

The insertion loss variation with the Ti thickness and diffusion conditions for a 7μm wide straight channel waveguide on samples SN#1 to SN#4 are summarized in Table 3.

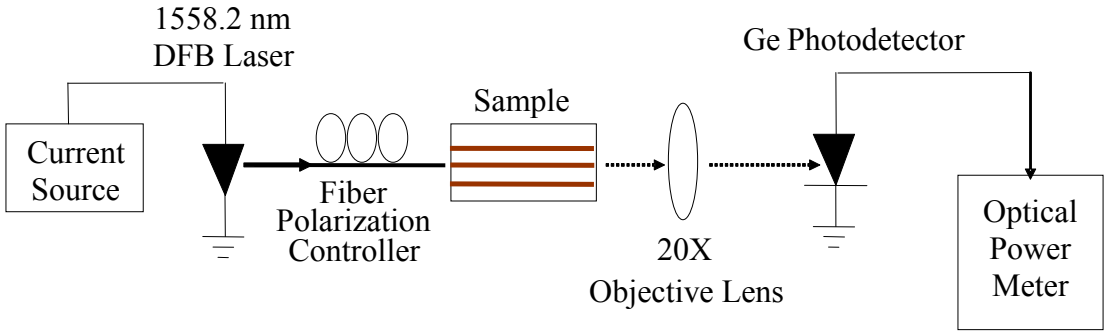

Fig. 22. The test setup for the insertion loss measurement.

All of the samples were fabricated with substrate dimensions of 19.0×12.7×1.0mm. Diffusion time was counted from the time when the temperature reached the desired set value till the time of turning off the furnace. After an initial diffusion of 9 hours, insertion losses for both the TE and TM polarizations were measured. Then, additional diffusions in increments of one hour were carried out and insertion loss measurements repeated. The listed results in Table 3 indicate that the insertion loss for TM polarization is larger than for TE polarization. The difference of insertion loss between both polarizations is much larger for the lower thicknesses of Ti-strips and shorter diffusion times. Samples SN#3 and SN#4 compare the effect of diffusion temperature for the case of same initial Ti film thickness.

Near field intensity mode profiles offer another important feature for characterizing channel waveguides. Fig.23 shows a near field intensity mode profile

measurement setup. The input light is DFB laser, which is the same as for the insertion loss measurement.

Table 3. Insertion loss of channel waveguides for TE and TM polarizations with various diffusion conditions and Ti thicknesses.

sample		SN#1		SN#2		SN#3		SN#4	
Ti thickness (Å)		1062		1106		1202		1202	
Diffusion Temperature (^{o}C)		1025		1025		1025		1035	
Insertion Loss (dB)	Diffusion Time	TE	TM	TE	TM	TE	TM	TE	TM
	9 hr	2.95	9.45	2.68	7.94	2.23	3.26	2.32	2.86
	10 hr	1.77	5.78	2.09	5.17	2.55	2.48	2.57	2.67
	11 hr	3.52	3.83	2.31	4.71	2.19	2.29	2.26	2.22
	12 hr	3.82	4.17	2.67	3.81	1.96	2.45	2.09	2.62

After propagation through the sample, the beam emerging from the 20X objective lens was focused on a vibrating mirror and directed through a 100μm wide vertical or horizontal slit (vertical for transverse, horizontal for depth), which was the placed in front of a Ge photodetector. The vibrating mirror was driven with a DC voltage through a control circuit. Horizontal and vertical scans were obtained by rotating the mounted mirror assembly 90º relative to the vibration axis. The slit was inserted to improve the spatial resolution for the relatively large photodetecter diode area. The output power from the photodetector was delivered to the optical power meter which was connected to a computer via a NI-DAQ board (National Instruments – Data Acquisition) for display

and storage of the data. (See appendix 18 for detail connection) The LabVIEW program was used to obtain mode profile data from the optical power meter.

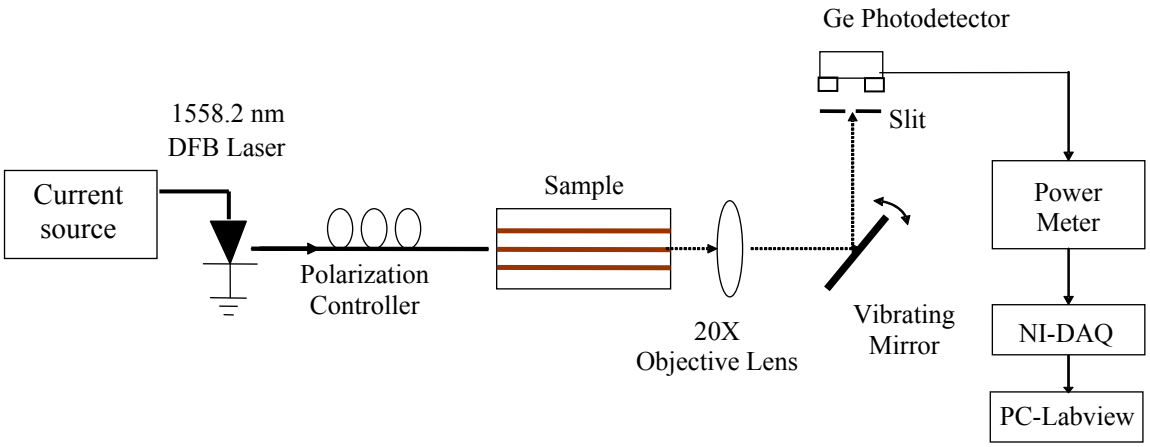

Fig. 23. The test setup of the field intensity mode profile measurement.

Fig. 24 shows the obtained mode profiles of transverse lateral and depth distributions for both the TE and TM polarizations on a 7μm wide waveguide in sample SN#4. The obtained images indicate that only single mode propagation is present for both the TE and TM polarizations in this waveguide, due to a single peak shown in the profile. The variation shows a symmetric Gaussian distribution for the horizontal scan, while an asymmetric profile is obtained in the vertical scan, corresponding to a significant difference in the refractive index at the air and waveguide interface.

The Full Width at Half Maximum (FWHM) was used to characterize the mode confinement of the waveguides. It can be calculated from the mode profile display, as shown in Fig. 25, using a directional coupler with a fixed known center to center separation of 67μm as a standard scale. The measured FWHM of 7μm and 8μm wide

channel waveguides of sample SN#4 for both the TE and TM polarizations are given in Table 4. Table 4 reveals that the TE-polarized mode has better confinement than the TM-polarized mode.

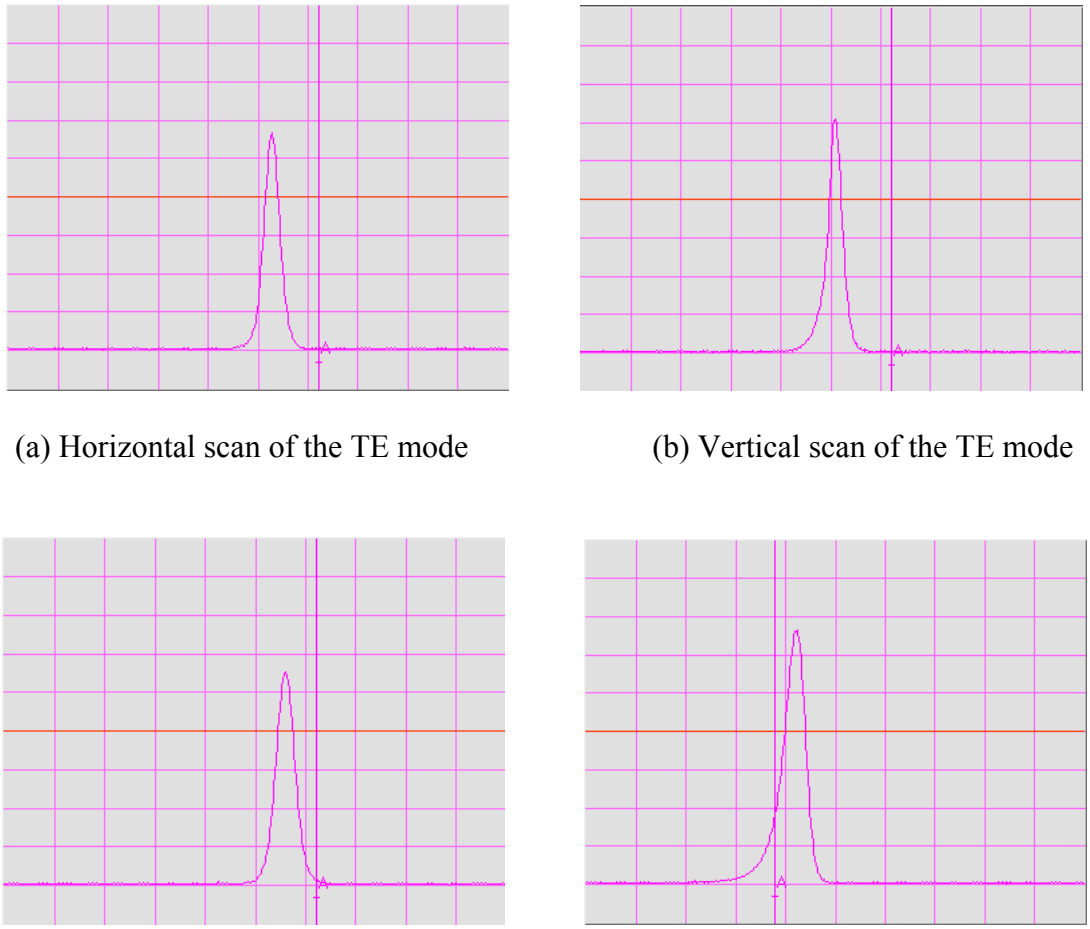

(a) Horizontal scan of the TE mode

(b) Vertical scan of the TE mode

(c) Horizontal scan of the TM mode

(d) Vertical scan of the TM mode

Fig. 24. Mode profiles of the 7μm wide channel waveguide on sample SN#4. The scale of the x and y axes are 10 mV/div and 200μs/div, respectively.

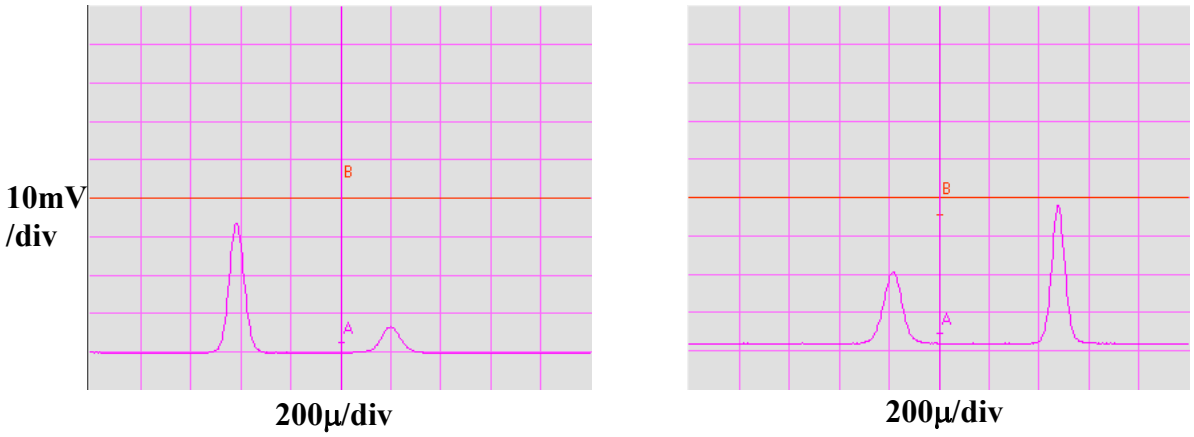

(a) (b)

Fig. 25. The output mode profile for both polarizations of a directional coupler diffused at 1025°C for 11h from a 1202 Å thick Ti film: (a) for the TE input polarization (power transfer coefficient=0.22) (b) for the TM input polarization (power transfer coefficient=0.63).

Table 4. Measured FWHM of 7µm and 8µm wide channel waveguides on sample SN#4 with a 1202Å Ti thickness and diffusion at 1035ºC for 10 hours.

Waveguide width	7µm		8µm	
	TM mode	TE mode	TM mode	TE mode
FWHM (µm) of horizontal scan	8.30	6.06	7.85	5.83
FWHM (µm) of vertical scan	8.30	7.18	8.75	6.73

The power splitting ratio (or power transfer coefficient), f_P, for the beam splitters was calculated by coupling light of polarization P (TE or TM) into one of the input ports i = 1 or 2 and measuring the output intensities at the two exit ports of the splitter, j = 1 and 2, as shown in Fig. 26. Then, the ratio of power output from port j ≠ i, was taken over the sum of the output powers from both ports, j = 1 and 2, for that polarization. For instance, in the case of light of polarization P (TE or TM) incident into port 1 [$(I_P)_1$ in (Fig.18)], the power splitting ratio was obtained from the ratio

$$f_P = \frac{P_{2P}}{P_{1P} + P_{2P}} \tag{127}$$

where P_{1P} and P_{2P} represent measured output powers at the straight-through port 1 and crossover port 2, respectively. The symmetry in the operation of the splitters, $(f_P)_{1j} = (f_P)_{2j} \equiv f_P$ for each polarization P, was confirmed by measuring the power splitting ratios with light coupled to input port1 [$(I_P)_1$ in (Fig.18)], and then repeating the measurements when the light was coupled to port 2 [$(I_P)_2$ in (Fig.18)].

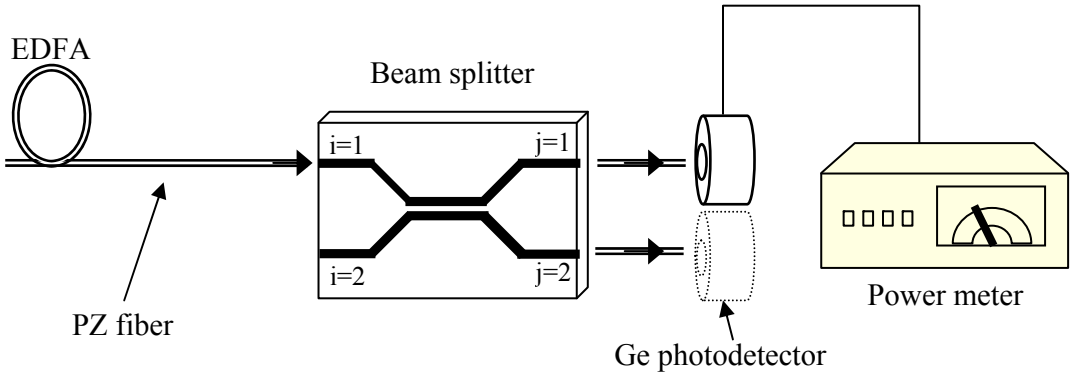

Fig. 26. The test arrangement for measuring the power transfer coefficient.

The variations of the sum of the measured power-transfer coefficients with separation gap d and diffusion times are shown in Fig. 27-(a) for sample SN#1 (of Table 3). The results reveal that the sum of the power-transfer coefficients add to one, and satisfy the requirement for the relaxed beam splitter equation (90) for a 11μm gap after 9 hours of diffusion. Fig.27-(b) shows the results of sample SN#2 (of Table 3). The trend of results is similar to Fig.27-(a). In this case, the requirements for the relaxed beam splitter are realized with a gap of 11μm after 10 hours of diffusion and 13μm after 12 hours of diffusion. The results for samples SN#3 and SN#4 (of Table 3), as depicted in Fig. 28, show that the beam splitters with an 11μm gap satisfy the requirements of the relaxed beam splitter [equation (90)] nearly after diffusion time of 12 hours and 10 hours, respectively. This indicates that coupling between the two parallel waveguides in the beam splitter structure is a periodic function of the coupling coefficient, which is mainly dependent upon the separation. Using the Ti film thickness, the diffusion temperature and time as fabrication control parameters, it should be possible to identify other combinations of these variables that would also satisfy the design criterion for a relaxed beam splitter.

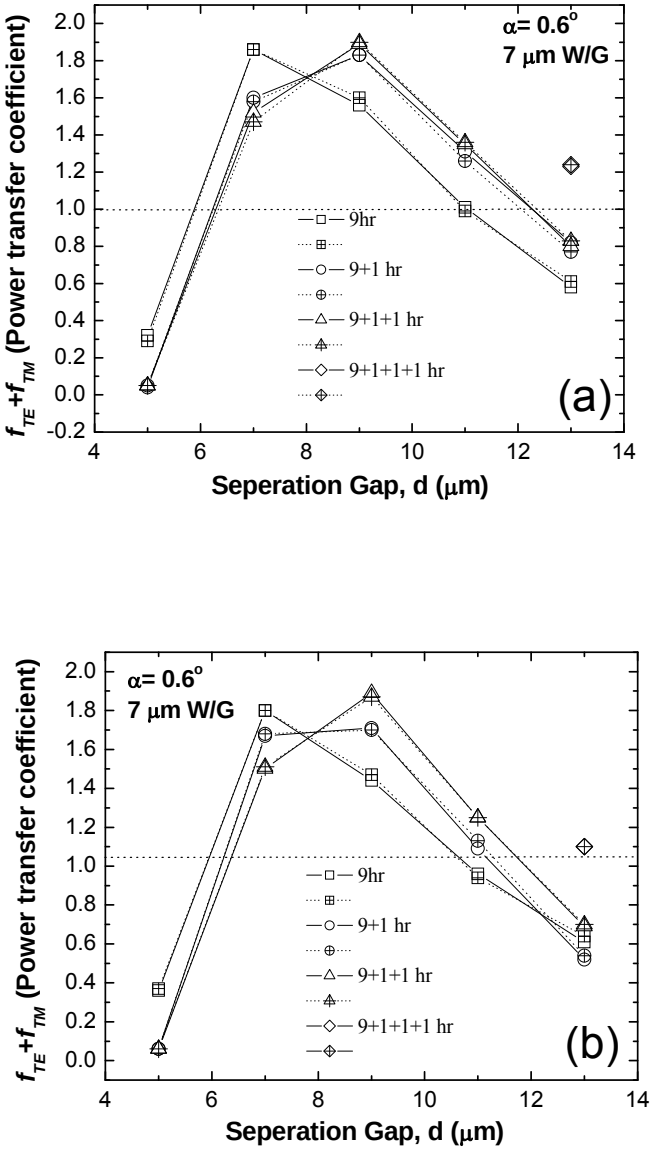

Fig. 27. Dependence of the sum of the power splitting ratio for the TE input polarization plus the TM input polarization on the separation gap d and diffusion time for polarization beam splitters on: (a) SN#1 and (b) SN#2. Dashed lines with cross in symbols identify input at port2. Solid lines without cross in symbols identify input at port1.

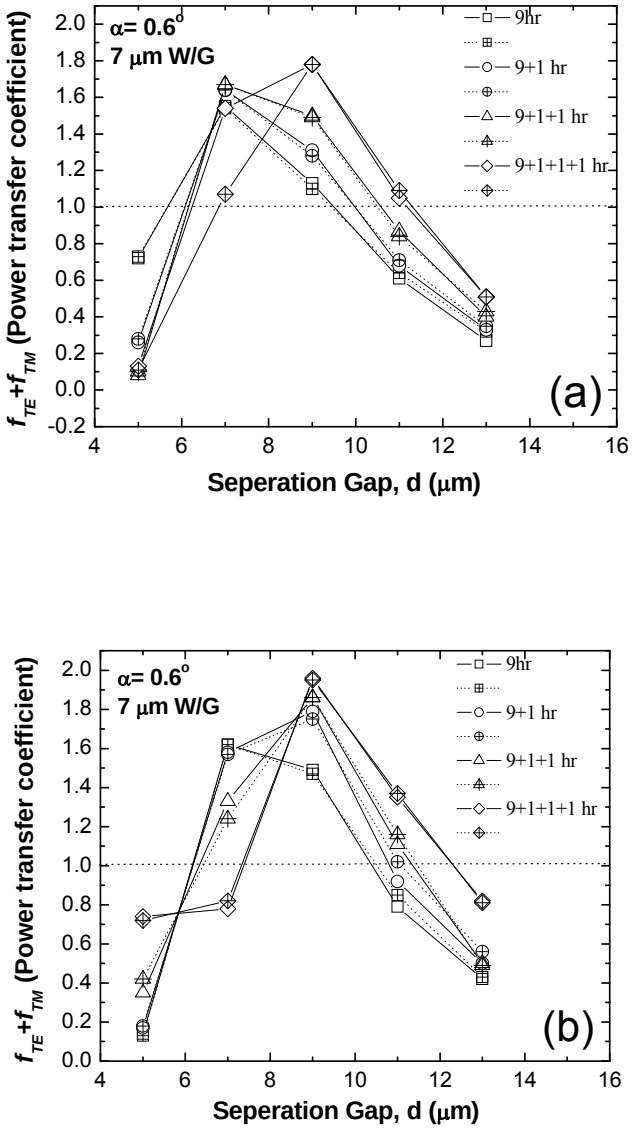

Fig. 28. Dependence of the sum of the power splitting ratio for the TE input polarization plus the TM input polarization on the separation gap d and diffusion time for polarization beam splitters on: (a) SN#3 and (b) SN#4. Dashed lines with cross in symbols identify input at port2. Solid lines without cross in symbols identify input at port1.

B. Zn Vapor Diffused Channel Waveguides and Beam Splitters in $LiTaO_3$*

Optical characterization of $LiTaO_3$ samples was carried out with the same setup as the measurement of $LiNbO_3$ (shown in Figs. 22, 23 and 26). All the channel waveguides were observed to be single mode for both the TE (extraordinary) and TM (ordinary) polarizations. Splitters which were produced with 7μm wide channel waveguides better fulfilled the relaxed beam splitter (RBS) criterion expressed in equation (91), over those produced using the 8μm wide waveguides. Only the results obtained from devices with W = 7μm are presented. Table 5 summarizes the measured values of Full Width at Half-Maximum (FWHM) for horizontally scanned mode profiles on straight channel waveguides formed in each of the three samples.

Table 5. FWHM for horizontal scans on 7μm wide straight channel waveguides (diffusion conditions of the samples are listed in Table 2).

Sample	TE-polarization (μm)	TM-polarization (μm)
S3	12.7	12.7
S7	11.9	12.4
S8	11.6	14.1

*Reprinted with permission from "Polarization dependence of the coupling ratio in $LiTaO_3$ directional couplers" by Y. W. Shin, O. Eknoyan, and H. F. Taylor, 2005, *Applied Optics*, vol. 44, no. 7, pp. 1156-1159, Copyright (2005) by OSA.

For vertical scans, the FWHMs were somewhat asymmetric, as expected, because of the large index difference between the air (above the sample) and the substrate. In view of the fact that the waveguides in the coupling region were displaced laterally, the horizontal mode profiles were more relevant for inter-waveguide coupling considerations.

Fiber-to-fiber insertion loss values, measured by butt coupling with single mode fibers to the input and output of the 7μm wide straight channel waveguides in each of the three samples, are listed in Table 6 for both the TE and TM polarizations.

Table 6. Fiber to fiber insertion loss for 7μm wide straight channel waveguides (diffusion conditions of the samples are listed in Table 2)

Sample	Insertion loss (dB) TE-polarization	Insertion loss (dB) TM-polarization
S3	3.30	3.44
S7	3.62	3.24
S8	3.59	3.81

Table 7 compares the transmission loss values for the various directional couplers produced by sample S7 with bending angle $\alpha = 0.6^{o}$ to those produced with $\alpha = 1.0^{o}$. The values were determined by measuring output powers (P_1 and P_2) from the two arms of each directional coupler, as in the case of the $LiNbO_3$ samples. All the listed measurements are for 7μm wide channel waveguides. The results indicate a higher loss for devices with the larger bending angle, in agreement with theory. The losses for $\alpha =$

1.0^o are larger by 1.71dB or more for the TE input polarization and by 6.61dB or more for the TM input polarization than for $\alpha = 0.6^o$.

Table 7. Variation of transmission loss with bending angle for directional couplers of various Separation gap *d* values using 7μm wide waveguide channels in sample S7.

Separation Gap *d* (μm)	5	7	9	11	13
TE input $\alpha = 0.6^o$	2.44	3.73	1.80	2.41	2.31
TE input $\alpha = 1.0^o$	4.10	16.31	13.23	8.62	4.65
TM input $\alpha = 0.6^o$	2.56	3.25	3.75	3.08	3.38
TM input $\alpha = 1.0^o$	13.57	13.11	12.08	11.42	9.99

The variations in the sum of the power splitting ratios for the orthogonal TE and TM polarizations, $f_{TE} + f_{TM}$, as a function of the separation gap *d* are shown in Fig. 29 for splitters in each of the three samples (S1, S2, S3) with a bending angle of $\alpha = 0.6^o$, and in Fig. 30 for splitters with a bending angle of $\alpha = 1.0^o$. Realization of the required criterion expressed by equation (90) at two values of the separation gap (d = 5 and 13μm in Fig. 29) with the same bending angle in sample S7 is reasonable because coupling between the two parallel waveguides is a periodic function of separation. Also, the two bending angles in sample S3 (d = 11 μm with $\alpha = 0.6^o$ in Fig. 29, and d = 13 μm with $\alpha = 1.0^o$ in Fig. 30) are indicative of a power transfer occurring between neighboring waveguides through the bent arms at the input and output ends of the interaction regions.

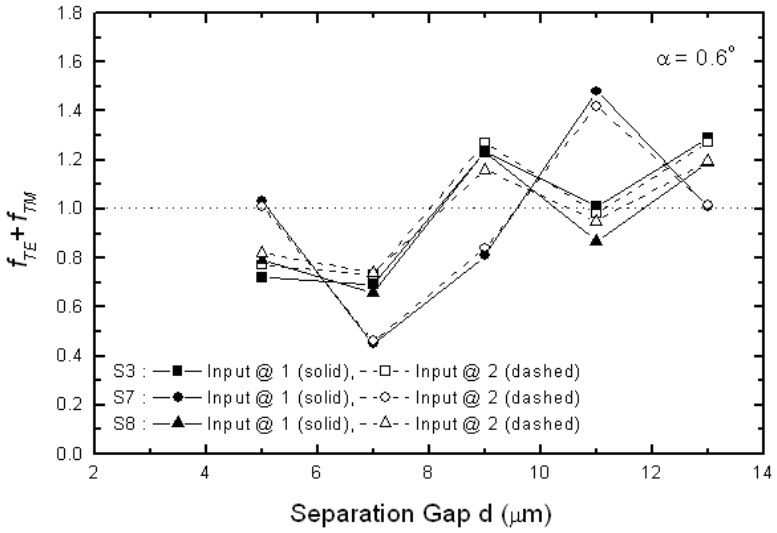

Fig. 29. Dependence of the sum of the power splitting ratio for the TE input polarization plus the TM input polarization on the separation gap *d* for the polarization beam splitters produced with 7μm-wide waveguides and a bending angle of 0.6^{o} [35], from 6 hours Zn vapor diffusion in $LiTaO_3$.

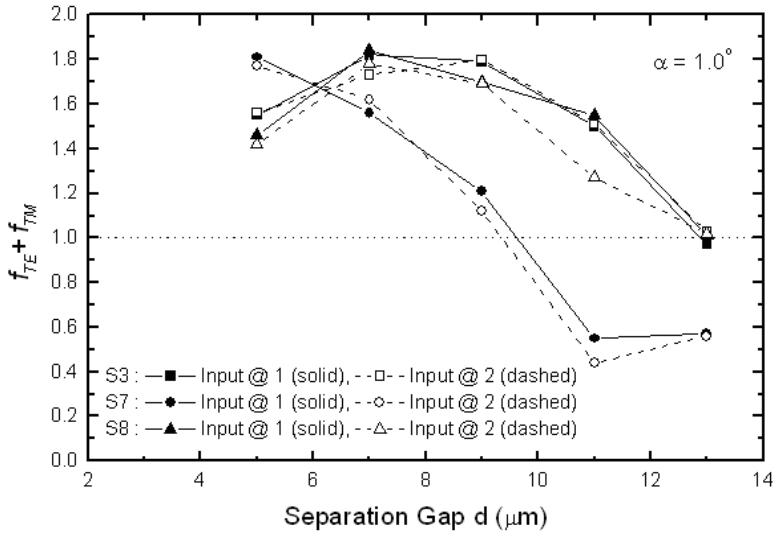

Fig. 30. Dependence of the sum of the power splitting ratio for the TE input polarization plus the TM polarization on the separation gap d for polarization beam splitters produced with 7-μm-wide waveguides and a bending angle of 1.0^{o} [35], from 6 hours Zn vapor diffusion.

C. Tunable TE↔TM Polarization Mode Converters

The tunable TE↔TM polarization mode converter is a crucial element for an optical tunable filter. In this work, it is formed by placing one pair of electrodes and a phase-matched periodic strain-induced index grating on top of a single-mode Ti-indiffused channel waveguide. The test setup used to characterize the performance of a tunable TE↔TM polarization mode converter, is illustrated in Fig. 31

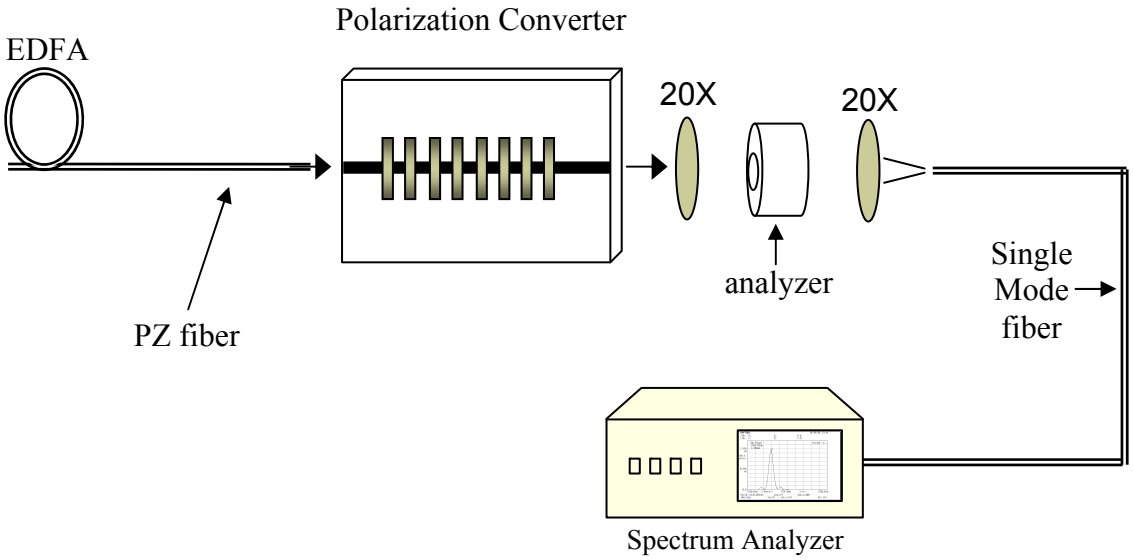

Fig. 31. The test setup for a polarization mode converter.

A broadband source is required to characterize wavelength selectivity. The Amplified Spontaneous Emission (ASE) light from an Erbium-Doped Fiber (EDF) in the 1.55μm wavelength regime was used as a broadband light source. The broadband ASE source was assembled with a backward pumping configuration, as shown in Fig. 32.

A 5m long Erbium-Doped Fiber (EDF) was pumped by a 980nm Laser Diode (LD) (SDL Optics Inc. Model: SDLO-2400-090) through a 980/1550nm WDM coupler. An optical isolator (Kaifa Technology, Model: IS-A-55-B-A-11) with more than 38dB of isolation was connected at the output of the coupler to prevent self-oscillation (lasing). The broadband ASE light was launched into one flat-polished end-edge of a channel waveguide through a cleaved single mode polarizing fiber (PZ fiber) which could be rotated to choose either a TE or TM polarization.

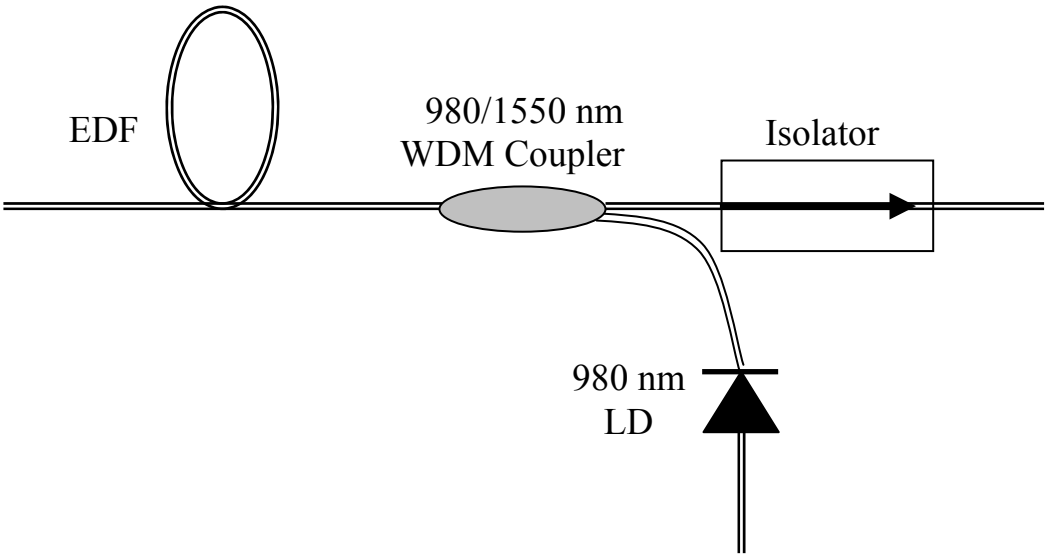

Fig. 32. Broadband ASE source assembly configuration.

A high polarization extinction ratio > 35dB was achieved for both the TE and TM polarized inputs. After PZ fiber rotation for polarization selection, at least 30 minutes was allowed for stabilization. To control the substrate temperature for the thermal tuning, the sample was placed on a Cu plate on top of a Thermo-Electric Cooler (TEC) which

was mounted on a high resolution x-y-z translation stage (LineTool Co., Model: A-RHFF). A thermistor (Omega Model: 44030) that was placed on the Cu plate was used to measure the substrate temperature. The output light beam was collimated with a 20X objective lens and passed through a polarization analyzer that could be rotated to pass either the TE or TM polarization of the output (Fig.31). The light beam from the polarization analyzer was focused by the second 20X objective lens and coupled into a cleaved single mode fiber, which in turn was connected to an Optical Spectrum Analyzer (OSA) (Anritsu, Model MS9710C). The output ASE power as a function of the LD pump current is shown in Fig. 33. An ASE power of 1mw was obtained at a pump current of 75mA. A typical output spectrum of the ASE source is shown in Fig. 34.

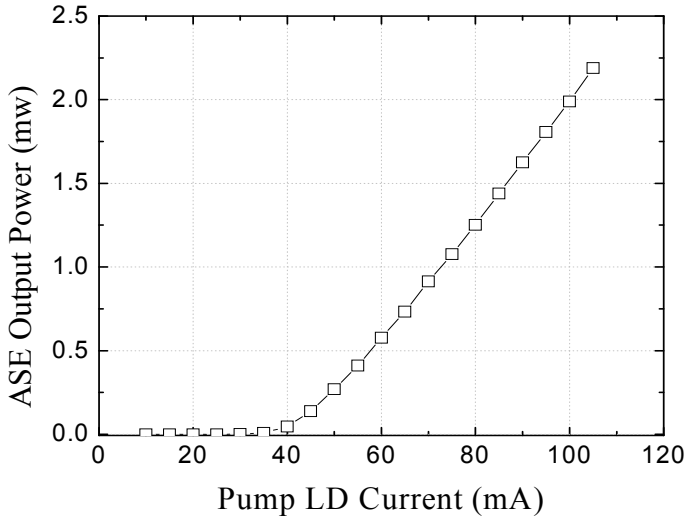

Fig. 33. ASE output power variation with the pump LD current.

According to the spectrum, the output power varies with wavelength, with a maximum power near 1531nm.

To test the polarization mode converter, the polarization of the input light has to be set to either the TE or the TM polarization. According to the analysis of the shear strain distribution in the $LiNbO_3$ substrate with the strain-induced SiO_2 gratings, the thickness of the SiO_2 and the elevated temperature during the deposition process are primary factors in the performance of polarization conversion.

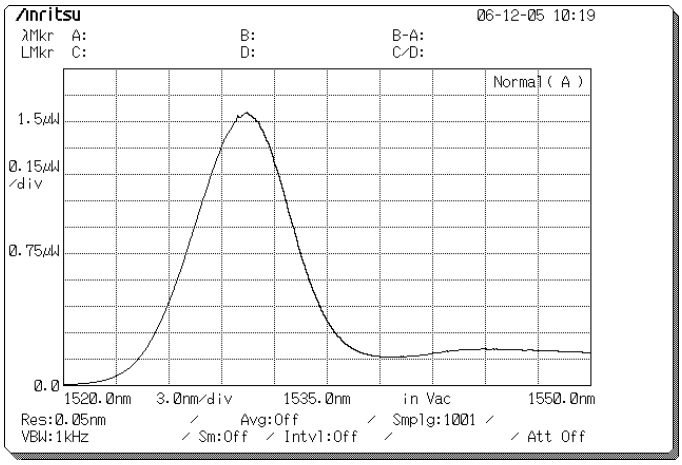

Fig. 34. ASE output spectrum at the pump LD current of 75mA.

To optimize the condition for the polarization conversion, various converters of different thicknesses of SiO_2 that were deposited at the same elevated 385^{o}C temperature were characterized. It was found that a converter with a SiO_2 film thickness of 1.60μm deposited at 385°C provided the best conversion efficiency, at 99.8%. The output spectra of a mode converter with a total of 500 strain-induced index gratings and a 21μm spatial period on sample SRD#5 are shown in Fig. 35 for both TE- and TM-polarized

inputs. The 7μm-wide channel waveguide of sample SRD#5 was produced from a 1210Å thick Ti film diffused at 1035°C for 10 hours, which are the optimized parameters that satisfy the requirements of the relaxed beam splitter. Fig. 35(a) and (b) show the unconverted TM mode output spectrum with both a linear and log scaled plot, respectively. The converted output spectra are shown in Fig. 35(c) and (d). Both reveal very comparable converted profiles at the phase-matched wavelength of 1534.8nm with a -3dB bandwidth (FWHM) of 2.3nm. The -3dB bandwidth is in close agreement with the expected value from $\Delta\lambda = 0.8(\lambda_o / N)$ with $\lambda_o = 1535$nm and $N = 500$. A similar spectrum was also observed for the orthogonal polarized input TE.

By calculating conversion efficiency, as defined in equations (101) and (102), the performance of the polarization mode converter can be verified and evaluated. The ideal conversion efficiency is equal to one (100%) at the phase-matched wavelength. Fig. 36 shows the experimental conversion efficiency as a function of the wavelength for both the TE- and the TM-polarized inputs with a 500-grating mode converter on sample SRD#5 at room temperature. It reveals 99.8% conversion efficiency at the phase-matched wavelength of 1534.8nm, it is polarization-independent and corresponds to a birefringence value Δn of 0.0731.

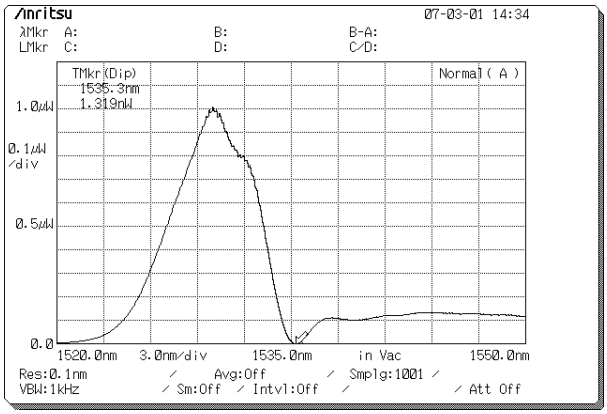

(a) Unconverted TM mode linear output

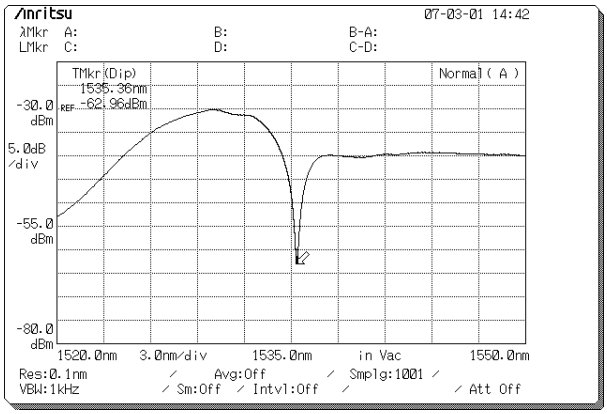

(b) Unconverted TM log output

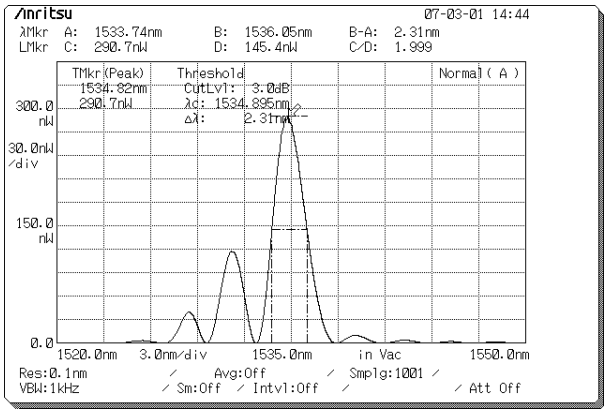

(c) Converted TE mode linear output

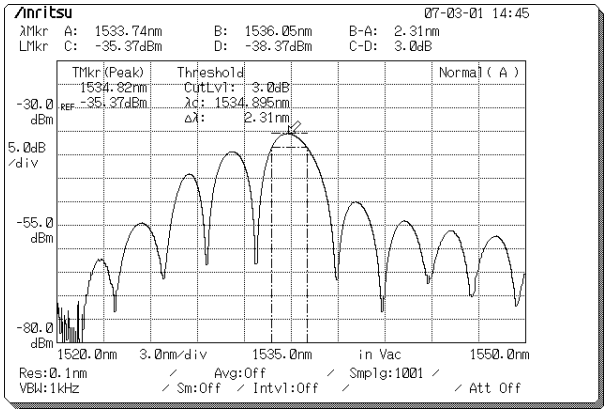

(d) Converted TE log output

Fig. 35. Output spectra of a polarization mode converter(SRD#5) for a TM polarized input at room temperature.

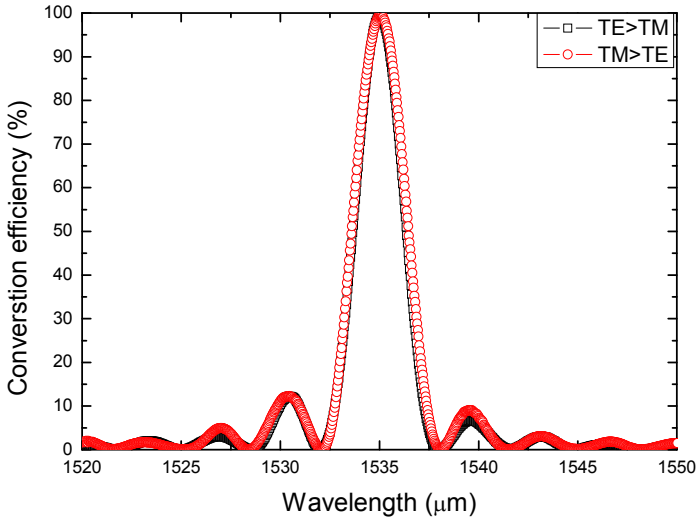

Fig. 36. Conversion efficiency as a function of wavelength tested on sample SRD#5 with 1.6μm thick SiO_2 gratings deposited at 385°C for both the TE- and TM-polarized inputs.

The variation of birefringence in $LiNbO_3$ with temperature ($d(n_e-n_o)/dT \sim -3.45 \times 10^{-5}$ /°C at wavelength 1.55μm) [36], provide a means for tuning the phase-matched wavelength by changing the substrate temperature via a thermoelectric cooler. With thermal tuning, the phase-matched wavelength shifted from 1530.43nm at 27.5°C to 1548.84nm at 14.8°C on sample SN#6 which had waveguides formed from a 1214Å thick Ti and diffused at 1035°C for 11 hours, as plotted in Fig. 37. The strain induced grating on sample SN#6 were formed by depositing 1.6μm thick SiO_2 film at 385ºC. This indicates a thermal tuning rate of -1.45 nm/°C.

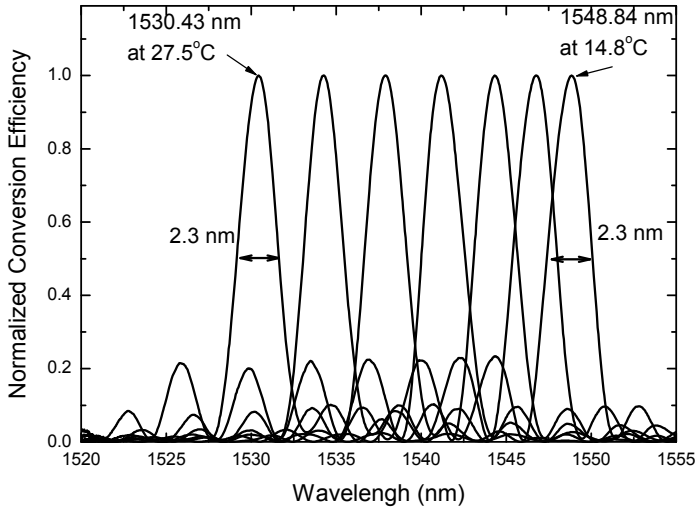

Fig. 37. Normalized converted power as a function of wavelength for both TE- and TM polarized inputs tested on sample SN#6 with thermal tuning.

Electro-optic tuning provides another tuning mechanism of a polarization mode converter via the electro-optic effect through an applied voltage. The electrical tuning spectral characteristics for a converter on sample SN#6 containing Cr/Au/Ti electrodes with electrode separation gap of 17μm are shown in Fig. 38(a). The tested converter (SN#6) for this measurement had a 7μm wide channel waveguide that was produced by diffusion a 1214Å Ti film in wet ambience at 1035°C for 11 hours with 500 of SiO_2 strain inducing gratings. The phase-matched wavelength of the response spectra shifted by 14.4nm with a DC voltage tuning from -100 V to +100 V, corresponding to a tuning rate of 0.07nm/V for TM input, and 0.05 for TE input. The phase matched wavelength for this converter on sample SN#6 was at 1535nm. The tuning of the conversion peak

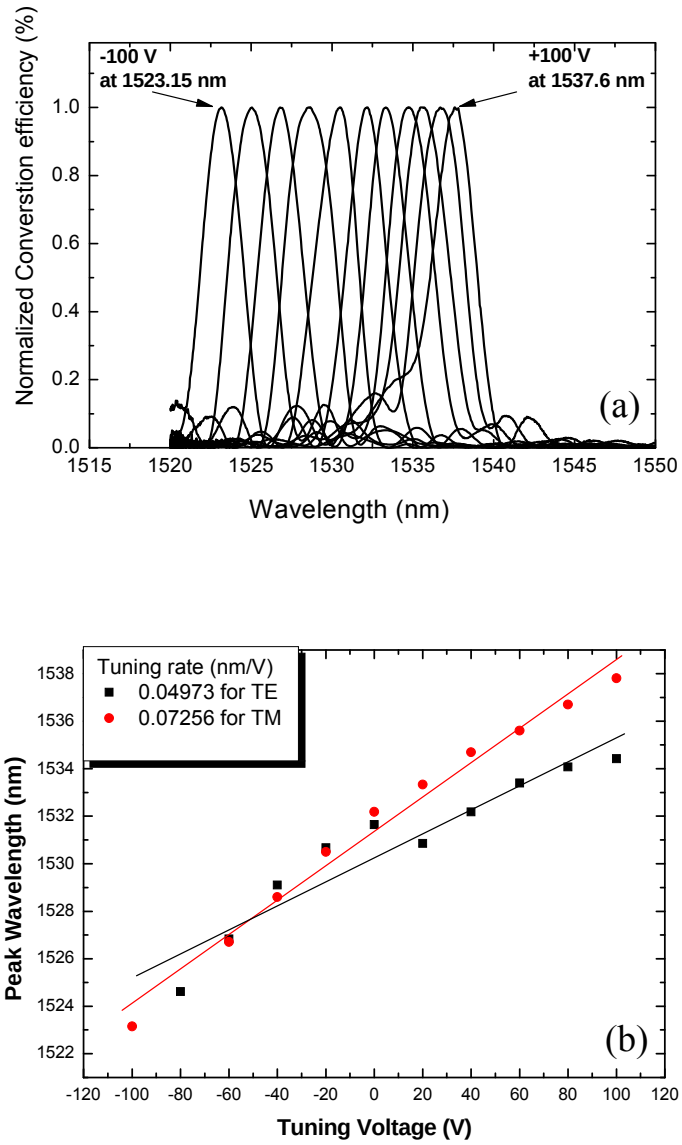

Fig. 38. Electro-optic tuning of the center wavelength for both TE- and TM-polarized inputs with an electrode gap of 17μm tested on sample SN#6 at 23°C. (a) The polarization independent conversion efficiency as a function of the wavelength for TM polarizations with voltage as a parameter, (b)linearly tuning behavior of phase-matched wavelength with applied voltage.

wavelength with voltage is linear for either TE or TM input polarization, as shown in Fig. 38(b), however the obtained tuning rates are notably different. Assuming that the overlap factors between the applied electric field and the optical field for the TE and TM polarizations are equal, $\Gamma_{TE} = \Gamma_{TM}$, the overlap factor is calculated from equation (105) as 0.52, for the electrode gap of 17μm.

D. Electro-optically Tunable Add Drop Filters with Relaxed Beam Splitter

The optically tunable add/drop filter in this research is composed of two relaxed beam splitters and tunable TE↔TM polarization mode converters that are integrated in an asymmetric Mach-Zehnder interferometer waveguide configuration. The performance of the filter depends largely on fullfilling the requirement of the power transfer coefficient of the relaxed beam splitters, as well as the realization of a high conversion efficiency with a narrow -3dB bandwidth (FWHM) and low side bands for the polarization mode converters. It is not possible to characterize the power transfer coefficient of the combined beam splitters in series for both the TE and TM polarizations in the adopted interferometer configuration. Therefore, the same fabrication parameters (Ti thickness, diffusion temperature and time) and separation d between waveguides of the directional type splitters, which were optimized for satisfying the requirement that the sum of the power transfer coefficients from both input polarizations must equal one at the output of a single beam splitter, were adopted for producing the interferometer waveguide configuration which integrates two such splitters in series on a $LiNbO_3$ substrate as shown in Fig. 39.

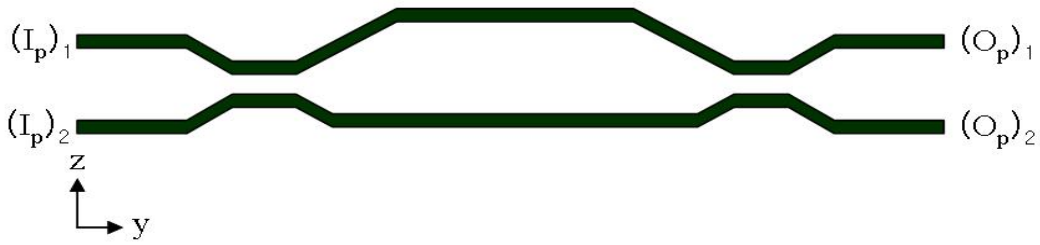

Fig. 39. Schematic of the 1st layer for the optical waveguide add drop filter.

After completing the Ti-indiffusion of the interferometer waveguide pattern, both end-edges of the $LiNbO_3$ substrate were polished for fiber optical coupling. The output power from each output port was measured using the same test setup as that which was used for the single beam splitters characterization. Based on the discussion in Chapter III, all of the input power should ideally emerge out from the express port and the optical power of drop port should be zero in the absence of polarization mode converters. Table 8 shows the results of the output performance and insertion loss of straight channel waveguides (SCs) and asymmetric interferometers (MZIs) of sample SR#5, which were formed by diffusing 1219Å thick Ti strips at 1035°C for 10 hours, before forming electrodes and strain gratings. The listed results confirm that most of the input optical power in the tested interferometer structures are delivered to the express port. The insertion loss of straight channel waveguides are in the range of 2.64~4dB. As expected, the insertion loss of the interferometers is larger than the channel waveguide because of the additional bending loss in the two beam splitters. Fig. 40 shows the variations of the filter's overall extinction ratio for different input polarizations with additional diffusion

times. In that plot, MZI#1 and MZI#3 are for 11μm and 13μm waveguide separation gap in the beam splitters (see Appendix 14), respectively. For the cases that show better than -20dB extinction ratio, the effect of diffusion time on the overall extinction ratio appears

Table. 8. The output performance of straight channel waveguides and optical add drop filters in sample SR#5 without strain gratings and electrodes.

Name	Input port	TE (μw)		Insertion Loss (dB)	TM (μw)		Insertion Loss (dB)
		$(O_p)_1$	$(O_p)_2$		$(O_p)_1$	$(O_p)_2$	
SC-#1	Single input	446		2.67	452		2.64
MZI-#1	$(I_p)_1$	200	2	6.11	194	0.6	6.30
	$(I_p)_2$	3	215	5.78	0.8	201	6.14
SC-#2	Single input	405		3.09	412		3.04
MZI-#2	$(I_p)_1$	201	3	6.07	206	0.1	6.05
	$(I_p)_2$	3	213	5.82	0.4	199	6.19
MZI-#3	$(I_p)_1$	214	1.8	5.82	198	0.8	6.21
	$(I_p)_2$	1.6	200	6.12	0.7	213	5.89
SC-#3	Single input	320		4.11	404		3.13
MZI-#4	$(I_p)_1$	184	1.8	6.49	226	0.8	5.63
	$(I_p)_2$	1.6	185	6.69	0.7	217	5.81
SC-#4	Single input	437		2.76	414		3.02

* SC and MZI stand for the straight channel waveguide and Mach Zehnder Interferometer, respectively.(See Appendices 14 and 15 for more details)

to be small, over the tested range (9~11 hours).

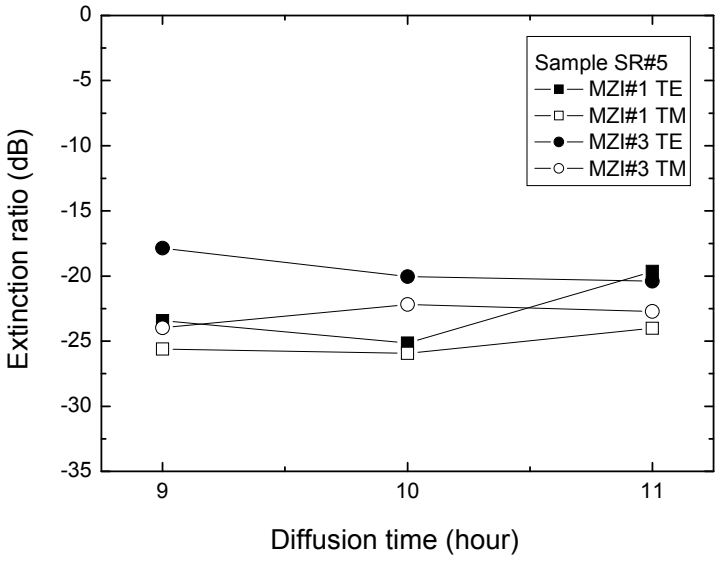

Fig. 40. The performance of the overall extinction ratio on a 2×2 interferometer structure in sample SR#5 produced by 1219Å thick, 7μm wide Ti film strip for 10 hours of diffusion at 1035ºC. Electrodes and grating are not present on the surface.

1. Spectral characteristics without applying voltage

After the performance of the Mach Zehnder interferometers was characterized by measuring the output powers from the express and drop ports, electrode pads made with Cr/Au/Ti of thicknesses, 400Å/800Å /600Å, respectively, were produced on the surface along the sides of the polarization mode converter regions with a 17μm gap between the electrodes. Finally 500 periodic strain-induced index gratings were formed on top of the

electrode pads from a SiO_2 film deposited at 390ºC and patterned after cooling to room temperature for the TE↔TM mode conversion. The alignment of the electrodes layer is critical because there could be significant optical loss for TM polarization if the electrodes touch the waveguide.

Table 9. Fiber to fiber insertion loss of the filter (SR#5) after forming gratings and electrodes.

Device SR#5	Input	TE input(μW)		Insertion Loss (dB)	TM input(μW)		Insertion Loss (dB)
		$(O_P)_1$	$(O_P)_2$		$(O_P)_1$	$(O_P)_2$	
MZI#1	P1	164	21	6.49	161	20	6.61
	P2	23	167	6.38	21	165	6.50

Once the entire device structure was formed and critical dimensions confirmed, optical measurements were repeated using the same setup as for the beam splitter (Fig.26) to ensure no damage occurred to the waveguides from the subsequent processes. Finally, the spectral characteristics were investigated using the set up shown in Fig. 41. The measured fiber to fiber insertion loss of MZI#1 in sample SR#5 was 6.5dB for the TE input polarization and 6.6dB for the TM polarization, as indicated in Table 9. These losses could be reduced by decreasing the bending angle.

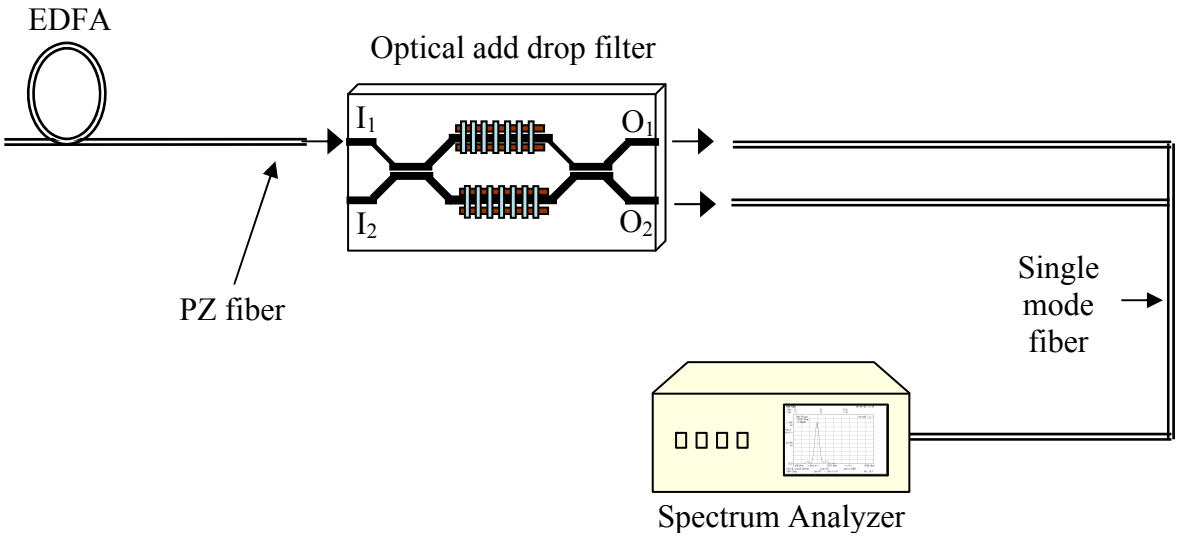

Fig. 41. The test setup for the optical add/drop filter.

Fig. 42 shows the output spectra of the express port O_1 and the drop port O_2 for filter MZI-#1, which is on sample SR#5 at 22°C substrate temperature without applying a DC voltage. The input beam enters from input port 1, $(I_p)_1$ and has a TM polarization. According to the spectrum image in Fig. 42(b), the peak wavelength of the drop port is at 1533.78nm with a -3 dB bandwidth (FWHM) of 2.31nm, which is in close agreement with the expected value from $\Delta\lambda = 0.8(\lambda_o/N)$ with λ_o = 1533.78nm and N = 500. The output spectra for TE polarized input is shown in Fig.43, and it matches closely to the TE input case.

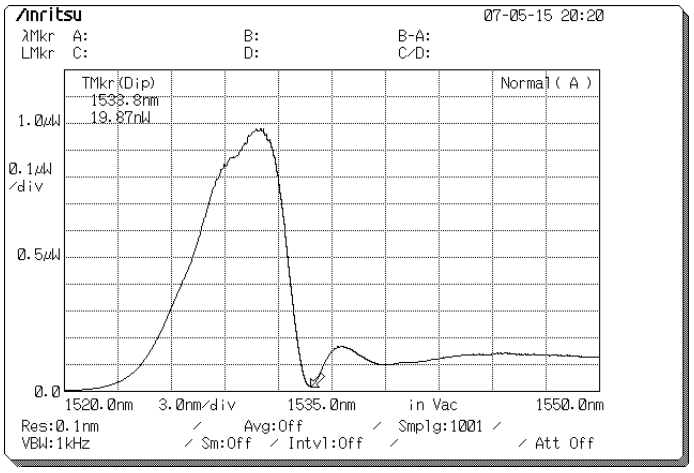

(a) Spectrum of express port $(O_p)_1$

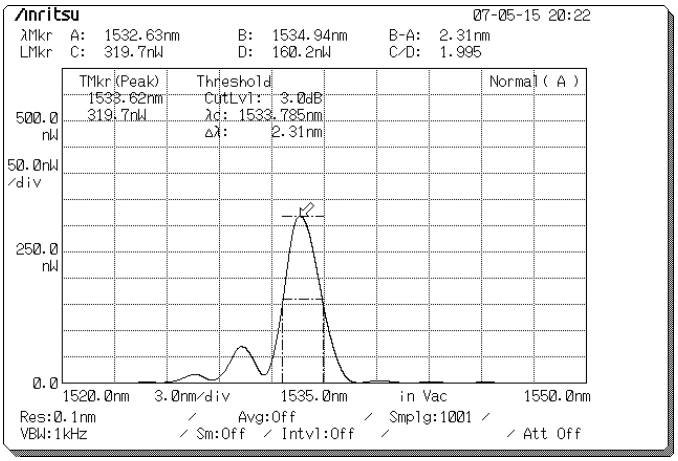

(b) Spectrum of drop port $(O_p)_2$

Fig. 42. Linear output spectra of the filter device MZI-#1 on sample SR#5 at 22ºC substrate temperature for the TM-polarized input from port $(I_p)_1$ without applying a DC voltage.

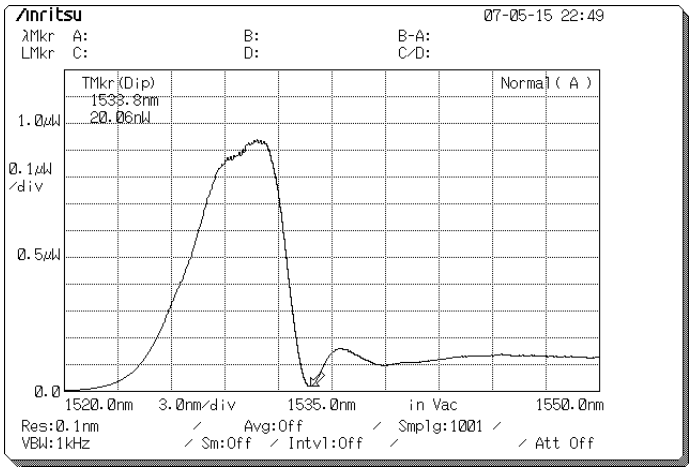

(a) Spectrum of express port $(O_p)_1$

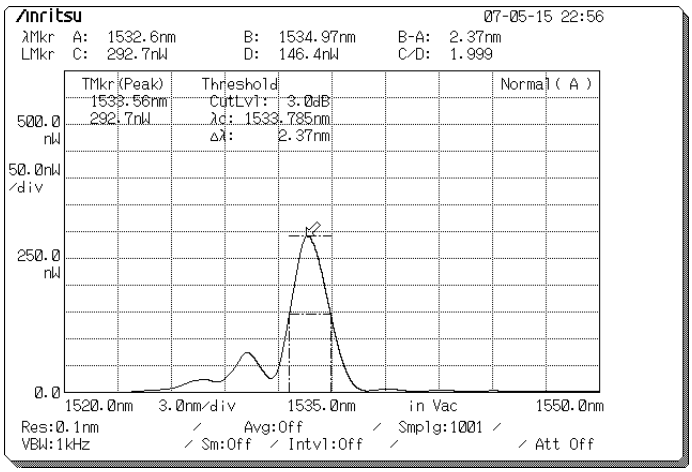

(b) Spectrum of drop port $(O_p)_2$

Fig. 43. Linear output spectra of the filter device MZI-#1 on sample SR#5 at 22ºC substrate temperature for the TE-polarized input from port $(I_p)_1$ without applying a DC voltage.

2. Normalized spectral characteristics without applying voltage

To evaluate the isolation and side-lobe characteristics of the filter, data obtained from the spectrum analyzer needed to be normalized relative to the original broadband input signal, because the output intensity of the ASE is not uniform over its spectral range. This was accomplished by using

$$\text{Relative Power (dB)} = 10 \times \log\left[\frac{\left(\frac{P_{f,out}(\lambda)}{P_{stch}(\lambda)}\right)}{\left(\frac{P_{f,out,max}(\lambda_s)}{P_{stch,}(\lambda_s)}\right)}\right]. \quad (128)$$

In the above relation, $P_{f,out}(\lambda)$ is the filter output power, $P_{stch}(\lambda)$ is the output power from a straight channel waveguide $P_{stch}(\lambda)$ on the same sample and for the same-drive current, $P_{f,out,max}(\lambda_s)$ is the filter maximum output power at the phase match wavelength λ_s, and $P_{stch}(\lambda_s)$ is output power of the straight channel waveguide, also at λ_s.

Fig. 44 is the normalized output spectra of the relative power for the filter MZI-#1 on sample SR#5 at 22ºC substrate temperature for TE and TM polarized inputs from port $(I_p)_1$ without applying a DC voltage. The center wavelength, which is the phase-matched condition, is 1533.8 and 1533.85nm for the TE and TM, respectively. The isolation of the express channel is 13.1dB for the TE and 13.45dB for the TM polarizations. The nearest side lobes to the main peak are about 10dB for the TE and 10.5dB for TM polarization below the central lobe.

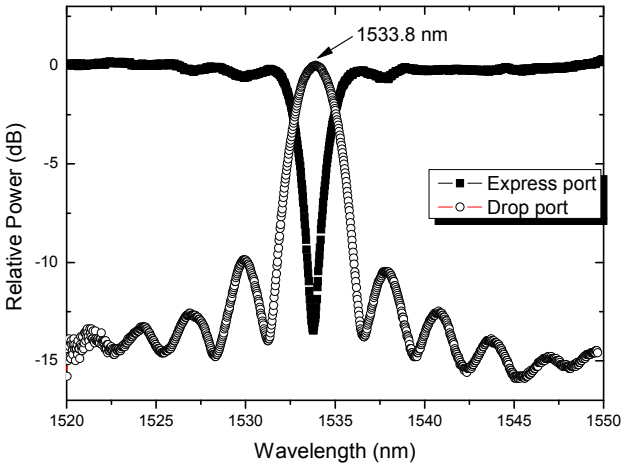

(a) Output spectrum for the TE input polarization

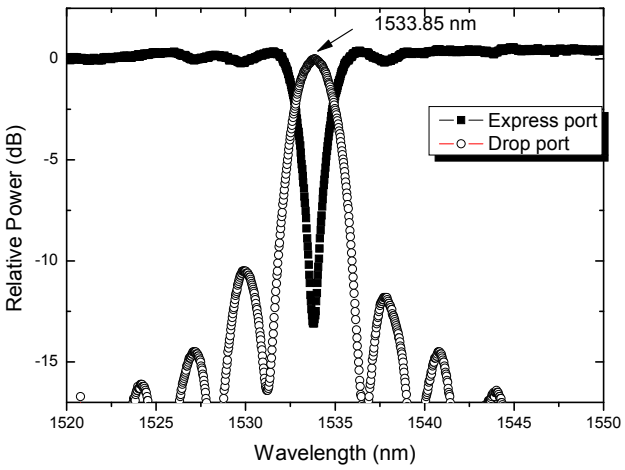

(b) Output spectrum for the TM input polarization

Fig. 44. The normalized filter output spectrum for device MZI-#1 in sample SR#5 without an applied voltage at room temperature for the drop port (open circle) and express port (solid square).

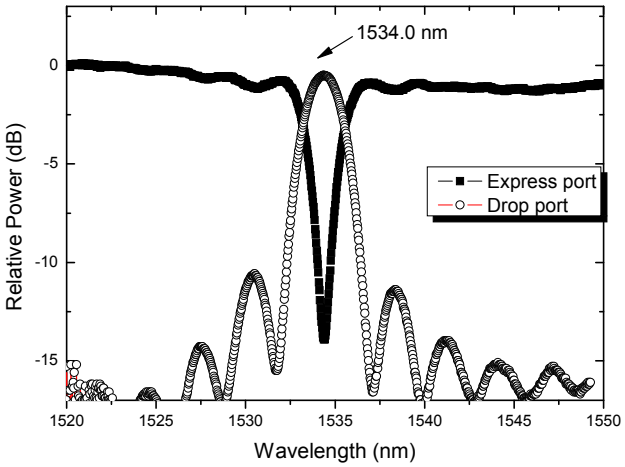

(a) Output spectrum for the TE input polarization

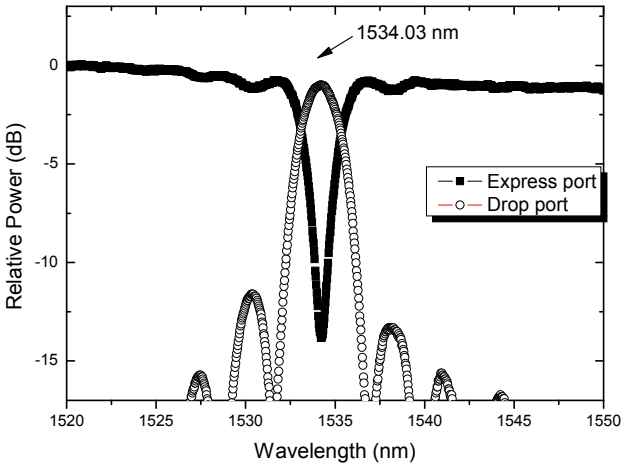

(b) Output spectrum for the TM input polarization

Fig. 45. The normalized filter output spectrum with the input light from port $(I_p)_2$ for device MZI-#1 in sample SR#5 without an applied voltage at room temperature for the drop port (open circle) and express port (solid square).

The output spectrum for TM input polarization is slightly better compared to TE input and is likely because of the higher extinction ratio of the interferometer, as evident from Fig. 40. The side lobes can be further suppressed by apodization of the polarization-converting strain pads [37].

Another important feature for the add/drop filter is the add port transmission performance. When the input signal is launched at the lower input port $(I_p)_2$, the output spectra in this case becomes $(O_p)_2$ for the express port, and $(O_p)_1$ for the drop port. The results are shown in Fig. 45 without any applied voltage and at room temperature. The output spectra for drop (Fig. 44) and add (Fig. 45) are well matched. The center wavelength shift is less than 0.2nm, and may be due to an experimental error.

Polarization independence is also an important requirement for an optical add/ drop filter. This can be evaluated by comparing the output spectra for each of the polarized input cases, as in Fig. 44(a) and (b) or Fig. 45(a) and (b). From these two graphs, it can be seen that the central wavelength shift caused by polarization is less than 0.05nm. However, the overall shape of the graphs such as sidelobes and isolation are almost identical. Consequently, these aspects represent the fact that the performance of the proposed filter in this research is polarization independent.

Previous results show polarization independent operation of the filter. To confirm this feature, the device was tested with 45º polarized input. As shown in Fig. 46, the output spectra from the express and drop ports for an input polarized at 45º, are similar to those obtained from either a TE or a TM input polarization. This validates polarization independent operation.

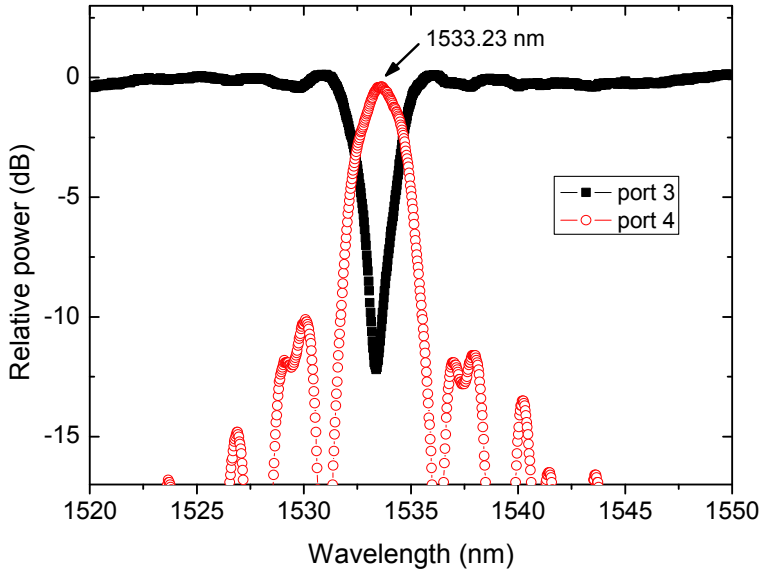

Fig. 46. The output spectrum of the filter(MZI#1 in sample SR#5) with 45º input.

3. Electro-optic tuning

The electro-optic tuning performance was characterized by applying DC voltage to the electrode on the filter, as shown in Fig. 47. In Fig. 48, the spectral response for the drop port is shown at applied voltages of -100V and +100V. The peak wavelength at the drop channel shifted by 15.7nm for the TE polarization and 15.4nm for the TM polarization. Throughout the tuning over the range from -100V to +100V, the observed Full Width at Half Maximum (FWHM) remained around 2.3nm. This agrees with the value calculated from equation (100), and could be made narrower by increasing the number of the strain-inducing grating pads, or in other words, the length of the polarization conversion region.

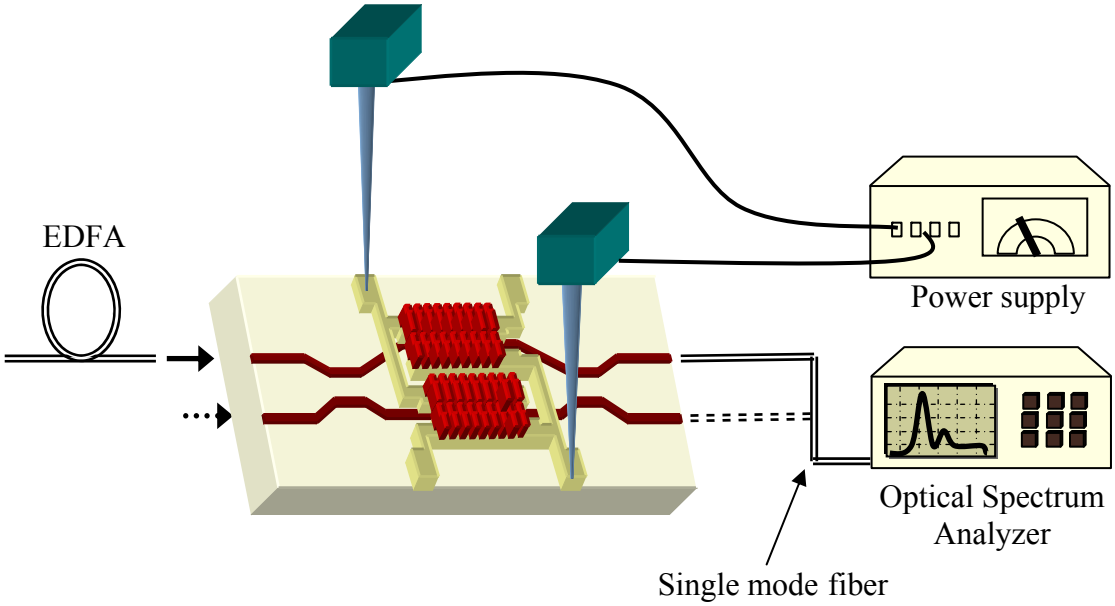

Fig. 47. Test set up for the electro-optic tuning.

The tuning range is mainly limited by the electric field breakdown of the $LiNbO_3$ crystal (nearly 10 V/μm) [17], and also depends upon the gap insulation between electrode pads and the quality of the electrode's metal deposition. In this research, the gap between the electrode pads was fixed at 17μm. The phase-matched wavelength shifted linearly with the tuning voltage. The observed tuning rates were 0.0754 nm/V for the TE-polarized input and 0.0751 nm/V for the TM-polarized input, as shown in Fig. 49. This tuning rate is slightly higher than what was found in previous results [12]. Higher tuning rates can be realized if narrower electrode gap is used. No major degradation was observed at the highest tuning voltage.

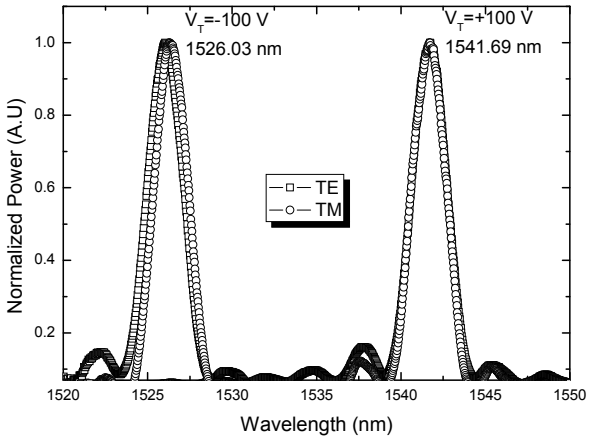

*

Fig. 48. Normalized electro-optic tuning performance of filter device MZI-1 on sample SR#5 for both TE and TM polarizations by applying a DC voltage from -100V to +100V.

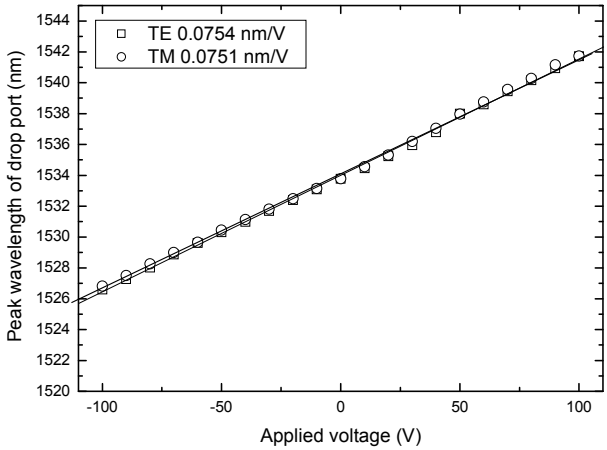

Fig. 49. Electro-optic tuning performance of filter device MZI-1 on sample SR#5 at 22°C for both the TE- and TM-polarized input.*

* Reprinted with permission from "Rapidly tunable optical add drop multiplexer utilizing relaxed beam splitters" by Y. W. Shin, O. Eknoyan, C. K. Madsen and H. F. Taylor, 2007, *Electronics Letter*, vol. 43, no. 25, pp. 1428, Copyright (2007) by The IET.

4. Tuning speed of the filter

The main advantage of electro-optic tuning is its rapid response time. Fast tuning speed is one of the most important requirements for an optical tunable filter in fast packet switched networks. The temporal tuning response is limited primarily by the electrode design and the speed of the electronics in the power supplies that are used to apply the tuning voltage. Two different time response tests were performed, as shown in Fig. 50. A voltage step from a signal generator (Agilent, model 33250B-signal generator) of 20V and rise time of approximately 5ns was used. In Fig. 50, the upper traces marked 1 represent the applied electrical signal from the generator to the electrodes, and the lower traces marked 2 represent the optical response from the drop port. To obtain an output response, the center wavelength of the drop port was shifted into the steep slope region (~ 1532.5nm) of the spectral output of the ASE using thermal tuning. The 10%-90% rise time is 22.4ns from a 5.2ns of input signal fall time. The 90%-10% fall time was 45.6ns from a 5.6ns of input signal rise time. Calculated tuning speeds of the filter based on rise and fall time are 0.664Å/ns and 0.329Å/ns, respectively. The slower fall time is attributed to the presence of charge in the oxide.

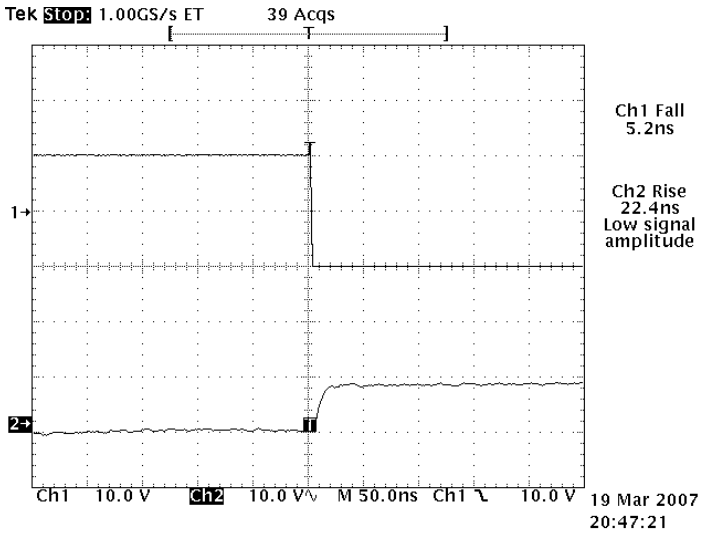

(a)

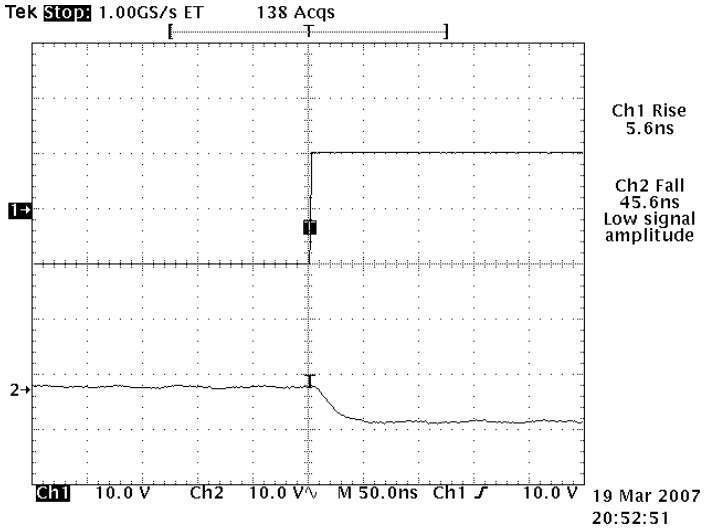

(b)

Fig. 50. The results of the temporal time response test of the filter with a 20 V step change in tuning voltage. Trace 1 is the applied voltage from the signal generator on the electrodes, and trace 2 is the optical output response at the drop channel; (a) rise time, (b) fall time.

E. Suggestion for Future Work

The nearest sidelobes to the main peak attained in this research are about 10dB below the central lobe. Lower sidelobes are essential for the suppression of interchannel crosstalk. Previous research in this laboratory has demonstrated electro-optically tunable programmable bandpass filter with nearest sidelobes of -20dB, utilizing symmetric branch 3-dB beam splitters [38]. The design used two-port asymmetric interferometer with interdigital electrode sets on its arms that allow the control of polarization coupling coefficient on individual sets electronically for the simultaneous tuning and apodization of the spectral output. This concept provides an attractive extension for making four-port add drop programmable tunable filters with low sidelobes. Fig. 51 shows a schematic for the proposed filter design which is composed of an asymmetric Mach-Zehnder interferometer containing two directional coupler type relaxed beam splitters, and interdigital electrode sets on the arms to provide programmable electro-optic coupling for polarization mode conversion. Programmability can be obtained by applying spatially periodic weighted independent voltages to the interdigital electrodes, which can be electronically controlled via a computer through a digital to analog converter (DAC) array chip. Using this method, lower tuning voltages and sidelobes suppression can be anticipated.

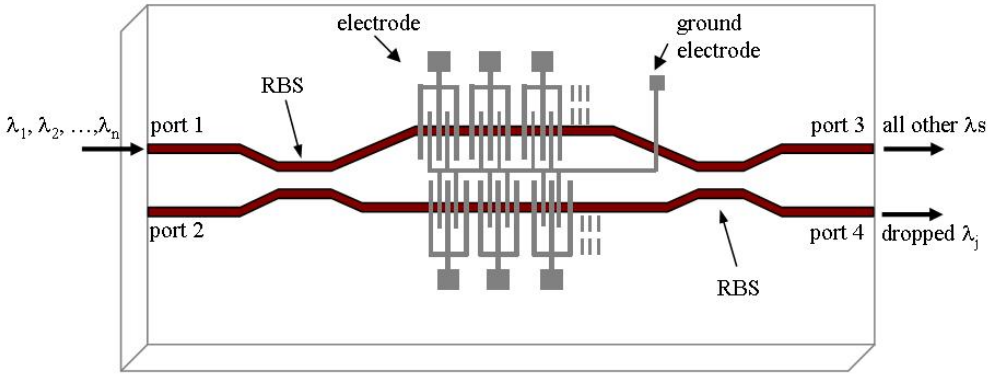

Fig. 51. A schematic for the electro-optic tunable filter utilizing relaxed beam splitters, programmable electro-optic polarization mode converter based on four-port asymmetric Mach-Zehnder interferometer configuration.

CHAPTER VI

CONCLUSION

A novel polarization independent electro-optically tunable add/drop filter using relaxed beam splitters has been developed. The filter is produced on a $LiNbO_3$ substrate, has a narrow -3dB bandwidth (FWHM) of 2.3nm and operates in the 1.55μm wavelength regime, it tunes rapidly with voltage and is polarization independent. The performance of the filter is based on passive beam splitters that satisfy a relaxed beam splitter (RBS) criterion and strain-induced phase-matched polarization mode converters, which are integrated on an asymmetric Mach-Zehnder waveguide configuration. The principle and performance of the optically tunable add/drop filter and the key components that govern its operation have been presented.

Channel waveguides and directional coupler type beam splitters with a bending angle of 0.6°, 3.5mm interaction region length L_c, and a gap between waveguides in the interaction region ranging from 5μm to 13μm with a 2μm interval were produced on x-cut, y-propagating $LiNbO_3$ substrates with different fabrication parameters. The experimental results from these elements were used to identify fabrication conditions that would satisfy the RBS requirement that the sum of the power transfer coefficient for the TE and TM polarizations should be equal to unity. Ti in-diffusion was used for the fabrication. Two sets of fabrication conditions were identified for producing the required RBSs, and both were formed utilizing 7μm wide channel waveguide. One set was

fabricated from a Ti film thickness of 1202Å and diffused at 1035°C for 10 hours. Fiber-to-fiber insertion losses of these splitters were 2.57dB and 2.67dB for the TE- and TM-polarized inputs, respectively. The other set of RBSs was produced with a Ti thickness of 1202Å and diffusion at 1025°C for 12 hours. Under these fabrication conditions, the channel waveguide were single mode for both polarizations. The measured FWHMs of the mode near field profiles were 6.06μm in the horizontal scan and 7.18μm in the vertical scan for TE polarization, while those for the TM polarization were 8.3μm in both scanning directions.

Tunable polarization mode converters with uniform strain-induced index gratings were produced from a spatially periodic static-strain inducing SiO_2 surface film with a spatial period of 21μm. Using a 1.6μm thick SiO_2 film that was deposited at 385ºC and patterned at room temperature with a total of 500 strips for the grating, a conversion efficiency of 99.8% and a -3dB bandwidth of 2.3nm were obtained. This is in close agreement with the calculated value of 2.45nm at the phase-matched wavelength 1535nm. Thermal tuning was used to shift the peak wavelength, and a thermal tuning rate of -1.45nm/°C was measured. Electro-optic tuning was also demonstrated. A shift for the peak conversion wavelength of 14.4nm was realized over a tuning voltage ranging from -100V to +100V. For an electrode gap of 17μm, a tuning rate of 0.049nm/V for the TE and 0.072nm/V for the TM polarization were obtained

An electro-optic add/drop tunable filter with relaxed beam splitters was produced based on the optimized fabrication conditions listed above. The fiber-to-fiber insertion loss for the interferometer was about 6dB and 6.5dB before and after integrating the

electrodes and gratings on the surface for both polarizations. At room temperature, the filter central wavelength at the drop channel was at 1533.8nm and for the add channel at 1534nm, for both polarizations. The -3dB bandwidth for both add and drop channels was 2.3nm. The nearest sidelobes were about 10dB below the center peak. A maximum tuning range of 15.7nm was achieved with an electrode gap of 17μm by controlling the applied voltage from -100V to +100V. The phase-matched wavelength tunes linearly at a rate of 0.075nm/V for both polarizations, and was repeatable. The temporal response of the filter to a 20V step change was measured to be 22.4ns for the rise time and 45.6ns for the fall time.

REFERENCES

[1] Govind P. Agrawal, *Fiber Optic Communication Systems*, 2nd edition. New York: John Wiley&Sons, 1997.

[2] P.E. Green, Jr., *Fiber Optic Networks*. Englewood Cliffs, NJ: Prentice Hall, 1993.

[3] H. Ishio, J. Minowa, and K. Nosu, "Review and status of wavelength-division-multiplexing technology and its application," *Journal of Lightwave Technology*, vol. LT-2, no. 4, pp. 448-463, Aug. 1984.

[4] C. R. Giles and M. Spector, "The wavelength add/drop multiplexer for light-wave communication networks," *Bell Labs Technical Journal*, pp. 207-229, Jan-Mar. 1999.

[5] W. Warzanskyj, F. Heismann, and R. C. Alferness, "Polarization-independent electro-optically tunable narrow-band wavelength filter," *Applied Physics Letters*, Vol. 53, pp. 13-15, Jul. 1988.

[6] P. Tang, "Polarization independent electrooptically tunable add drop filter in Ti:$LiNbO_3$ at 1.55 μm wavelength regime," Ph.D. Dissertation, Texas A&M University, Department of Electrical Engineering, College Station, 2002.

[7] A. Iocco, H. G. Limberger, and R. P. Salathe, "Bragg grating fast tunable filter," *Electronics Letters*, vol. 33, no. 25, pp. 2147-2148, Dec. 1997.

[8] S. Suzuki, A. Himeno, and M. Ishii, "Integrated multichannel optical wavelength selective switches incorporating an arrayed-waveguide grating multiplexer and thermooptic switches," *Journal of Lightwave Technology*, vol. 16, no. 4, pp. 650-

[9] D. Sadot and E. Boimovich, "Tunable optical filters for dense WDM networks," *IEEE Commun. Mag.*, vol. 36, no. 12, pp. 50-55, Dec. 1998.

[10] J. M. H. Elmirghani and H. T. Mouftah, "Technologies and architectures for scalable dynamic dense WDM networks," *IEEE Commun. Mag.*, vol. 38, no. 2, 58-66, Feb. 2000.

[11] P. Tang, O. Eknoyan, and H. F. Taylor, "Rapidly tunable optical add-drop multiplexer (OADM) using a static-strain-induced grating in $LiNbO_3$," *Journal of Lightwave Technology*, vol. 21, no. 1, pp. 236-245, Jan. 2003.

[12] H. Kuo, "Investigation of an electrooptic tunable filter in litium niobate," Ph.D. Dissertation, Texas A&M University, Department of Electrical Engineering, College Station, 2006.

[13] H. F. Taylor and O. Eknoyan, "Guided wave acousto-optic and electro-optic tunable filter designs with relaxed beam-splitter requirements," *Applied Optics*, vol. 39, no. 1, pp. 124-128, Jan. 2000.

[14] A. Yariv, *Quantum Electronics*, 3rd edition. New York: John Wiley & Sons, 1989.

[15] H. Nishihara, M. Haruna, and T. Suhara, *Optical Integrated Circuits*. New York: McGraw-Hill, 1989.

[16] A. Yariv, *Optical Electronics in Modern Communications*, 5th edition. New York: Oxford University Press, 1997.

[17] A. Yariv, and P. Yeh, *Optical Waves in Crystals*. New York: John Wiley & Sons, 1984.

[18] A. Yariv, "Coupled-mode theory for guided-wave optics," *IEEE Journal of Quantum Electronics*, vol. QE-9, no. 9, pp.919-933, 1973.

[19] C. T. Wang, *Applied Elasticity*, Mcgraw-Hill, New York, 1953.

[20] K. Iizuka, *Engineering Optics*, 2nd edition, Springer-Verlag, 1986.

[21] D. A. Pinnow, *Handbook of Lasers*, edited by R. J. Pressley, CRC Press, Cleveland, 1971.

[22] R. C. Alferness, "Efficient waveguide electro-optic TE↔TM mode converter/wavelength filter," *Applied Physics Letters*, vol. 36, no. 7, pp. 513-515, April 1980.

[23] Y. S. Kim and R. T. Smith, "Thermal expansion of lithium tantalate and lithium niobate single crystals," *Journal of Applied Physics*, vol. 40, no. 11, pp. 4637-4641, Oct. 1969.

[24] K. Saitoh, M. Koshiba and Y. Tsuji, "Stress analysis method for elastically anisotropic material based optical waveguides and its application to strain-induced optical waveguides," *Journal of Lightwave Technology*, vol. 17, No.2, pp 255-259 1999.

[25] N. Mabaya, P.E.Lagasse and P. Vandebulcke, "Finite element analysis of optical waveguides," *IEEE Transactions on Microwave Theory and Techniques*, vol. MTT-29, No.6, pp600-605 1981.

[26] O. Eknoyan, H. F. Taylor, J. M. Marx, Z. Tang, and R. R. Neurgaonkar, "Guided-wave electrooptic devices utilizing static strain induced effects in ferroelectrics," *Ferroelectrics*, vol. 205, pp. 147-158, 1998.

[27] D. F. Nelson and R. M. Mikulyak, "Refractive indices of congruently melting lithium niobate," *Journal of Applied Physics*, vol. 45, no. 8, pp. 3688-3689, Aug. 1974.

[28] F. Heismann and R. C. Alferness, "Wavelength-tunable electrooptic polarization conversion in birefringent waveguides," *IEEE Journal of Quantum Electronics*, vol. QE-24, no. 1, pp. 83-93, Jan. 1988

[29] R. C. Alferness and L. L. Buhl, "Long-wavelength Ti:$LiNbO_3$ waveguide electro-optic TE↔TM converter," *Electronics Letters*, vol. 19, no. 1, pp. 40-41, Jan. 1983.

[30] R. C. Alferness, "Waveguide electrooptic modulators," *IEEE Transactions on Microwave Theory and Techniques*, vol. MTT-30, no. 8, pp. 1121-1137, Aug. 1982.

[31] R. J. Holmes and D. M. Smyth, "Titanium diffusion into $LiNbO_3$ as a function of stoichiometry," *Journal of Applied Physics*, vol. 55, no. 10, pp. 3531-3535, May 1984.

[32] J. L. Jackel, V. Ramaswamy, and S. P. Lyman, "Elimination of out-diffused surface guiding in titanium-diffused $LiNbO_3$," *Applied Physics Letters*, vol. 38, pp. 509-511, Apr. 1981.

[33] R. V. Schmidt and I. P. Kaminow, "Metal-diffused optical waveguides in $LiNbO_3$," *Applied Physics Letters*, vol. 25, no. 8, pp. 458-460, Oct. 1974.

[34] T. Tamir, *Guided-Wave Optoelectronics*, pp. 145-211, Springer-Verlag, Berlin, 1988.

[35] Y. Shin, O, Eknoyan, and H. F. Taylor, "Polarization dependence of the coupling ratio in $LiTaO_3$ directional couplers," *Applied Optics*, vol. 44, no. 7, pp. 1156-1159,

Mar. 2005.

[36] G. D. Boyd, W. L. Bond, and H. L. Carter, "Refractive index as a function of temperature in $LiNbO_3$," *Journal of Applied Physics*, vol. 38, no. 4, pp. 1941-1943, Mar. 1967.

[37] I.R. Croston, A.D. Carr, N.J. Parsons and S.N. Radcliffe, L.J. Ville,"Lithium Niobate electro-optic tunable filter with high sidelobe suppression," Electron. Lett., 29, pp.157-159, 1993.

[38] Y. Ping, "Programmable two-port polarization independent electro-optically tunable wavelength filter," Ph.D. Dissertation, Texas A&M University, Department of Electrical and Computer Engineering, College Station, Texas, 2006.

APPENDIX 1

DICING WAFERS

1. Mount a blue tape to an o-ring and place a $LiNbO_3$ wafer on the center of the tape.
2. **R** Turn on 4 knobs/switches for dicing: water valve behind the sink (yellow), air knob under bench (black), vacuum pump power switch under saw (silver), water line valve under saw (yellow).
3. **R** Turn on saw power.
4. Select PROGRAM and program 300 was used. Confirm parameters.
5. Check two parameters of Height = 0.6 mm and Thickness = 1.1 mm for 1 mm thick wafer. Select PROGRAM again to finish setting.
6. **R** Turn on spindle and wait until indicated light was stabilized.
7. Select ZERO CHUCK. Be prepared to RESET if the blade cuts into chuck.
8. Place the wafer mount on the chuck, and select WAFER LOCK.
9. Select ALIGN. Align the wafer with crosshairs using controlling panels on right.
10. Press SINGLE CUT to start cutting.
11. Do a test run before cutting into the wafer.
12. When finished, select WAFER RELEASE.
13. Do steps marked **R** in reverse order to shut down system.
14. Take out diced substrates.

APPENDIX 2

SUBSTRATE CLEANING PROCEDURE

1. Brush and swip a substrate gently with a Q-tip in soapy water.
2. Rinse several times thoroughly with D.I. water.
3. Sonicate in Acetone for 10 minutes.
4. Rinse with Methanol.
5. Sonicate in Methanol for 10 minutes.
6. Rinse with D.I. water.
7. Sonicate in soap water for 10 minutes.
8. Rinse with D.I. water.
9. Sonicate in D.I. for 10 minutes.
10. Rinse with Methanol.
11. Blow dry with N_2.

APPENDIX 3

DC SPUTTERING PROCEDURE

1. Turn on TC main power and main power to valves at the center under target.
2. Vent the chamber and load samples.
3. Close bell jar and turn on mechanical pump switch.
4. Turn on chamber roughing valve and wait until chamber pressure is below 50 μmHg.
5. Close roughing valve and open high vacuum valve all the way.
6. Heat bell jar up to 60°C.
7. Wait until chamber pressure drops below 2×10^{-6} Torr.
8. Turn on cooling system for thickness monitor and set the cooling temperature at 15°C.
9. Turn on Argon gas valve and set the flow rate at 140sccm.
10. Adjust high vacuum valve until Hastings vacuum gauge reads 22 μmHg.
11. Set parameters of thickness monitor.(For Ti, Density:4.5, Z-ratio:0.628, Tooling 325)
12. Turn on power supply and select the red button.
13. Turn on the current dial slowly to 40 mA.
14. Pre-sputtering for 15 minutes.
15. Rotate to the sample position and start deposition.
16. After finish deposition, turn off the current dial, power supply, and Argon gas valve.
17. Reset the cooling temperature to 25°C and turn off the system.
18. Wait for more than two hours and take out samples.

APPENDIX 4

POSITIVE PHOTOLITHOGRAPHY PROCESS

1. Dehydrate samples at 135°C for 5 minutes.
2. Let samples cool down for 10 minutes.
3. Spin Clariant AZ 5214 photoresist at 5000 rpm for 30 seconds.
4. Soft bake samples at 99°C for 2 minutes and 30 seconds.
5. Cool down samples for 10 minutes.
6. Expose samples under UV light with 8 mw/cm^2 power density for 7 seconds without filter.
7. Develop samples in a Shipley MF312:H_2O = 1:1.2 solution for 50 seconds.
8. Rinse samples thoroughly with D.I. water.
9. Blow dry samples gently with N_2.

APPENDIX 5

POSITIVE PHOTOLITHOGRAPHY PROCESS ON SiO_2 FILM

1. Dehydrate samples with SiO_2 film at 135°C for 15 minutes.
2. Wait until samples cools down to room temperature.
3. Spin adhesion promoter(AZ promoter) first at 3000 rpm for 30 seconds for improving the adhesion between SiO_2 film and photoresist.
4. Spin Clariant AZ 5214 photoresist at 3000 rpm for 30 seconds.
5. Soft bake samples at 99°C for 4 minutes.
6. Cool down to room temperature.
7. Expose samples under UV light with 8 mw/cm^2 power density for 7.7 seconds without filter.
8. Develop samples in a Shipley MF312:H_2O = 1:1.2 solution for 70 seconds.
9. Rinse samples thoroughly with D.I. water.
10. Blow dry gently with N_2.

APPENDIX 6

O_2 PLASMA ASHING

1. Turn on power supply and vacuum pump.
2. Vent and load samples into barrel asher.
3. Pump down the chamber and O_2 line below 50 μmHg.
4. Turn on O_2 valves and adjust flow rate until chamber pressure reaches 500 μmHg.
5. Turn on forward power to 100 watts and keep reflected power below 5 watts.
6. Run RF for 3 minutes.
7. When finished, vent and take out samples.
8. Turn off valves, O_2 gas, and power supply.

APPENDIX 7

REACTIVE ION ETCHING (RIE)

1. Turn on main power and warm up for 30 minutes.
2. Vent and load samples into the chamber.
3. Turn on power switches of mechanical pump and high vacuum pump. (Not the valves)
4. Open roughing valve until chamber pressure drops below 7000 μmHg.
5. Close roughing valve.
6. Open high vacuum valve.
7. Until chamber pressure drops to 20 μmHg or below, switch throttle valve to auto.
8. Turn on gases and adjust the flow rate. CHF_3 ~ 30 sccm, Argon ~ 3 sccm, and Helium ~ 7.5 sccm.
9. Wait until chamber pressure stabilized at 70 μmHg.
10. Turn on RF power. Adjust forward power to 350 watts and reflected power to 0 watt.
11. Start etching and timing.
12. After finished etching, turn off RF power, close gases, and switch throttle valve to open.
13. Wait for few minutes and close high vacuum valve and blower switch.
14. Vent and take out samples.
15. Turn off the mechanical pump and high vacuum pump.
16. Turn off main power.

APPENDIX 8

LAYOUT DIMENSION OF A BEAM SPLITTER

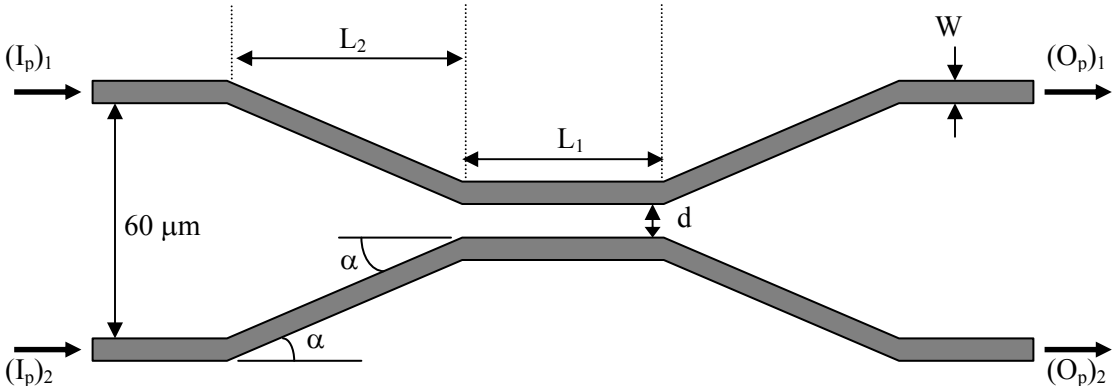

Fig. 52. Four-port directional coupler beam-splitter configuration.

Table 10. The dimension of a polarization beam splitter with $\alpha = 0.6°$ and $L_1 = 3.5$ mm.

Device #	1K	2K	3K	4K	5K	6K	7K	8K	9K
w (μm)	7	7	7	7	7	8	8	7	8
d (μm)	5	7	9	11	13	8	12	-	-
L_2 (μm)	2626	2531	2435	2340	2244	2483	2292	-	-

Note : L_2 is length for inner edge of W/G based on inside separation of 60 μm.

APPENDIX 9

DEKTAK^3 SURFACE PROFILE MEASURING SYSTEM

1. Start the program.
2. Load a sample on the platform and turn on the light.
3. In program: SETUP→STYLUS→ALIGN, adjust the focus and alignment.
4. In program: SCAN PROGRAM→SCAN ROUTINE, set the scanning length and profile mode.
5. Select F4 key to start scanning.
6. Move R and M markers to proper position to level the scanned profile.
7. Move R and M markers again to right position to measure the thickness.
8. In program: ANALYSIS→ANALY FUNCTIONS→AVE HEIGHT→COMPUTE, the thickness is given.
9. After measurement, exit program and turn off the light.

APPENDIX 10

TITANIUM IN-DIFFUSION PROCESS

1. Load well cleaned samples on an alumina (Al_2O_3) D-tube, and put the D-tube in the center of an alumina long tube.
2. Use a glass rod to adjust the alumina tube to the center of a quartz tube of the furnace.
3. Seal the quartz tube with a quartz cap at front and connect to a bubbler.
4. Turn on compressed air valve and adjust air flow rate at the back of the furnace.
5. Adjust settings at front panel for desired diffusion temperature.
6. Wait until air flow rate stabilizes at 3~4 bubbles/second.
7. Turn on control switch.
8. Until current meters stabilize; turn on element switch.
9. It takes 45~60 minutes to heat up to the set temperature.
10. When current meters swing on/off, start counting diffusion time.
11. Frequently check the bubbling rate at front during diffusion.
12. Until reaching the total diffusion time, turn off the element and control switches right away.
13. Wait for 3~4 hours until the furnace temperature drops below 200°C.
14. Detach the bubbler. Then turn off compressed air valve.
15. Take out alumina tube and samples next day.

APPENDIX 11

POLISHING PROCESS

1. Apply one or two small drops of UV epoxy (Norland optical adhesive P/N 8101) on the clean waveguide surface of one sample.
2. Place the second sample with the waveguide surface faced down on top of the first sample.
3. Cure epoxy under UV light for 10 minutes each side.
4. Place samples into a polishing mount and secure the mount to a polish jig.
5. Start rough polishing with polish grit mixed in lapping oil.
6. Polish at 6~7 rpm speed for approximately 15~20 minutes.
7. Clean thoroughly the polishing mount and fixture before next step of fine polishing.
8. Mix 3μm diamond polishing grit with soap, water, and suspendex according to certain ratio.
9. Pour the mixed solution on the polishing plate and tray.
10. Turn on the pump for circulating the mixture.
11. Place the polishing jig on the plate gently, and very slowly increase the rotating speed of the plate to 16 rpm.
12. After polishing for one hour, inspect the end face with microscope. If not satisfied, do 20 minutes polishing interval and check again.
13. Clean all parts for finer polishing with the 0.3 μm diamond polishing grit.
14. Repeat the same procedure as polishing with 3 μm grit mixture.

15. Polish for 15~20 minutes at 16 rpm.

16. Take out samples and soak in MF312 until separate.

17. Clean the sample surface with methanol.

18. Inspect edge quality under microscope before optical testing.

APPENDIX 12

IMAGE REVERSAL PROCESS

1. Dehydrate samples at 135°C for 10 minutes.
2. Wait until samples cool down to room temperature.
3. Spin Clariant AZ 5214 photoresist at 4000 rpm for 30 seconds.
4. Pre soft-baked at 100°C for 1 minute.
5. Cool down for 5 minutes.
6. Fast exposed under 8.0 mw/cm^2 UV light for 1.0 seconds with a filter.
7. Second soft-baked at 110°C for 2 minutes.
8. Cool down for 10 minutes.
9. Flood exposed under 8.0 mw/cm^2 UV light for 2 minutes without a filter.
10. Develop samples in a Shipley MF312:H_2O = 1:1.2 solution for 45 seconds.
11. Rinse samples well with D.I. water.
12. Blow dry samples gently with N_2.

APPENDIX 13

E-BEAM EVAPORATION PROCEDURE

1. Turn on the thickness monitor and the indicated light should flash twice. If light keeps flashing, the thickness crystal sensor needs to be replaced. Then turn it off.
2. Before venting the chamber, make sure the roughing valve and high vacuum valve are closed.
3. Vent the system.
4. Place crucibles with deposited materials and load samples.
5. Close the lid and turn on the mechanical pump and roughing valve to pump down the system.
6. Wait until the chamber pressure drops below 50 μmHg.
7. Close the roughing valve.
8. Turn on the high vacuum valve.
9. Turn off the mechanical pump.
10. Wait until system pressure is below 7×10^{-6} torr.
11. Turn on the cooling system.
12. For SiO_2 deposition, start to heat up samples slowly until 385°C. Open the O_2 valve and adjust O_2 flow rate at 1~2 sccm when the sample temperature reaches 200°C. Keep the chamber pressure below 1.0×10^{-5} torr.
13. Turn on the thickness monitor and set parameters of the density and z-ratio for deposited materials.

14. Start deposition.
15. For Cr/Au/Ti electrode deposition, wait for 15~20 minutes before depositing another metal layer.
16. After the deposition is complete, turn off the thickness monitor.
17. For deposited SiO_2 film, turn off the heating variac and open O_2 control knob all the way until the sample temperature drops below 50°C.
18. Leave the cooling system on for at least one hour.
19. Close the O_2 valve.
20. Turn off the cooling system.
21. Close the high vacuum valve.
22. Vent the system and take out samples.

APPENDIX 14

LAYOUT DIMENSION OF A TUNABLE ADD/DROP FILTER

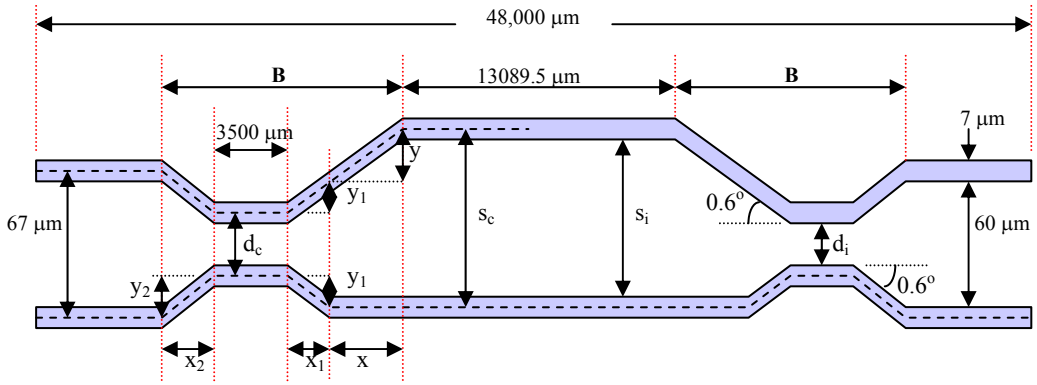

Fig. 53. The waveguide layout diagram of a tunable add/drop filter.

Table 11. The mask layout of devices with different waveguide gap d_c and optical path for tunable add/drop filters.

Device #	MZI-1	MZI-2	MZI-3	MZI-4
x_2 [µm]	2339.49	2244	2339.49	2244
y_2 [µm]	24.5	23.5	24.5	23.5
d_c [µm]	18	20	18	20
x_1 [µm]	2056.03	2056.03	2051.56	2051.56
y_1 [µm]	21.53	21.53	21.48	21.48
x [µm]	3240.62	3240.62	3249.57	3249.57
y [µm]	33.94	33.94	34.03	34.03
s_c [µm]	95	97	95	97
s_i [µm]	88	90	88	90
d_i [µm]	11	13	11	13
B [µm]	11136.14	11040.65	11140.62	11045.13

APPENDIX 15

LAYOUT OF A TUNABLE ADD/DROP FILTER PATTERN

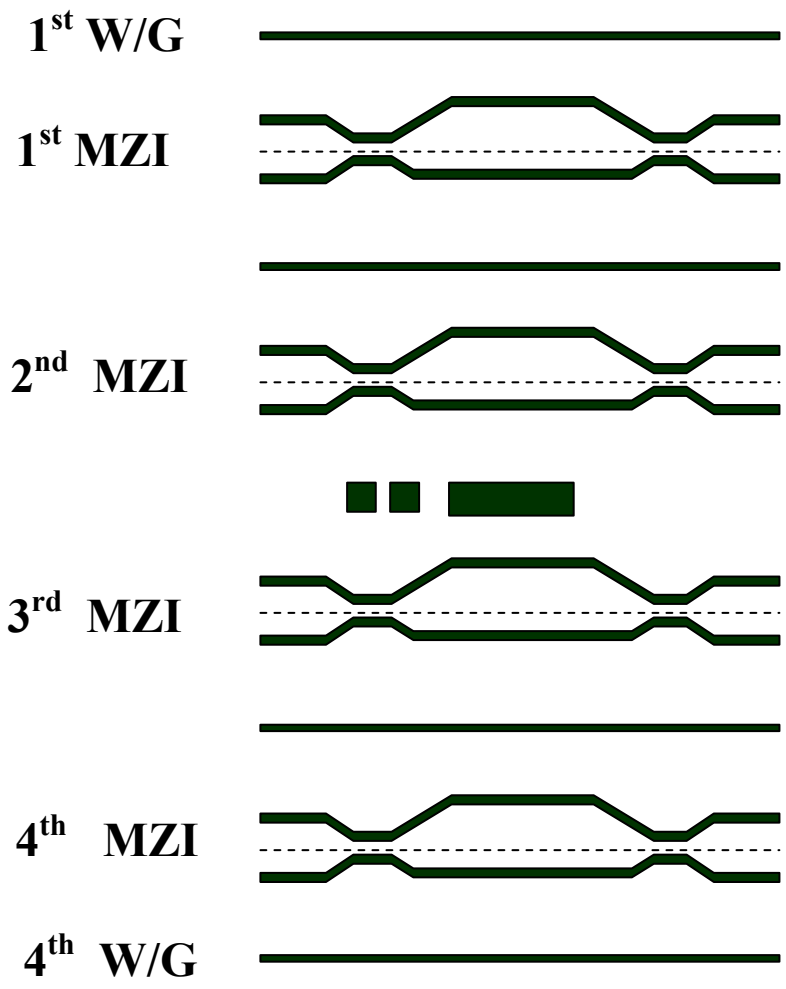

Fig. 54. The waveguide layout diagram of tunable add/drop filters.

APPENDIX 16

LAYOUT DIMENSION OF ELECTRODES

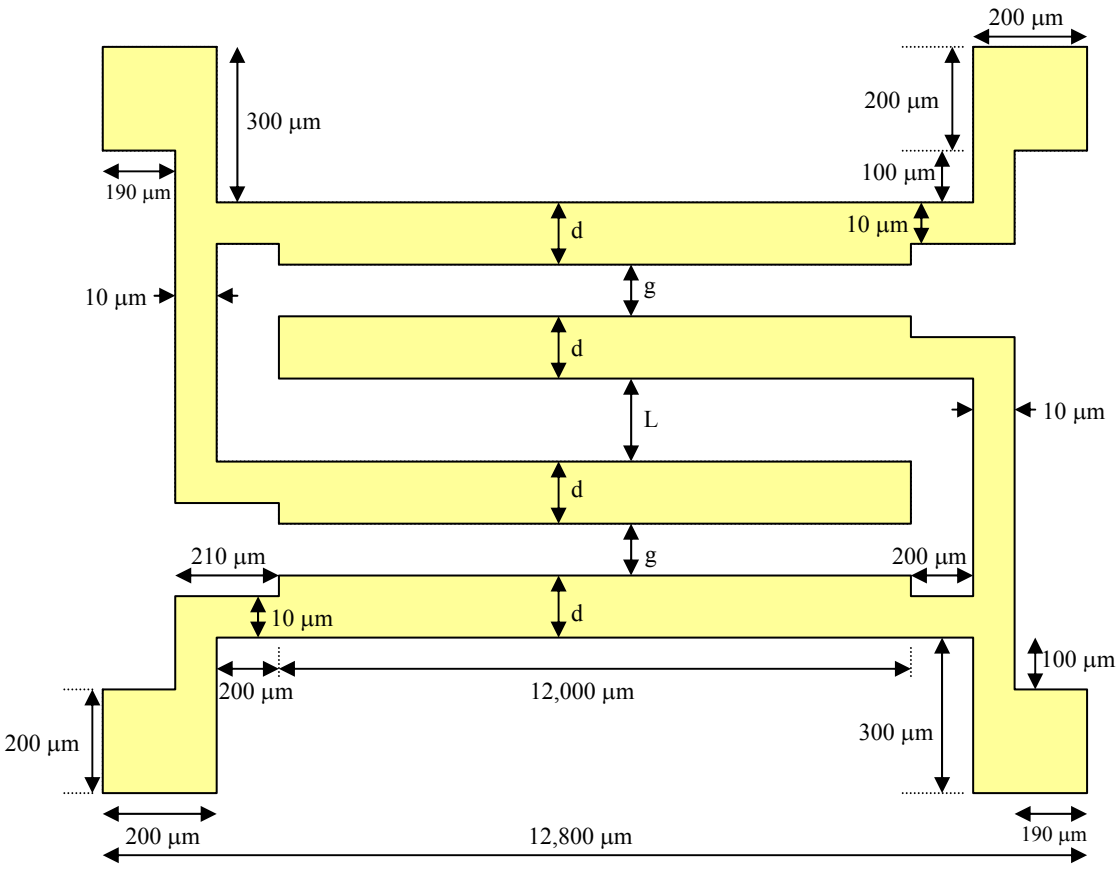

Fig. 55. The layout of the electrode pattern.

Table 12. The layout dimension with different electrode gaps.

Device #	MZI-1	MZI-2	MZI-3	MZI-4
d (µm)	13	13	13	13
L (µm)	52	54	52	54
g (µm)	17	17	17	17

APPENDIX 17

LAYOUT DIMENSION OF STRAIN INDUCING GRATINGS

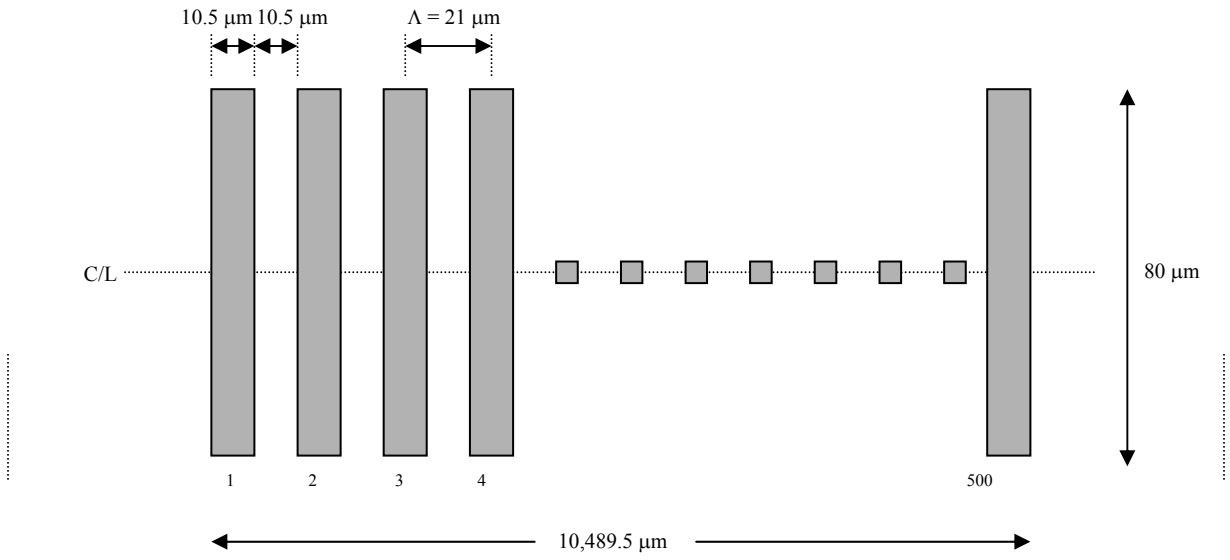

Fig. 56. The layout dimension of strain inducing gratings.

APPENDIX 18

DETAIL TEST CONNECTION FOR MODE PROFILE

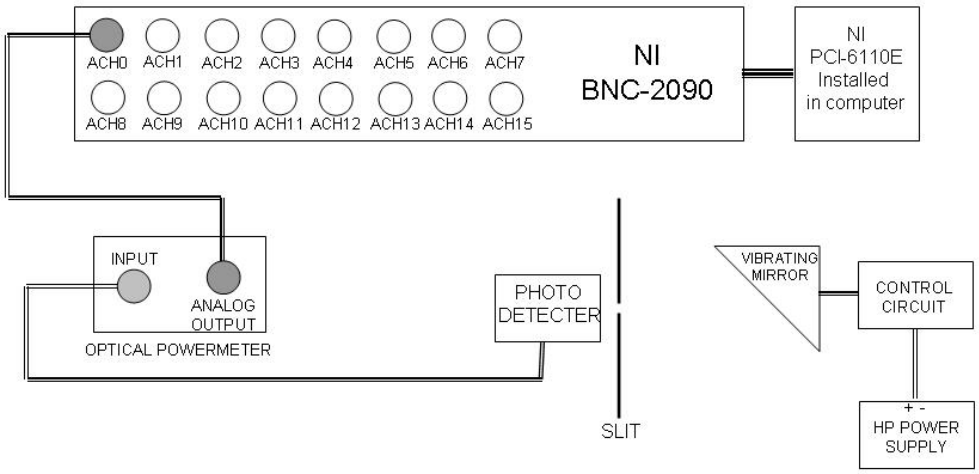

Fig. 57. Testing setup connection for intensity mode profile.

VITA

Yong-Wook Shin was born in Seoul, Korea. He received his B.S. and M.S degree in ceramic engineering from Yonsei University, Korea in 1999 and 2001, respectively. He started his doctoral program in electrical engineering at Texas A&M University in Sept. 2002 and received his Ph.D. degree in August 2008. He can be reached at the following address:

Yong-Wook Shin

20341 NW Colonnade Dr. #2107, Hillsboro, OR 97124